ROSETTE SPECTROSCOPIC IMAGING

by

Claudiu V. Schirda

BS, University of Bucharest, 1997

MS, University of Pittsburgh, 1998

Submitted to the Graduate Faculty of

Arts and Sciences in partial fulfillment

of the requirements for the degree of

Doctor of Philosophy

University of Pittsburgh

2007

UNIVERSITY OF PITTSBURGH

FACULTY OF ARTS AND SCIENCES

This dissertation was presented

by

Claudiu V. Schirda

It was defended on

February 22, 2007

and approved by

Dr. Rainer Johnsen - Committee member

Dr. Hrvoje Petek - Committee member

Dr. Ralph Roskies - Committee member

Dr. Fernando Boada - Committee co-chairperson

Dr. Irving Lowe - Committee co-chairperson

ii

ROSETTE SPECTROSCOPIC IMAGING

Claudiu V. Schirda, PhD

University of Pittsburgh, 2007

Chemical shift imaging (CSI) has been the mainstay of spectroscopic imaging because of its simple implementation, reliability and ease of image reconstruction. This technique has been widely used for observing the changes in the metabolic signature of tissues during evolving pathological and/or physiological conditions. CSI owes its ease of implementation and analysis to the Fourier encoding approach upon which is based. In this approach, the spectral-spatial information is encoded in a rectilinear fashion that favors the acquisition of very high-resolution information along the spectral axis and relatively low resolution along the spatial directions. For applications where higher spatial resolution is desired over a narrower spectral bandwidth, trajectory designs that repeatedly cross the center of k-space through the use of time-dependent gradients offer a convenient means to achieve significant speedups in data acquisition. This stems from the fact that the readout period could be used to acquire multiple spatial frequency values which, in turn, leads to a reduction in the total number of RF excitations required to provide proper encoding of the spatial and spectral information. Among the trajectory designs that could be well suited for such a spectroscopic imaging approach the Rosette data acquisition approach is particularly attractive because of its relatively simple implementation and modest gradient requirements. The time-varying nature of the gradients in this trajectory design, while flexible, leads to smooth variations in sample density and larger signal bandwidths than those associated with the CSI gold standard. Despite these potential drawbacks, because no time is

spent collecting information in the corners of k-space, we demonstrate that rosette spectroscopic imaging (RSI) can lead to an efficiency gain over CSI in a wide range of spectral bandwidths and spatial resolutions. An analytic relationship for the number of excitations to be used in an RSI experiment is derived and a method to obtain a more accurate self-derived B0 map that uses the information of the prevalent resonance in each voxel and linear regression is offered. Moreover, we show that any imaging technique that periodically samples the center and edges of k-space could be used for spectroscopic imaging.

TABLE OF CONTENTS

LIST OF TABLES

ACKNOWLEDGMENTS

I wish to express my gratidude to all the committee members for their continous support and involvement during the completion of this work. Professors Ralph Roskies, Rainer Johnsen, Hrvoje Petek, Irving Lowe and Fernando Boada, thank you! Your questions and observations led me to look at the larger picture of Magnetic Resonance Spectroscopic Imaging and how using the rosette trajectories fit in this picture. It also led to the development of the second spectroscopic imaging technique presented in this thesis. In particular, I wish to thank Dr. Boada for his guidance and pointing out problems that needed to be addressed. It has been a pleasure working with you over these past few years. Above being a scientist, I think you are a great human being.

My thanks go to Dr. Costin Tanase for the numerous hours of discussion and his great attention to detail as well as for the 3D Voronoi volumes he calculated and I used for the comparison made at the end of Section 3.4. Also, thank you for your friendship.

To have your parents, your brother and sisters always believe that you will accomplish whatever you set out to do, to believe in you in general and to trust the decisions you make since you were a little kid, makes life so much easier. This is how my family has always been and I am greatfull for it.

Finally, I dedicate this work to my daughter Claudia Isabella because she made it worthwhile. Her smile always puts a smile on my face, no matter how sunny or rainy the day is.

1.0   INTRODUCTION

1.1   OBJECTIVE

The discovery of the NMR phenomena by Felix Bloch and Edward Purcell in 1946 ushered the scientists into a new era of chemical and physical molecular analysis. However, it was not until 1973 when Paul Lauterbur first demonstrated magnetic resonance imaging (MRI) on small test tube samples using a back projection technique similar to the one used in x-ray computerized tomography (CT). In 1975, Richard Ernst proposed using phase and frequency encoding in conjunction with Fourier Transform and this forms the basis of the current MRI techniques. Since than, remarkable progress has been made and MRI has become the technique of choice for obtaining high quality images of the inside of the human body and for investigating living systems in a non-invasive manner.

Magnetic Resonance Spectroscopic Imaging (MRSI) has developed as an extension of MRI allowing for simultaneous detection of NMR spectra from a large number of voxels and has important applications in studying *in vivo* biochemistry and metabolic pathways in fundamental biomedical research. MRS is also a valuable diagnostic tool and, among other applications, has been successfully used in studies of bipolar disorder, schizophrenia, Alzheimer's disease, cardiac disease, obesity and diabetes. For a long time, the method of choice has been Free Induction Decay Chemical Shift Imaging (FIDCSI), or in short, Chemical Shift Imaging (CSI). However,

because the spectral-spatial information is encoded in a rectilinear fashion that favors the acquisition of very high-resolution information along the spectral axis, the minimum number of phase encodes required is equal to the spatial resolution ($N_x \cdot N_y$), the acquisition times become intolerable long as the resolution increases. A number of fast CSI methods attempting to reduce the experiment duration while preserving an acceptable signal-to-noise (SNR) ratio have been developed. An elaborate study found that while these methods provide a speed-up in data acquisition compared to gold standard CSI, their sensitivity (SNR over square root of total scan time) is generally lower than the one for CSI. Not covered in this study, and of particular interest to us, is a class of CSI methods that uses non-Cartesian trajectories self-rewinding to the center of k-space. We will show that any imaging technique that periodically samples the center and the edges of k-space could be used for spectroscopic imaging, providing not only a significant speed-up in data acquisition but also, potentially, a higher sensitivity compared to conventional CSI.

1.2   THESIS STRUCTURE

This thesis is organized as follows. In Chapter 2.0 basic MRI/MRSI concepts like excitation, use of encoding gradients in K-space (data-space) to generate images/spectroscopic images of spin densities, Bloch evolution equations, sampling requirements to avoid aliasing (Nyquist Criterion) are described.

Chapter 3.0 contains the bulk of this thesis and looks at the Rosette trajectories from a new perspective, namely in K-t space. An innate property of these trajectories is the periodic sampling of the center and edges of K-space and this will be used extensively in setting the

requirements for proper K-t space sampling when designing the gradient waveforms/trajectories (Section 3.3). Based on the nuclei used (^{1}H, ^{31}P, etc.), and hardware constraints (maximum slew rate, gradient and sampling rate) the maximum spectral bandwidth achievable *vs.* spatial resolution is derived. We show that as the spatial resolution N_x increases, the achievable spectral bandwidth decreases and at higher N_x's the data-sampling rate becomes the most limiting factor.

The number of excitations required in the case of non-Cartesian trajectories and especially crossing trajectories is notoriously difficult to quantify. Because we look at the trajectories in the three-dimensional K-t space (two spatial and one temporal dimension), where the trajectories intersect each other only at the center of the space ($K=0$), we succeed in deriving an analytical expression for the number of excitations to be used in an RSI experiment (Section 3.4). The significance of this result is analyzed here. By looking at the two-dimensional (2D) and 3D Voronoi weights, we show that when the number of excitations is approximately equal to the number predicted by the equation we derived, the rosette trajectories achieve their highest sampling efficiency. In addition, the pre-compensation weights required when reconstructing non-uniformly sampled data, can be estimated exactly using an analytical expression.

Because the trajectories are tailor designed for each spatial resolution/spectral bandwidth, in a sense, Section 3.3 goes hand-in-hand with the Data Reconstruction (Section 3.5).

In Section 3.6, we predict that RSI will perform better than a CSI acquisition with square support because it doesn't spend time collecting high-frequency spatial information in the corners of K-space and it's more appropriate to compare RSI to a circularly supported CSI acquisition. While the RSI performance will be affected by its non-uniformly sampling pattern, it

still achieves an up to ~15% gain in SNR compared to the square supported CSI over the same acquisition time. These predictions are verified with extensive simulation studies in Section 3.7.

The technique is experimentally demonstrated on phantoms and in vivo by acquiring both Phosphorous ^{31}P and high-resolution ^{1}H spectroscopic images on a leg of a healthy human volunteer (Section 3.8). By adding a second set of trajectories, time delayed with respect to the first one, or in other words, using two temporal interleaves, the bandwidth of the technique is effectively doubled. This is demonstrated for the proton ^{1}H acquired data. The images are corrected with self-derived B0 maps. The algorithm proposed to derive these maps is described in Section 3.8.3.

Discussions and Conclusions are presented in Section 3.9.

In Chapter 4.0 we proceed to demonstrate experimentally that any imaging technique that periodically samples the center and edges of k-space can be used for spectroscopic imaging. We adapt the Twisted Radial Lines (TWIRL) trajectories by forcing the radial component of the gradient to become null at the edge of k-space and then rewinding the trajectory to the center of k-space. Experimental Results are presented to support our theory.

Chapter 5.0 contains concluding remarks.

In Appendix, the theoretical sampling uniformity/efficiency factor for a rosette trajectory acquisition is calculated.

2.0 MRI/MRSI BASICS

2.1 BASIC MRI PRINCIPLES

When imaging an object, the wavelength of the energy used to image needs to be smaller than the size of the object. This is the case with X-ray imaging, optical and electronic microscopes and the list of applications could go on. However, when this is not possible, researchers found ways around this limitation. The trade-off is giving up on the 'instantaneous' nature of imaging associated with wavelengths smaller than the structure of the object imaged. For example, in Experimental High Energy Physics, when probing for the structure of protons and neutrons, looking for quarks and other elementary particles, the scale of energy involved is rather difficult if not impossible to achieve even in the large accelerators used in this kind of experiments. Matter and antimatter is collided at relativistic speed and scientists look for and analyze the byproducts of these collisions in their search for evidence of a new particle, rather than the particle itself. The experiments need to run sometimes for a few years for enough data/statistics to be generated.

In MRI, the density of nuclear spins placed in a strong magnetic field B_0 is imaged at resolutions of the order of millimeters using as source of energy radio frequencies with wavelengths a few orders of magnitude larger. Gradients are used to generate spatial variations

in B_0 and therefore in the phase and frequency of the radio energy being absorbed and emitted by an object. Images are produced based on these variations.

Consider a pool of protons, placed in a constant magnetic field $\vec{B}_0 = B_0 \cdot \vec{1}_z$.

The spins will precess at the Larmor frequency (γ-gyromagnetic ratio):

$$\omega_0 = \gamma \cdot B_0 \tag{2.1}$$

This is also the resonant frequency of the radiation the spins absorb or emit generating transitions between Zeeman energy levels and corresponding to states aligned or anti-aligned with the magnetic field ($\hbar$-reduced Planck constant):

$$E_0 = \hbar \cdot \omega_0 \tag{2.2}$$

Because a spin of a positive charged particle aligned with B_0 is in a lower energy state than one anti-aligned, on average, at equilibrium, there will be more spins pointing in the direction of the main magnetic field than against it, resulting in a net magnetization $\vec{M}_0 = M_0 \cdot \vec{1}_z$.

If a gradient G_z is applied along the z direction, the magnetic field becomes

$$B(z) = B_0 + G_z \cdot z \tag{2.3}$$

$$\omega(z) = \gamma \cdot B(z) = \omega_0 + \gamma \cdot G_z \cdot z \tag{2.4}$$

The spins at $z > 0$ will precess at a faster resonant frequency $\omega > \omega_0$ and the ones at $z < 0$ will precess at a lower frequency $\omega < \omega_0$. A radio frequency (RF) pulse with a narrow frequency band BW that modulates a carrier wave at ω_0 will excite only the spins below and above $z = 0$ whose resonant frequency are within that RF pulse band. The thin slab of material whose spins have been excited, or tipped, is perpendicular to the direction of the gradient field and has a thickness

$$\Delta z = \frac{\Delta \omega(z)}{\gamma \cdot G_z} = \frac{2 \cdot \pi \cdot BW}{\gamma \cdot G_z} = \frac{BW}{\not{\gamma} \cdot G_z} \tag{2.5}$$

$$\not{\gamma} = \gamma / (2 \cdot \pi) \tag{2.6}$$

If we want to excite the spins in a slice that is centered at a position other than $z = 0$, the frequency of the carrier RF wave can be slightly increased ($z > 0$) or decreased ($z < 0$). This way one spatial dimension is resolved. Applying now a gradient G_x in the x direction (a field whose z component varies linearly in proportion to x) modifies the magnetic field again and therefore the resonant frequency of the spins as a function of their position (G_z is turned off):

$$B(x) = B_0 + G_x \cdot x \tag{2.7}$$

$$\omega(x) = \gamma \cdot B(x) = \omega_0 + \gamma \cdot G_x \cdot x \tag{2.8}$$

All spins at the same position x will precess at the same frequency. An RF receive coil that is spatially non-selective, acquires the signal produced by all the excited spins while the G_x gradient is turned on. Computing the spectrum of this signal produces the amount of magnetization corresponding to each frequency bin and therefore to each position x (Equation(2.8)). The magnetization at position x is the integral of the signal for all the spins in the y dimension (that have the same x), and the spectrum obtained is a projection of the object looking in the y direction. Changing the direction of the gradient (Figure 2-1 left) and collecting additional projections followed by projection-reconstruction to reconstruct the slice, as in X-ray computed tomography, resolves the other two spatial dimensions. This is how MRI was first proposed by Paul Lauterbur in 1973. Two years later, Richard Ernst proposed resolving the two spatial dimensions in the excited slice in a different way.

After resolving the position along z axis as described above, but before using G_x and acquiring the signal with different frequencies along the x dimension, consider turning on a gradient G_y in the y direction for a time interval T_{PE}. This will modify the magnetic field and therefore the precession frequency:

7

$$B(y) = B_0 + G_y \cdot y \tag{2.9}$$

$$\omega(y) = \gamma \cdot B(y) = \omega_0 + \gamma \cdot G_y \cdot y \tag{2.10}$$

No signal is acquired while G_y is turned on. If the strength of the gradient G_y is modified from repetition to repetition, because $\omega(y)$ is different for each repetition, the amount of phase accrued by the spins at position y, before data acquisition starts, is different for each repetition:

$$\varphi(y) = -\omega(y) \cdot T_{PE} = -\gamma \cdot G_y \cdot y \cdot T_{PE} \tag{2.11}$$

This information, combined with the frequency encoded during the time G_x is turned on and data is collected, is resolved with a two dimensional (2D) Fourier Transform. In this case, G_y is called phase-encoding gradient and G_x is called frequency-encoding gradient. The minus sign in Equation(2.11) is introduced due to the convention for a negative precession direction for protons.

In general, an acquisition scheme could employ a gradient waveform

$$\vec{G}(t) = G_x(t) \cdot \vec{1}_x + G_y(t) \cdot \vec{1}_y + G_z(t) \cdot \vec{1}_z \tag{2.12}$$

The resonant frequency and the phase of a spin at position $\vec{r} = x \cdot \vec{1}_x + y \cdot \vec{1}_y + z \cdot \vec{1}_z$ and time t are:

$$\omega(\vec{r},t) = \omega_0 + \gamma \cdot \vec{G}(t) \cdot \vec{r} \tag{2.13}$$

$$\varphi(\vec{r},t) = -\int_0^t \omega(\vec{r},u) \cdot du = -\int_0^t (\gamma \cdot \vec{G}(u) \cdot \vec{r}) \cdot du = -2\pi \int_0^t (\not{\gamma} \cdot \vec{G}(u) \cdot du) \cdot \vec{r} = -2\pi \cdot \vec{k}(t) \cdot \vec{r} \tag{2.14}$$

$$\vec{k}(t) = \int_0^t \not{\gamma} \cdot \vec{G}(u) \cdot du \tag{2.15}$$

The ω_0 contribution to phase in Equation(2.14) is a constant term that is the same for all spins and it has been discarded.

The transversal magnetization at position $\vec{r}$ and time t that we would like to determine, can be written as ($i = \sqrt{-1}$):

$$M_{xy}(\vec{r},t) = M_{xy}(\vec{r}) \cdot e^{-i \cdot 2\pi \cdot \vec{k}(t) \cdot \vec{r}} \qquad (2.16)$$

The RF receive coil, acquires the signal from all the spins in the system, thus:

$$S(t) = \iiint_V M_{xy}(\vec{r}) \cdot e^{-i \cdot 2\pi \cdot \vec{k}(t) \cdot \vec{r}} \cdot d\vec{r} \qquad (2.17)$$

This is the Fourier transform of the spatial distribution of $M_{xy}(\vec{r})$, and by acquiring data (sampling) at different values of the spatial frequency $\vec{k}(t)$, followed by an inverse Fourier transform, the image can be reconstructed. $\vec{k}(t)$ is referred to as K-space trajectory where K-space is the space associated with data acquired $S(t)$ (or $S(\vec{k}(t))$) and image space is associated with $M_{xy}(\vec{r})$.

Two acquisition methods have been presented above. Equation (2.17) suggests there is a lot of flexibility in the way data can be collected and, indeed, numerous sampling strategies have been designed to provide benefits in the applications for which they are intended. However, no matter what kind of K-space trajectories they employ, the Nyquist-Shannon sampling theorem is paramount in designing each strategy. The theorem states that exact reconstruction of a continuous-time baseband signal from its samples is possible if the signal is band limited and the sampling frequency is greater than twice the signal bandwidth. Let $x(t)$ represent a continuous time signal and $X(f)$ be the continuous Fourier transform of that signal:

$$X(f) \triangleq \int_{-\infty}^{\infty} x(t) \cdot e^{-i \cdot 2\pi \cdot f \cdot t} \cdot dt \qquad (2.18)$$

If the signal is band limited to a one-sided baseband bandwidth B, thus $X(f) = 0$ for all $|f| > B$, the condition to be able to reconstruct exactly $x(t)$ from samples at a uniform sampling rate f_s is:

$$f_s > 2 \cdot B \tag{2.19}$$

In practice, the MRI signal is sampled in a discrete fashion and a finite number of complex data points are recorded. When the sampling times are $t_0, t_1, ..., t_{N-1}$ thus, N samples are collected, rather than using the continuous FT in equation(2.18), a Discrete Fourier Transform (DFT) would be calculated:

$$X_n = \sum_{m=0}^{N-1} x_m \cdot e^{\frac{-2\pi \cdot i \cdot m \cdot n}{N}} \tag{2.20}$$

$x_m = x(t_m)$ is the m'th sample collected (out of N samples, $m = 0, 1, ..., N-1$) and $X_n = X(f_n)$ is the n'th DFT sample reconstructed, for a total of N reconstructions ($n = 0, 1, ..., N-1$) corresponding to frequencies $f_0, f_1, ..., f_{N-1}$.

The Shannon-Nyquist sampling theorem applies when using a frequency-encoding gradient. The sampling rate is the inverse of the dwell time Δt_x (time interval between data points acquired) and for an object that fills the entire field of view fov, based on equation(2.8), the signal from all the excited spins in the object has a total bandwidth $\Delta f = 2 \cdot B$:

$$\Delta f = \frac{\omega(fov/2) - \omega(-fov/2)}{2 \cdot \pi} = \gamma \cdot G_x \cdot fov \tag{2.21}$$

Therefore, it is necessary:

$$\gamma \cdot G_x \cdot fov \leq 1/\Delta t_x \tag{2.22}$$

Because $\Delta k_x = \gamma \cdot G_x \cdot \Delta t_x$ (Equation(2.15)), equation (2.22) is equivalent to:

$$\Delta k_x \leq 1/fov \tag{2.23}$$

The distance between the sampling points in K-space Δk, has to be smaller or equal to the inverse of the *fov*. When the condition in equation(2.23), also known as Nyquist Criterion, is satisfied, K-space is properly/sufficiently sampled. If (2.23) is not satisfied, aliasing artifacts will occur. Equation (2.23) is observed in almost every acquisition method; however, there are sampling strategies [62] that sufficiently sample the low frequency components of K-space that contain the most energy, but undersample outer K-space region that contains little energy and therefore will not contribute sever aliasing artifacts. These methods could reduce the total scan time while increasing the spatial resolution.

While techniques that sample asymmetrically K-space exist (only a little more than half K-space is sampled and the symmetry of the Fourier transform is used since an image is a real function, however a phase correction is required), most acquisitions sample the K-space symmetrically because of the numerous sources of phase errors causing the real-value image assumption to be violated. For the technique using phase/frequency encoding introduced by Richard Ernst, technique largely known and used under the colorful name "spin warp", a $K_x - K_y$ space description would go as follows. N_x sample points are collected after each phase encode at intervals $\Delta k_x = 1/ fov_x$ placed between $-K_x^{max}$ and K_x^{max} ($2 \cdot K_x^{max} = N_x \cdot \Delta k_x$)

$$dx = \frac{fov_x}{N_x} = \frac{1}{2 \cdot K_x^{max}}$$ (2.24)

For uniform weighting of the K-space in the y dimension with N_y phase encodes (see Figure 2-1 right), G_y is incremented in equal steps ΔG_y to generate equal increments in K_y:

$$\Delta k_y = 1/ fov_y = \gamma \cdot \Delta G_y \cdot T_{PE}$$ (2.25)

$$\Delta G_y = 1/(\gamma \cdot fov_y \cdot T_{PE})$$ (2.26)

$$G_y^{max} = \frac{N_y \cdot \Delta G_y}{2}$$ (2.27)

The frequencies sampled in the y dimension in Δk_y steps, are in the range $-K_y^{max}$ to K_y^{max} :

$$K_y^{max} = \gamma \cdot G_y^{max} \cdot T_{PE} = \frac{N_y}{2 \cdot fov_y} \tag{2.28}$$

$$dy = \frac{fov_y}{N_y} = \frac{1}{2 \cdot K_y^{max}} \tag{2.29}$$

A 2D FT reconstructs an image with $N_x \cdot N_y$ points in image domain (called pixels) corresponding to a resolution $dx \cdot dy$, over a field of view $fov_x \cdot fov_y$.

So far, in the experiments presented above, the evolution of the magnetization $\vec{M}_0$ has been described from a somewhat simplistic perspective, as the angular momentum would be conserved when there is no external impulse acting on it (e.g. an RF pulse). However, this is not the case. The excited spins interact with other excited spins, resulting in dephasing and a decrease of the transversal magnetization over time and they interact with the lattice spins, resulting in a transition from an excited state to an equilibrium state and therefore in a gradual recovery of the initial longitudinal magnetization. The characteristic times that describe these interactions in a semiclassical fashion are the T_1 spin-lattice relaxation time and T_2 spin-spin relaxation time. In the absence of an external RF field, the time evolution of the longitudinal and transversal magnetizations M_z and M_{xy} can be written as:

$$M_z(t) = M_z(0) \cdot (1 - e^{-t/T_1}) \tag{2.30}$$

$$M_{xy}(t) = M_{xy}(0) \cdot e^{-t/T_2} \tag{2.31}$$

Since the excited spins are aligned and have the same resonant energy, the spin-spin interaction is stronger than the spin-lattice interaction and the transversal relaxation takes place

faster than the longitudinal one. Inhomogeneities in the magnetic field gradient add to the dephasing of the spins, resulting in faster signal loss and spin-spin relaxation described by a T_2^*:

$$\frac{1}{T_2^*} = \frac{1}{T_2} + \frac{1}{T_{inhom}} \tag{2.32}$$

$$T_2^* < T_2 < T_1 \tag{2.33}$$

Due to relaxation phenomenon in imaged objects, the RF pulses used for excitation usually have a duration much shorter than T_1 and T_2. This is known as pulsed NMR and the magnetization $\vec{M}$ evolution equation, if T_1 and T_2 effects are neglected, is:

$$\frac{d\vec{M}(t)}{dt} = \vec{M}(t) \times \gamma \vec{B}(t) \tag{2.34}$$

In general, the time evolution of the magnetization in the presence of an RF field is described by the Bloch Equations, which update equation(2.34) to include the relaxation effects:

$$\frac{dM_z(t)}{dt} = \gamma \cdot (M_x(t) \cdot B_y(t) - M_y(t) \cdot B_x(t)) - \frac{M_z(t) - M_0}{T_1} \tag{2.35}$$

$$\frac{dM_x(t)}{dt} = \gamma \cdot (M_y(t) \cdot B_z(t) - M_z(t) \cdot B_y(t)) - \frac{M_x(t)}{T_2^*} \tag{2.36}$$

$$\frac{dM_y(t)}{dt} = \gamma \cdot (M_z(t) \cdot B_x(t) - M_x(t) \cdot B_z(t)) - \frac{M_y(t)}{T_2^*} \tag{2.37}$$

In above equations, $\vec{B}$ is the total magnetic field. Therefore, in the most general case:

$$\vec{B}(\vec{r},t) = (B_0 + \vec{G} \cdot \vec{r}) \cdot \vec{1}_z + \vec{B}_1(\vec{r},t) \tag{2.38}$$

In MRI, the RF field $\vec{B}_1$ generated by an RF transmit coil (that plays the role of an acquisition coil after generating the $\vec{B}_1$ field), has time varying x and y components, with $B_{1z} = 0$. For a spatially homogeneous $\vec{B}_1$, if the gradients are turned off ($\vec{G} = 0$), the effective magnetic experienced by the spins is:

$$B_{eff} = \sqrt{B_0^2 + B_1^2} \qquad (2.39)$$

With Ω in a narrow range $-BW/2$ to $BW/2$, $\vec{B}_1$ can be written:

$$\vec{B}_1(\vec{r},t) = B_1 \cdot (\cos((\omega_0 + \Omega) \cdot t) \cdot \vec{1}_x + \sin((\omega_0 + \Omega) \cdot t) \cdot \vec{1}_y) \qquad (2.40)$$

RF pulses ($\vec{B}_1(\vec{r},t)$), that produce desirable magnetization profiles $M_{xy}(\vec{r})$, can be designed based on solving Bloch's Equations, analytically or numerically [9-11, 13, 26, 33, 43-47, 52, 60].

Figure 2-1 Projection Imaging (PI) and Spin Warp Acquisitions
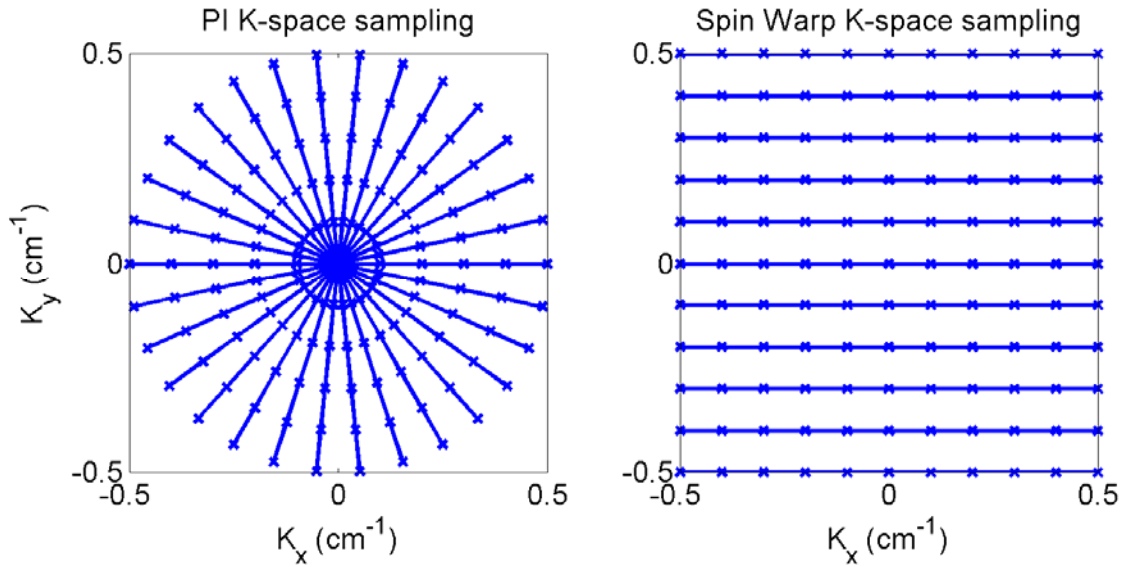
In Figure 2-2, an example of a pulse sequence (rosette acquisition) is shown. The RF pulse is played at the same time with a slice selection gradient G_z, followed by a refocusing z-axis gradient (area is equal to half of the slice selection gradient area). Data is acquired with $G_{x,y}$ on.

Figure 2-2 Rosette Acquisition Pulse Sequence
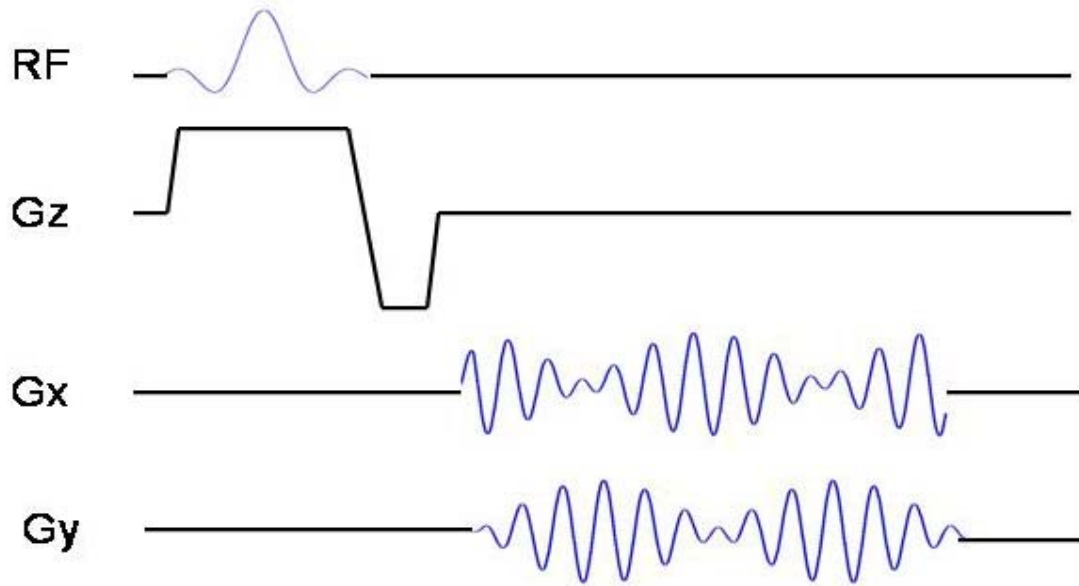
2.2 MAGNETIC RESONANCE SPECTROSCOPIC IMAGING (MRSI) BASICS

A spin in a magnetic field, interacting with the surrounding atoms, will experience a slight shift in its resonant frequency. A proton in a hydrogen atom, or a Phosphorous nucleus or other nuclei for that matter forming a bond with a groups of atoms in a molecule will resonate at a frequency, while the proton or Phosphorous nucleus in the same magnetic field but surrounded by a different group of atoms, will resonate at a different frequency. This shift in frequency, called chemical shift, is usually expressed as a fraction of the resonant frequency ω_0, because, like ω_0, it scales with the main magnetic field B_0, and is usually a few parts per million (ppm).

In Magnetic Resonance Spectroscopic Imaging (MRSI or MRS), unlike MRI where all the chemical shifts are combined in one image, most of the time resulting in artifacts due to incorrect assignment of the frequency which is related to the spatial position (previous section),

these chemical shifts are resolved while at the same time spatial images are generated for each shift.

In a simple spectroscopic experiment, where two different resonances are excited and allowed to decay freely, the measured signal will look like the one in Figure 2-3.

Figure 2-3 Two resonances Free Induction Decay
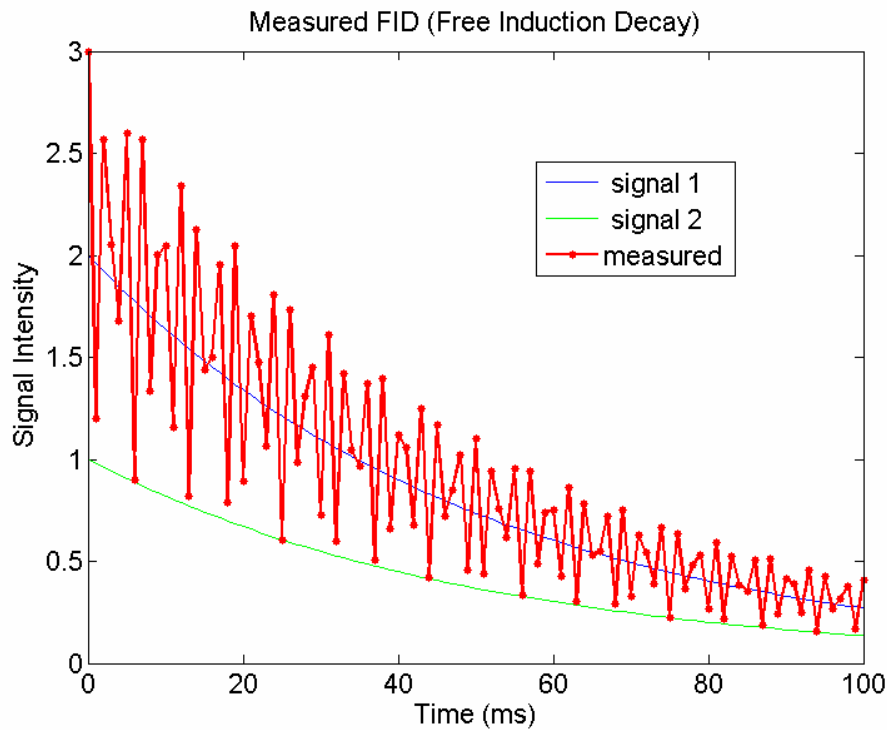
In this form, it would be hard to say much about the spectral components forming the signal. However, applying a Fourier Transform, resolves the two resonances (Figure 2-4). As in imaging (previous section), using the Shannon-Nyquist criterion, for a uniformly time sampled signal at intervals Δt_δ, the spectral bandwidth is $\Delta \delta = 1/\Delta t_\delta$ and the spectral resolution is the inverse of the readout time $df = 1/T_{AQ}$.

Figure 2-4 Two resonances reconstructed spectrum
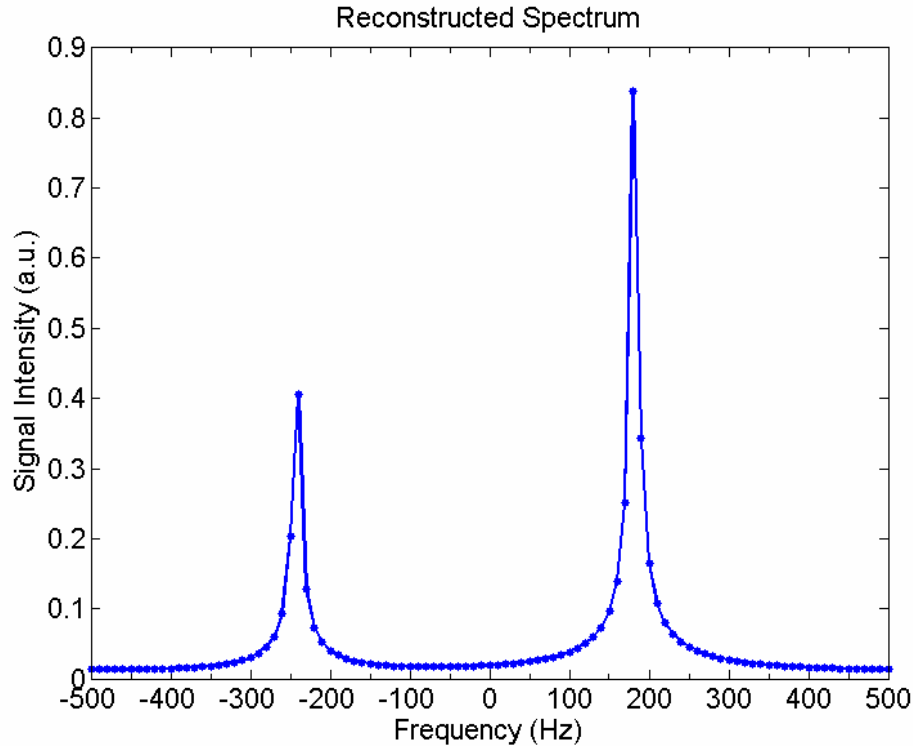
A straightforward way to design a spectroscopic imaging acquisition is to collect FIDs at different positions in K-space. If the sampled positions in K-space are enough to generate a spatial image, the spectral and spatial information is resolved. This is exactly what the Free Induction Decay Chemical Shift Imaging (FIDCSI) technique does. Following a slice selection RF excitation pulse, the G_x, G_y gradients are turned on for a short period τ_G, with different amplitudes from repetition to repetition, encoding different positions in K_x, K_y (Figure 2-7). While all the data points sampled lye on a three dimensional (3D) Cartesian grid (Figure 2-5), allowing for Fast Fourier Transform (FFT) data reconstruction in each direction, the drawback to encoding only one spatial frequency per repetition is a long scan duration as the spatial resolution increases ($T_{CSI} = N_x \cdot N_y \cdot T_R$, T_R is the repetition time).

Figure 2-5 FIDCSI K-t space sampling

FIDCSI
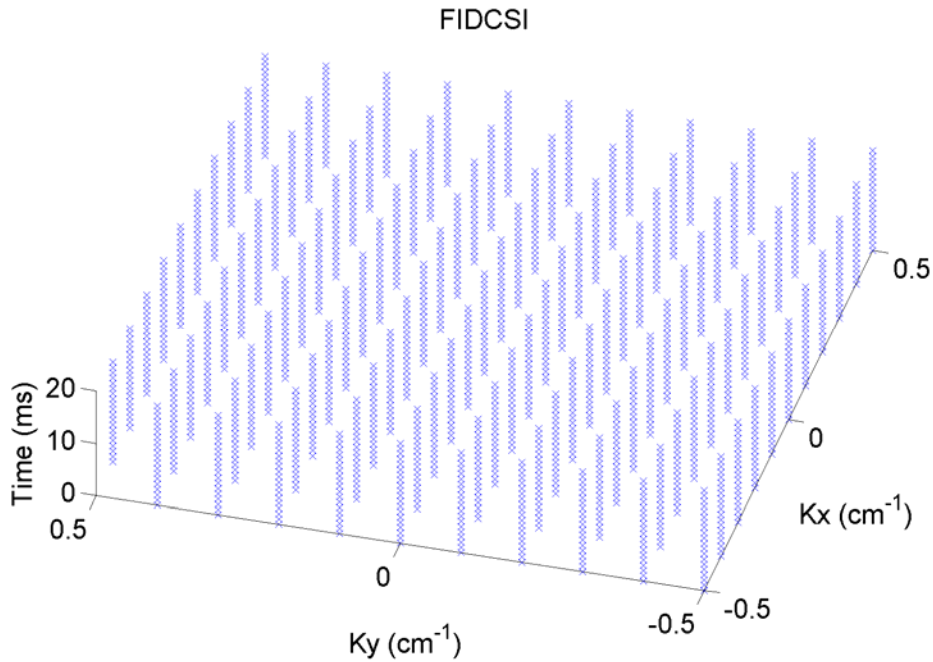
All the fast spectroscopic imaging techniques developed, achieve a speedup in data acquisition by encoding at least two dimensions, usually one spatial and one spectral, over one repletion period. Overall speedup in data acquisition can be also achieved by encoding only one spatial dimension rather than the spectral one as done by CSI, if the spatial resolution N_x is much greater than the spectral one N_δ. Some of these methods will be discussed in section 3.6.1. By looking at K-t space sampling from a different angle (Figure 2-6), it becomes apparent that it can be thought of as a collection of planes (Figure 2-7) with data points collected at the same time interval after each RF excitation. These planes are equally space apart in time at time intervals $dT = 1/\Delta\delta$ (we will also refer to this time as spectral dwell time Δt_δ). We will refer to these planes as temporal planes. In the FIDCSI acquisition, it takes $N_x \cdot N_y$ repetitions to sample properly one of these planes to create an image corresponding to that time moment (echo time).

Figure 2-6 Alternative perspective FIDCSI K-t space sampling
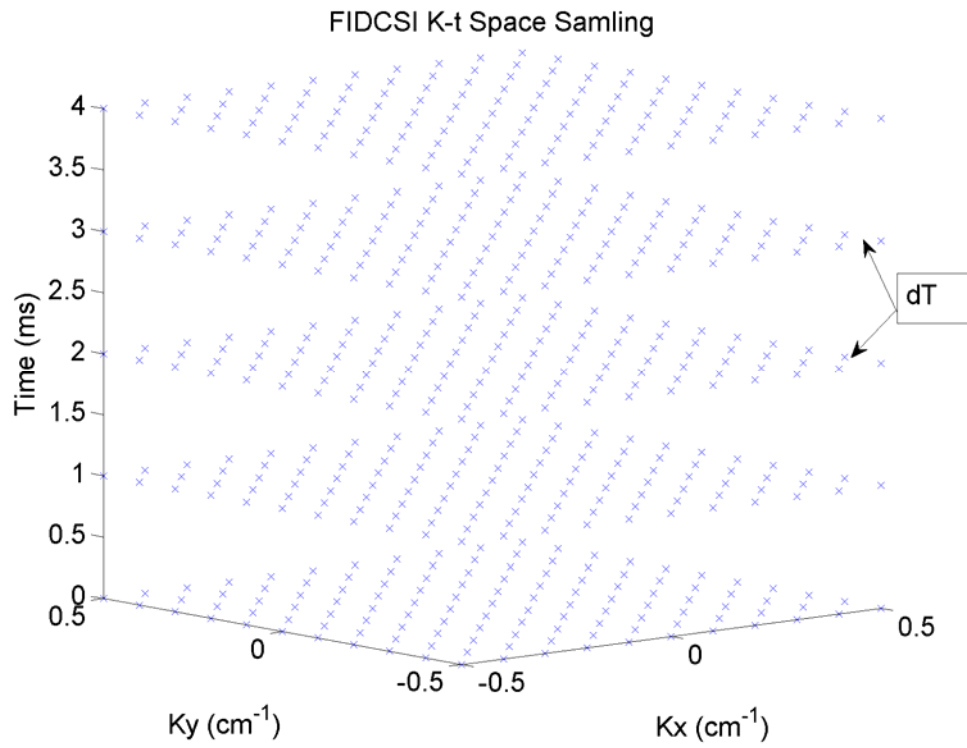
Figure 2-7 Temporal slice FIDCSI K-space sampling
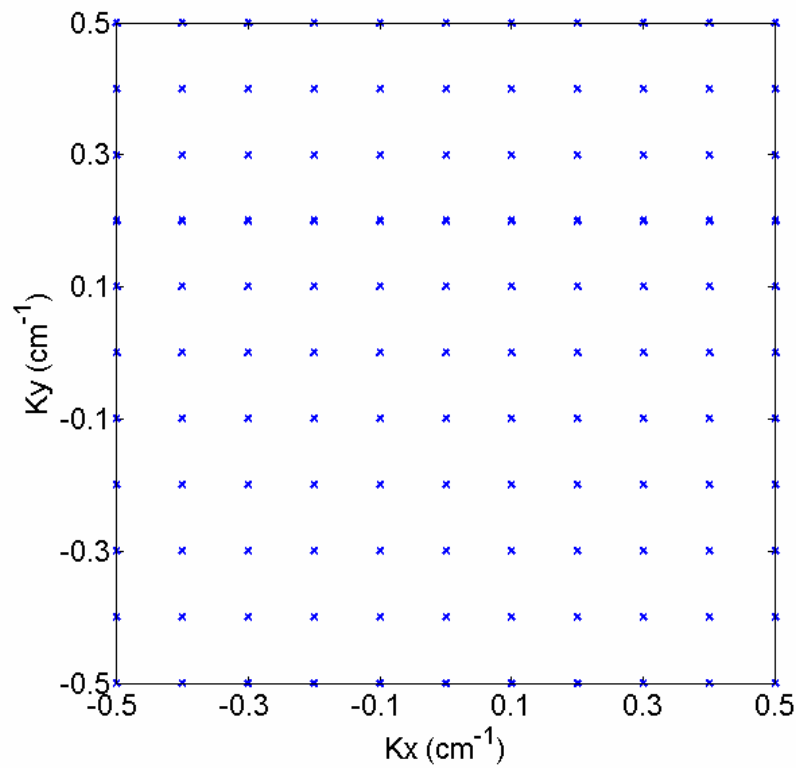
If the duration $dT = 1/\Delta\delta$ is large enough, greater than the time dt necessary for the scanner to collect a data sample, an acquisition trajectory could sample more than one position on this plane, requiring fewer overall excitations to sample properly the K-t space. Moving from one K-space position to another position in this temporal plane, means a gradient would be used (equation(2.15)). In this case, to allow the signal from all spins over the entire field of view in the receiver, we also have to account for the chemical shift at each position, in the range $\Delta\delta$; the signal bandwidth/sampling rate equation (2.22) becomes:

$$\gamma \cdot G \cdot fov + \Delta\delta \leq 1/dt \qquad (2.41)$$

If dT becomes too small (corresponding to a large bandwidth $\Delta\delta$), because a trajectory will be limited by scanner hardware constraints to how fast it can move through K-space (G_{max}^{HW}) or how fast it can turn (slew rate S_{max}^{HW}), or by the maximum signal bandwidth/sampling rate (G_{max}^{samp}-equation(2.41)), it may not be able to sample more than one point during this time. In section 3.3, we will calculate based on these hardware constraints the maximum spectral bandwidth $\Delta\delta_{max}$ that can be achieved by the rosette trajectories.

Note that, depending on the context, when we will refer to spectral resolution, this can be either the separation (in Hz) between the spectral points or spectral slices in the reconstructed spectrum, $df = \Delta\delta / N_\delta$, or it can be the number of spectral points (spectral slices) N_δ. The same goes for the spatial resolution. Depending on the context, it can be either $\Delta x = fov / N_x$ (in cm or mm), or it can be the number of spatial points (in one direction) in the reconstructed image N_x.

3.0   ROSETTE SPECTROSCOPIC IMAGING (RSI)

3.1   INTRODUCTION

A multitude of spectroscopic imaging techniques (mostly using Cartesian trajectories) have been developed for improving Chemical Shift Imaging (CSI) data acquisition times. However, the SNR efficiency in these approaches was shown by Pohmann *et al.* [50] to be lower than that for standard CSI. This stems from an inefficient/partial use of the available data collection time following each excitation, as we will show in Section 3.5.1. Not covered in [50], and of particular interest to us, is a class of CSI methods that uses trajectories self-rewinding to the center of K-space. We'll demonstrate that self-rewinding trajectories, for example Out-and-In Spirals and Rosette trajectories, or any imaging technique that can be adapted to periodically sample the center and edges of K-space and don't spend time acquiring the low-energy data in the corners of K-space, can make optimal use of the signal available after each radio frequency (RF) excitation. Our results demonstrate that, in addition to speedups of one or two orders of magnitude in data acquisition, self-rewinding trajectories have the potential to achieve higher sensitivity (signal-to-noise (SNR) over square root of total scan time) than CSI, thus allowing for greater flexibility in selecting the total scan time.

The rosette trajectories have been chosen because of the relative ease to generate and implement the gradient waveforms and because the gradients vary smoothly in time. First

proposed by Likes [25], rosette trajectories have been examined and demonstrated experimentally for spectrally selective MR imaging by Noll [37] and Noll *et al.* [39]. In these approaches, data is first being demodulated at the resonant frequency of each spectral component present and then reconstructed in a two-dimensional (2D) imaging fashion. We will be looking and reconstructing the data from a three dimensional (3D) perspective (two spatial dimensions plus one spectral dimension), simultaneously resolving the spatial and spectral information. This will allow us to set general conditions for choosing the trajectory parameters and obtain the highest SNR efficiency. In addition, the 3D perspective will reveal that a whole class of trajectories, namely self-rewinding trajectories or trajectories that can be adapted to sample periodically the center and edges of K-space, share common spectroscopic properties and could be used for spectroscopic imaging. Adapting for spectroscopic imaging an imaging technique that uniformly samples K-space, further improves on the SNR efficiency achieved by RSI (in Chapter 4.0 of this thesis).

3.1.1   Rosette Trajectory Properties

The rosette trajectories consist of a radial oscillation about the origin of K-space with angular oscillation frequency $\omega_1 = 2\pi \cdot f_1$ that rotates in $K_x - K_y$ space with angular oscillation frequency $\omega_2 = 2\pi \cdot f_2$. They are mathematically described by:

$$\vec{K}(t) = K_{\max} \cdot \sin(\omega_1 t) \cdot e^{i \cdot \omega_2 \cdot t} \tag{3.1}$$

To encode K-space properly, usually more than one excitation is required and a multishot acquisition is employed. In general, this is done by using a number N_{sh} of excitations that are

subsequently rotated with respect to the first trajectory by an angle $\varphi_0 = 2\pi \cdot n / N_{sh}$ with $n = 1, 2, ..., N_{sh} - 1$.

Figure 3-1 shows these trajectories ($\omega_1 > \omega_2$) in K-space and in Figure 3-2 they are depicted in K-t space:

Figure 3-1 K-space sampling of a temporal slice using one trajectory set
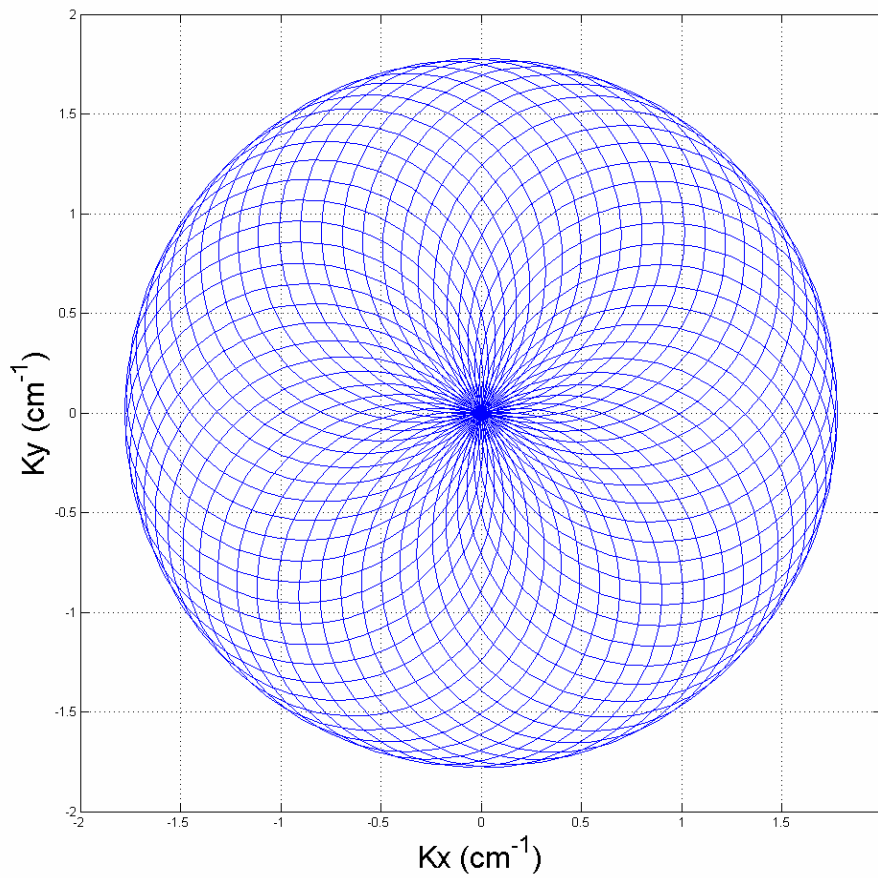
Figure 3-2 Multishot Rosette: K-t space 3D view $N_x = N_y = 64$, $fov = 18cm$, $\Delta\delta = 600Hz$
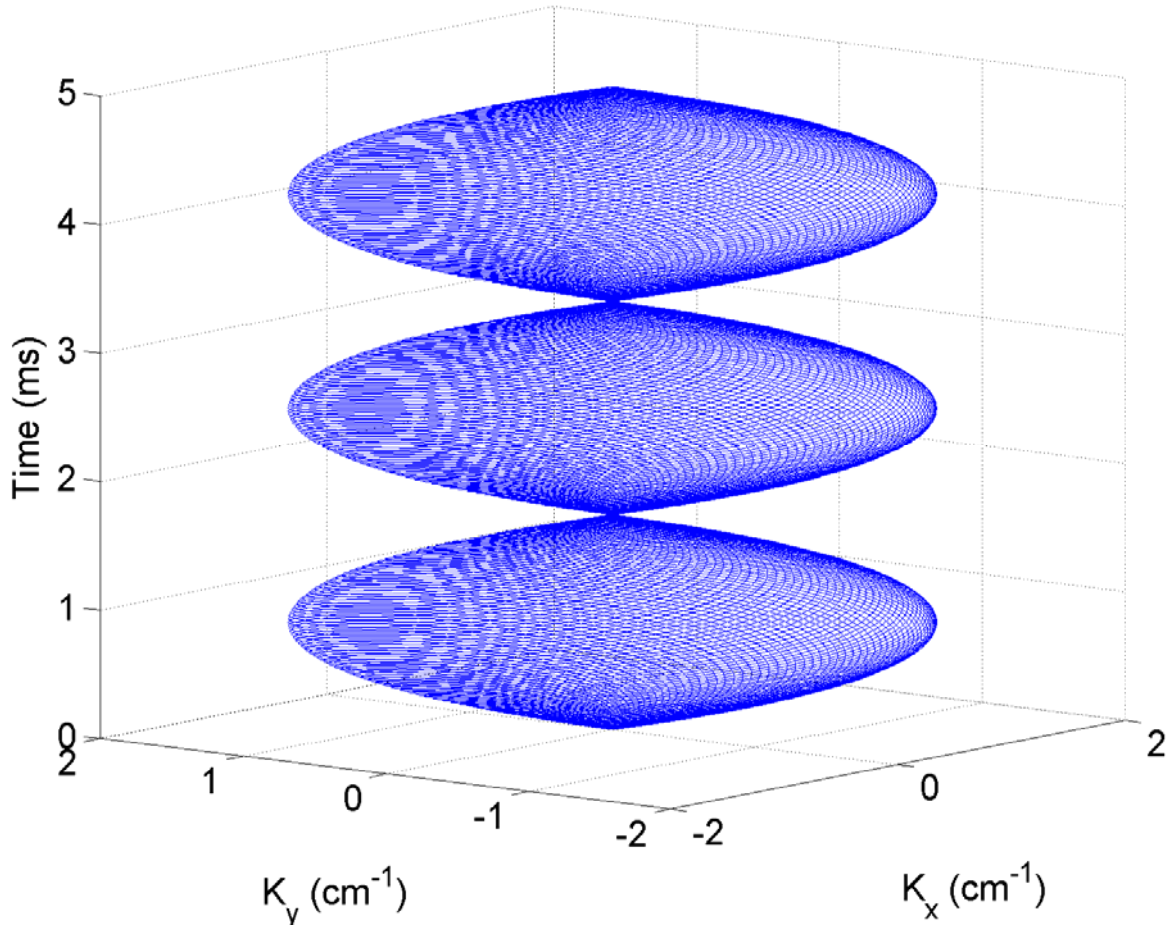
The radial distance $K_r(t)$ in K-space from $K = 0$ is:

$$K_r(t) = |\vec{K}(t)| = K_{max} \cdot \sin(\omega_1 t) \tag{3.2}$$

The gradient or the speed of the trajectory in K-space can be written [37]:

$$\vec{G}(t) = \frac{1}{\gamma} \cdot \frac{d\vec{K}(t)}{dt} = \frac{K_{max}}{2 \cdot \gamma} \cdot (\omega_+ \cdot e^{i \cdot \omega_+ \cdot t} + \omega_- \cdot e^{-i \cdot \omega_- \cdot t}) \tag{3.3}$$

$$\begin{aligned} \omega_+ &= \omega_1 + \omega_2 \\ \omega_- &= \omega_1 - \omega_2 \end{aligned} \tag{3.4}$$

The x and y gradient components (Figure 3-3) are $G_x(t) = \mathrm{Re}(\vec{G}(t))$ and $G_y(t) = \mathrm{Im}(\vec{G}(t))$:

$$G_x(t) = \frac{K_{max}}{2 \cdot \varkappa} \cdot (\omega_+ \cdot \cos(\omega_+ t) + \omega_- \cdot \cos(\omega_- t))$$

$$G_y(t) = \frac{K_{max}}{2 \cdot \varkappa} \cdot (\omega_+ \cdot \sin(\omega_+ t) - \omega_- \cdot \sin(\omega_- t))$$

(3.5)

The magnitude of the gradient as a function of time is:

$$G(t) = |\vec{G}(t)| = \sqrt{\vec{G}(t) \cdot \vec{G}^*(t)} = \frac{K_{max}}{\varkappa} \cdot \sqrt{\omega_1^2 \cdot \cos^2(\omega_1 t) + \omega_2^2 \cdot \sin^2(\omega_1 t)}$$

(3.6)

$$G(t) = \frac{K_{max} \cdot \omega_1}{\varkappa} \cdot \sqrt{1 - (1 - \frac{\omega_2^2}{\omega_1^2}) \cdot \frac{K_r^2(t)}{K_{max}^2}}$$

(3.7)

Therefore, the gradient along the trajectory will oscillate between a maximum value G_{max} and a minimum value G_{min}:

$$G_{max} = max(G(t)) = \frac{K_{max} \cdot max(\omega_1, \omega_2)}{\varkappa}$$

(3.8)

$$G_{min} = min(G(t)) = \frac{K_{max} \cdot min(\omega_1, \omega_2)}{\varkappa}$$

(3.9)

Unlike [37, 39] that found $G_{max} = K_{max} \cdot \omega_1 / \varkappa$, we allow for trajectories with $\omega_2 > \omega_1$.

Figure 3-3 Theoretical Gradient Waveforms ($\omega_2 / \omega_1 > 1$)

25
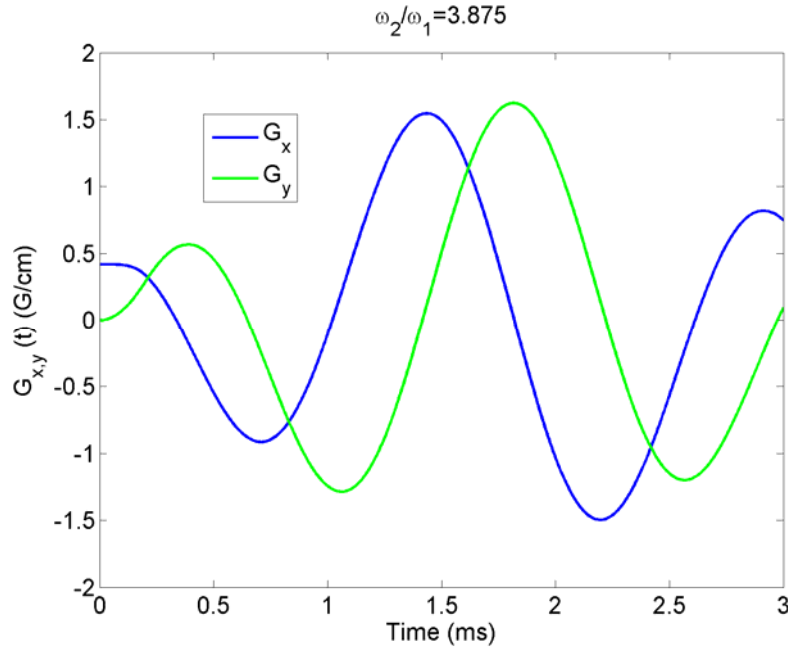
The radial $G_r(t)$ and tangential $G_g(t)$ component of the gradient vector, namely the component of the gradient along the line connecting $K = 0$ and the trajectory position at instant t, and the component perpendicular on this line respectively, are also useful quantities. They can be obtained by rotating $\vec{G}(t)$ to the new reference system:

$$\vec{G}^1(t) = e^{-i \cdot \omega_2 \cdot t} \cdot \vec{G}(t) = \frac{K_{max}}{2 \cdot \gamma} \cdot (\omega_+ \cdot e^{i \cdot \omega_1 \cdot t} + \omega_- \cdot e^{-i \cdot \omega_1 \cdot t}) \tag{3.10}$$

$$G_r(t) = \text{Re}(\vec{G}^1(t)) = \frac{K_{max}}{\gamma} \cdot \omega_1 \cdot \cos(\omega_1 t) \tag{3.11}$$

$$G_g(t) = \text{Im}(\vec{G}^1(t)) = \frac{K_{max}}{\gamma} \cdot \omega_2 \cdot \sin(\omega_1 t) \tag{3.12}$$

Alternatively, they can be obtained by observing that, if $dK_r(t)$ and $dK_g(t)$ are the radially and azimuthally infinitesimal small changes in $\vec{K}(t)$, and because the change in the azimuthal position on the trajectory is $d\vartheta = \omega_2 \cdot dt$:

$$G_r(t) = \frac{dK_r(t)}{\gamma \cdot dt} = \frac{K_{max}}{\gamma} \cdot \omega_1 \cdot \cos(\omega_1 t) \tag{3.13}$$

$$G_g(t) = \frac{dK_g(t)}{\gamma \cdot dt} = \frac{K_r(t) \cdot d\vartheta}{\gamma \cdot dt} = \frac{K_r(t)}{\gamma} \cdot \frac{d\vartheta}{dt} = \frac{K_{max} \cdot \sin(\omega_1 t)}{\gamma} \cdot \omega_2 \tag{3.14}$$

The acceleration along the trajectory, the rate at which the gradient changes, or the slew rate, is:

$$\vec{S}(t) = \frac{d\vec{G}(t)}{dt} = \frac{K_{max}}{2 \cdot \gamma} \cdot i \cdot (\omega_+^2 \cdot e^{i \cdot \omega_+ \cdot t} - \omega_-^2 \cdot e^{-i \cdot \omega_- \cdot t}) \tag{3.15}$$

$$S(t) = \sqrt{\vec{S}(t) \cdot \vec{S}^*(t)} = \frac{K_{max}}{2 \cdot \gamma} \cdot \sqrt{(\omega_+^2 + \omega_-^2)^2 - 4 \cdot \omega_+^2 \cdot \omega_-^2 \cdot \cos^2(\omega_1 t)} \tag{3.16}$$

The maximum and minimum slew rate along the trajectory is:

$$S_{max} = \frac{K_{max}}{2 \cdot \gamma} \cdot (\omega_+^2 + \omega_-^2) = \frac{K_{max}}{\gamma} \cdot (\omega_1^2 + \omega_2^2) \tag{3.17}$$

$$S_{min} = \frac{K_{max}}{2 \cdot \gamma} \cdot (\omega_+^2 - \omega_-^2) = \frac{K_{max}}{\gamma} \cdot 2 \cdot \omega_1 \cdot \omega_2 \tag{3.18}$$

3.2   ROSETTE TRAJECTORIES SPECTRAL RESPONSE

Ideally, in a spectroscopic imaging acquisition, the final reconstructed image should precisely reflect the spatial and spectral information in the imaged object. As will be shown in the data reconstruction section, Section 3.5, a reconstruction that is not optimal could result in artifacts and ghost resonances, phenomenon known as spectral leakage. However, even if an optimal reconstruction was employed, depending on the modality in which the K-t space was encoded, spectral information of an object at a resonant frequency could still appear at an off-resonance frequency. This is called the spectral response of an acquisition technique.

Using simulations, Noll [37] analyzed the spectral behavior of a multishot rosette trajectory with a data acquisition length equal to 2.5 radial oscillation periods per shot, each shot crossing the center of K-space six times. In this section, we further investigate the rosette spectral properties, for acquisitions using trajectories with longer readout periods (which cross the center of K-space a greater number of times). We theoretically explain how regular patterns of phase accumulation lead to the obtained spectral response function and that the same kind of response is to be expected from other self-rewinding trajectories used for 2D spectroscopic imaging.

The off-resonance behavior of the rosette acquisition technique is evaluated in two different ways. First, a simulation model similar to the one used by Noll [37] is used. Our simulation object consists of a large disk, with a superimposed ellipse, both of them on-resonance (Figure 3-4). The K-space data is generated noise free using analytical expressions for the 2DFT of an ellipse (equation(3.140)).

Figure 3-4 Spectral Response Simulated Object and Region of Interest (ROI)
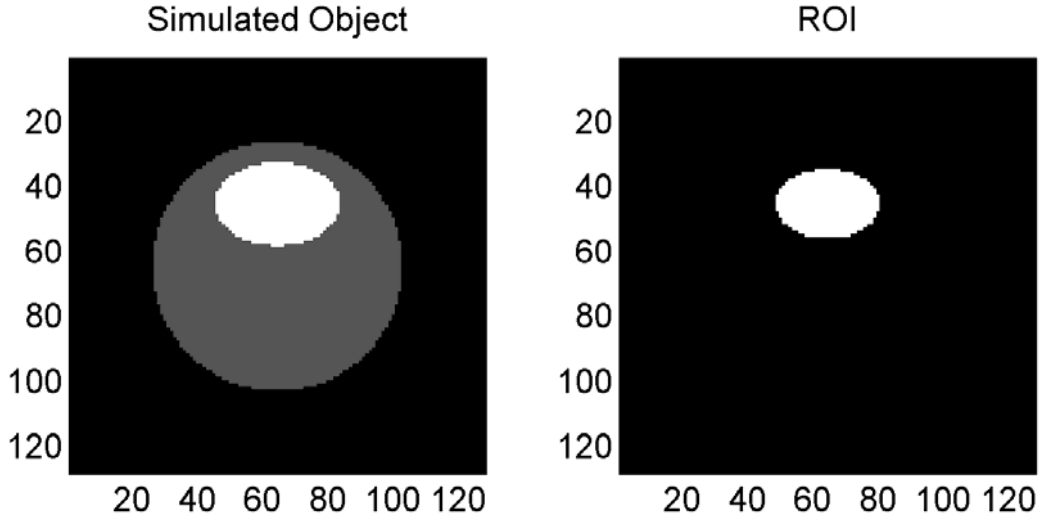
The trajectories are designed as in Section 3.3 and the number of shots used is the theoretical number derived in Section 3.4 (given by equation (3.83) or equation(3.87)). The data is modulated to several resonant frequencies $f = \omega/(2\pi)$ (by multiplying data with $e^{i\cdot\omega\cdot t}$), in the range zero to $2 \cdot f_1$ ($f_1 = \omega_1/(2\pi)$), and a two dimensional reconstruction is performed. For the simulations performed, the radial oscillation frequency is $f_1 = 300Hz$. The image intensity for the simulated object is calculated at each off-resonance frequency inside the ellipse in a region of interest (ROI) depicted in Figure 3-4. The length of the trajectories T_{read} is incrementally increased by $dT = 1/(2 \cdot f_1)$ and the procedure is repeated. The evaluated spectral response for trajectories with a length equal to $N_\delta = 5$ petals ($N_\delta/2 = 2.5$ radial oscillation, $N_\delta + 1 = 6$ $K = 0$ crossings), $N_\delta = 16$ petals (8osc. 17 cross.), $N_\delta = 32$ petals (16osc. 33 cross.) and $N_\delta = 64$ petals (32osc. 65 cross.), is presented in Figure 3-5 ($T_{read} = N_\delta \cdot dT$). The result for $N_\delta = 5$ is practically the same as the one obtained by Noll [37]. There are two reasons for the slight differences between the curve obtained by us ($N_\delta = 5$) and the one obtained by Noll.

28

While Noll used for reconstruction a ramp filter ($w_i \sim K_i$) as in projection imaging to pre-compensate the data, we used a more appropriate weighting function ($w_i \sim K_i \cdot \sqrt{K_{max}^2 - K_i^2}$ weights that are the same as the 3D Voronoi volumes associated with the data points – Section 3.4; see also Section 3.5 on importance of weighting function in data reconstruction). In addition, our trajectories have a somewhat higher K-t space sampling density. To form an image at the targeted spatial resolution, Noll's trajectories [37] with a length of 2.5 radial oscillations require a smaller number of excitations than our acquisition that requires every .5 (half) radial oscillations an image is generated (as described in Trajectory Design Section 3.3), and therefore require a greater number of excitations. From a 2D K-space perspective (37, 55), because our simulations use a larger number of trajectories, there are also a larger number of trajectory crossings where the phase accumulation takes place. Nevertheless, the main features of the spectral response function obtained by Noll and the one obtained by us for $N_\delta = 5$ are the same: the local maxima and minima in the studied frequency range (0 to $2 \cdot f_1$), correspond to the same locations in both cases.

Figure 3-5 Spectral Response function evaluated using modulation ($e^{i \cdot \omega \cdot t}$) + 2D reconstruction
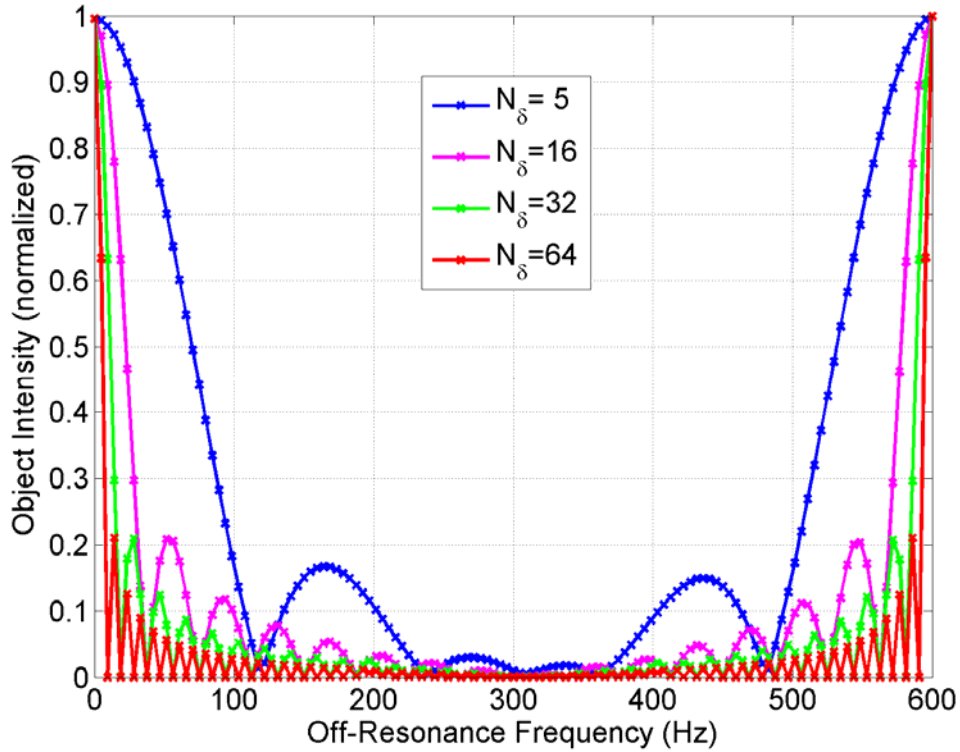
Using the same generated object, another way to evaluate the spectral response is by performing a three dimensional reconstruction, simultaneously resolving the two spatial dimensions and the spectral information. Data was zero padded along the time direction to obtain 128 spectral points in the range $-\Delta\delta/2$ to $\Delta\delta/2$ ($\Delta\delta = 2 \cdot f_1$ as discussed in Trajectory Design Section 3.3). The image intensity is evaluated in each spectral slice, in the same ROI as for the 2D reconstruction. The results for the zero to f_1 range are displayed in Figure 3-7 and can be compared to the results for the modulation plus 2D reconstruction in the same range (Figure 3-6, which is the left half of Figure 3-5). Regardless of the modality of reconstruction (modulation+2D or 3D), the spectral response measured exhibits the same behavior in either case.

Figure 3-6 Spectral Response evaluated using modulation + 2D recon (0 to f_1 range)
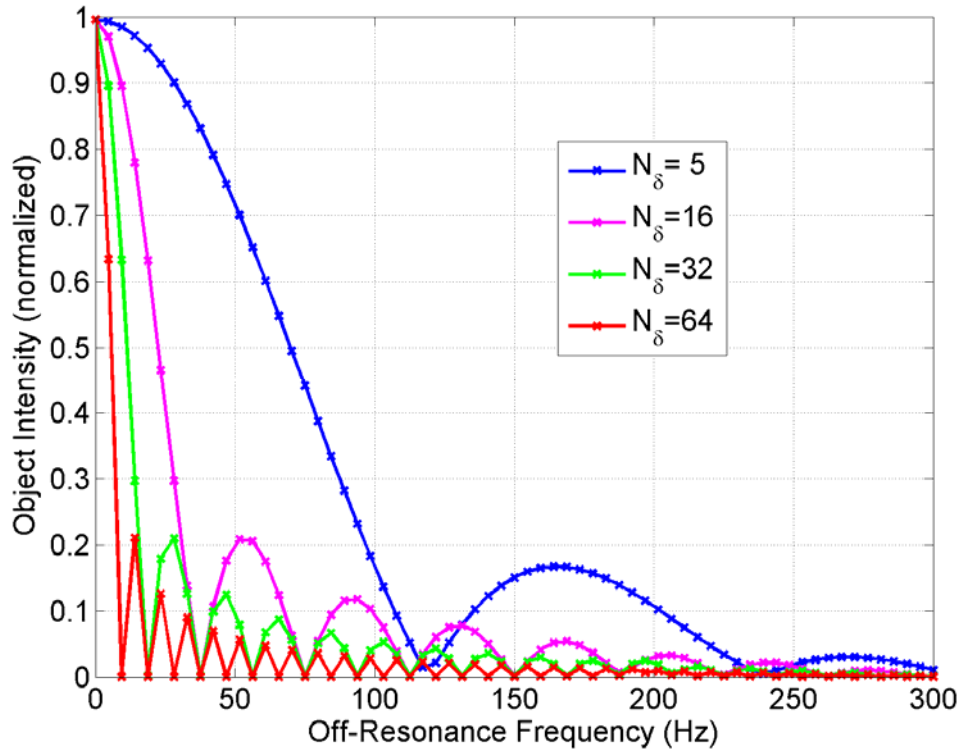
Figure 3-7 Spectral Response evaluated using 3D recon, zero-padded to 128 spectral points (0 to f_1)
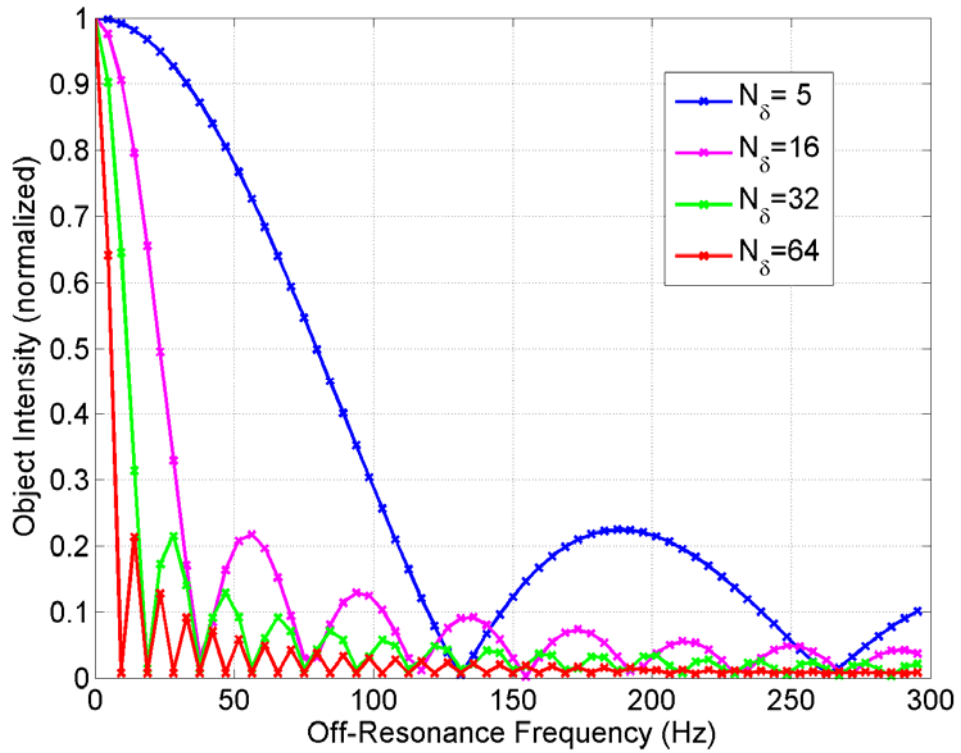
The results obtained in Figure 3-5 could be explained by looking at the data in K-t space. For an arbitrary position $\vec{k} = (k_x, k_y)$ in K-space (distance to the origin $0 < K_r \leq K_{max}$), there is a total of $2 \cdot N_\delta$ data points sampled at different time instants as seen in Figure 3-8. The K-t position of the sampled data is depicted by the thick blue lines. Temporal slices, as defined in Trajectory Design (Section 3.3) are delimited by the green horizontal line. The time axis at an arbitrary position K_r (red line), will be sampled twice within one temporal slice (not necessarily by the same trajectory but rather by one of the rotated trajectories of a multishot acquisition, following a later excitation). The yellow horizontal lines represent the position of the gridding planes on which acquired data is convoluted to make possible a reconstruction that uses a Fast Fourier Transform (FFT) algorithm as discussed in Data Reconstruction Section 3.5.

Figure 3-8 Profile of K-t space through $K = 0$, parallel to the time axis
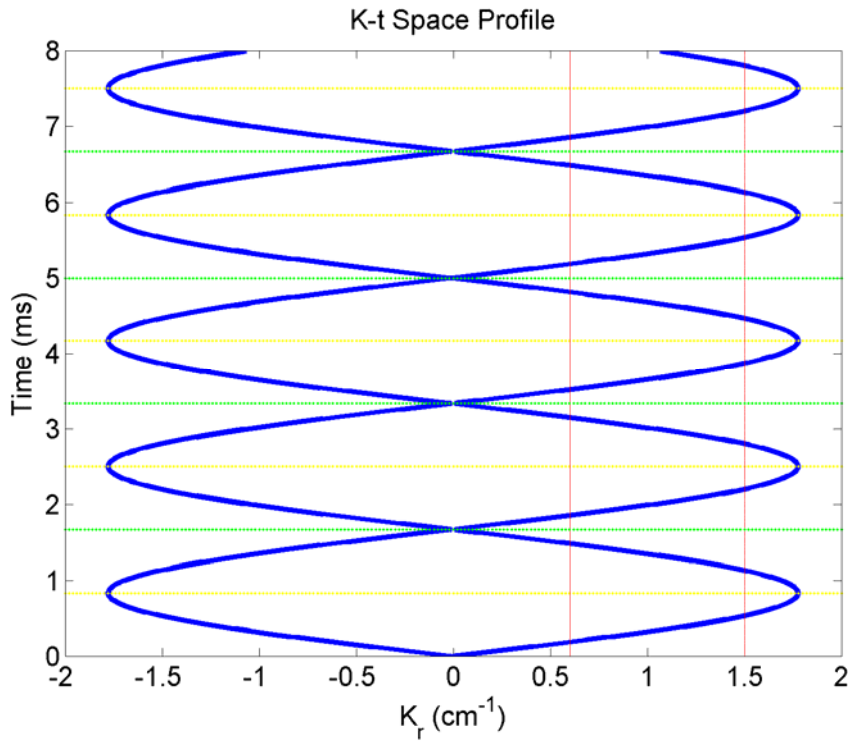
We consider points within the range $k_x \pm \Delta k_x / 2, k_y \pm \Delta k_y / 2$ ($\Delta k_x = \Delta k_y = 1 / fov$) being

the same, having the same signal $A_\alpha \cdot e^{i \cdot \varphi_\alpha}$ (for an ellipse this is given by equation(3.140)), and no

T_2 relaxation. For the modulation plus 2D reconstruction, the total off-resonant signal at that K-

space position can be written as:

$$S_\alpha = \sum_{j=1}^{2 \cdot N_\delta} A_\alpha \cdot e^{i \cdot \varphi_\alpha} \cdot e^{i \cdot \omega \cdot t_\alpha^{(j)}} = \sum_{j-=1}^{N_\delta} A_\alpha \cdot e^{i \cdot \varphi_\alpha} \cdot e^{i \cdot \omega \cdot t_\alpha^{(j-)}} + \sum_{j+=1}^{N_\delta} A_\alpha \cdot e^{i \cdot \varphi_\alpha} \cdot e^{i \cdot \omega \cdot t_\alpha^{(j+)}} \qquad (3.19)$$

$j-$ is the summation index for the data points below the yellow horizontal median lines

in Figure 3-8 and $j+$ for data points above these lines. Therefore, if $dT = 1/(2 \cdot f_1)$ is the distance

in time between two successive $K = 0$ crossings, and Δt_α is the distance between the sampling

instant and closest horizontal median line, t_{j-}^α and t_{j+}^α can be written as:

$$t_{j-}^\alpha = (j-1) \cdot dT + \frac{dT}{2} - \Delta t_\alpha \qquad (3.20)$$

$$t_{j-}^\alpha = (j-1) \cdot dT + \frac{dT}{2} + \Delta t_\alpha \qquad (3.21)$$

The sum in equation (3.19) becomes:

$$S_\alpha = A_\alpha \cdot e^{i \cdot \varphi_\alpha} \cdot \sum_{j=1}^{N_\delta} e^{i \cdot \omega \cdot ((j-1) \cdot dT + dT / 2)} \cdot (e^{-i \cdot \omega \cdot \Delta t_\alpha} + e^{i \cdot \omega \cdot \Delta t_\alpha}) \qquad (3.22)$$

$e^{-i \cdot \omega \cdot \Delta t_\alpha} + e^{i \cdot \omega \cdot \Delta t_\alpha} = 2 \cdot \cos(\omega \cdot \Delta t_\alpha)$, and the geometrical series in equation (3.22) can be

written in a simpler form:

$$\sum_{j=1}^{N_\delta} e^{i \cdot \omega \cdot ((j-1) \cdot dT + dT / 2)} = e^{i \cdot \omega \cdot dT / 2} \cdot \sum_{j=0}^{N_\delta - 1} e^{i \cdot \omega \cdot j \cdot dT} = e^{i \cdot \omega \cdot dT / 2} \cdot \frac{1 - e^{i \cdot \omega \cdot N_\delta \cdot dT}}{1 - e^{i \cdot \omega \cdot dT}} = \frac{1 - e^{i \cdot \omega \cdot N_\delta \cdot dT}}{e^{-i \cdot \omega \cdot dT / 2} - e^{i \cdot \omega \cdot dT / 2}} (3.23)$$

Noting that $e^{-i \cdot \omega \cdot dT / 2} - e^{i \cdot \omega \cdot dT / 2} = -2 \cdot i \cdot \sin(\omega \cdot dT / 2)$, we can write:

$$S_\alpha = A_\alpha \cdot e^{i \cdot \varphi_\alpha} \cdot \cos(\omega \cdot \Delta t_\alpha) \cdot \frac{(e^{i \cdot \omega \cdot N_\delta \cdot dT} - 1)}{i \cdot \sin(\omega \cdot dT / 2)} \qquad (3.24)$$

The contribution of the $\cos(\omega \cdot \Delta t_\alpha)$ term to the final reconstructed image is more difficult

to quantify because it involves both the off-resonance frequency and the Δt_α variable that

depends on the distance to the center of K-space, which takes values in between $\Delta t_\alpha = 0$ (at

$K_r = 0$)and $\Delta t_\alpha = dT / 2$ (at $K_r = K_{max}$). However, because of its position in the nominator in

expression (3.24), and because it is a smooth varying function in the range -1 to 1, its effect will

be less than the one of the faster varying function $e^{i \cdot \omega \cdot N_\delta \cdot dT} - 1$, and less than the contribution of

the $1 / \sin(\omega \cdot dT / 2)$ term which takes values in between $-\infty$ to ∞. The contribution to the final

image of these last two terms is independent of the position in K-space (α index), and depends

only on the off-resonance amount. Therefore, the spectral response function is approx. equal to:

$$f(\omega) = \frac{(e^{i \cdot \omega \cdot N_\delta \cdot dT} - 1)}{i \cdot \sin(\omega \cdot dT / 2)} = i \cdot \frac{(1 - e^{i \cdot \omega \cdot N_\delta \cdot dT})}{\sin(\omega \cdot dT / 2)} \qquad (3.25)$$

The $1 / \sin(\omega \cdot dT / 2)$ term has maxima at $\omega \cdot dT / 2 = n \cdot \pi$ ($n = 0, \pm 1, \pm 2, ...$), where it

diverges to infinity. In the range of frequencies analyzed (0 to $2 \cdot f_1$), using $dT = 1/(2 \cdot f_1)$

and $\omega = 2 \cdot \pi \cdot f$, the maxima correspond to $f = 0$ and $f = 2 \cdot f_1$. A minimum is obtained

at $\omega \cdot dT / 2 = \pi / 2$, or $f = f_1$.

The faster varying term $1 - e^{i \cdot \omega \cdot N_\delta \cdot dT} = 1 - e^{i \cdot \pi \cdot N_\delta \cdot f / f_1}$ is a periodic function that produces the

bumps in the spectral response function $|f(\omega)|$ (Figure 3-5), with maxima when

$e^{i \cdot \pi \cdot N_\delta \cdot f / f_1} = e^{i \cdot (2 \cdot n + 1) \cdot \pi} = -1$ ($n = 0, \pm 1, \pm 2, ...$). There will be a total of N_δ local maxima in the range

0 to $2 \cdot f_1$:

$$f_{max}^{(n)} = f_1 \cdot (2n + 1) / N_\delta, \quad n = 0, 1, 2, .., N_\delta - 1 \qquad (3.26)$$

The first maximum $f_{max}^{(n=0)} = f_1 / N_\delta$ and the last one $f_{max}^{(n=N_\delta - 1)} = 2 \cdot f_1 - (f_1 / N_\delta)$ cannot be

distinguished because $1 / \sin((\pi / 2) \cdot f / f_1)$ has a much stronger effect on the spectral response

where $1/\sin(x) \to 0$, and only a total of $N_\delta - 2$ local maxima will be visible. When N_δ is odd, the central local maximum falls exactly at f_1 and coincides with the minimum of $1/\sin((\pi/2) \cdot f/f_1)$, resulting in a rather non visible local maximum as seen for $N_\delta = 5$ in Figure 3-5.

The minima in the spectral response function $|f(\omega)|$ correspond to $e^{i \cdot \pi \cdot N_\delta \cdot f/f_1} = e^{i \cdot n \cdot 2 \cdot \pi} = 1$ ($n = 0, \pm 1, \pm 2, ...$). In the range considered (0 to $2 \cdot f_1$) this factor has $N_\delta + 1$ zeros positioned at the off-resonant frequencies ($n = 0$ for on-resonance):

$$f_{min}^{(n)} = 2 \cdot f_1 \cdot n / N_\delta = n/(N_\delta \cdot dT) = n/T_{read}, \quad n = 0, 1, 2, .., N_\delta \qquad (3.27)$$

Equation (3.27) is an important result because it provides the theoretical support for calculating the width of the spectral passband in which there is very little degradation of the object. The second zero, is the inverse of the trajectory readout duration $T_{read} = N_\delta \cdot dT$, the same as the result measured by Scheffler [55] in the context of randomized stochastic trajectories, and by Noll [37], and as can be seen in our results in Figure 3-5:

$$f_{min}^{(n=1)} = 2 \cdot f_1 / N_\delta = 1/(dT \cdot N_\delta) = 1/T_{read} \qquad (3.28)$$

For $f = 0$ and $f = 2 \cdot f_1$, the spectral function can be calculated as a limit of type $0/0$. Using $\sin(\omega \cdot dT / 2) = \sin((\pi/2) \cdot f / f_1)$ and the limits $\lim_{x \to 0} e^x \approx 1 + x$ and $\lim_{x \to 0}(\sin(x)) \approx x$:

$$\lim_{\omega \to 0} f(\omega) = i \cdot \frac{1 - (1 + i \cdot \pi \cdot N_\delta \cdot f / f_1)}{(\pi/2) \cdot f / f_1} = 2 \cdot N_\delta \qquad (3.29)$$

The same result is obtained in the limit $f = 2 \cdot f_1$. Normalizing the spectral function to this maximum, it becomes evident that for a trajectory with fixed dT (and therefore fixed radial oscillation frequency $f_1 = \omega_1 /(2\pi)$), increasing the acquisition duration $T_{read} = N_\delta \cdot dT$, and thus

the number of times ($N_\delta + 1$) the trajectories cross the center of K-space $K = 0$, produces a better

off-resonance behavior:

$$f_N(\omega \neq 0) = \frac{f(\omega)}{\max(f(\omega))} = \frac{f(\omega)}{f(\omega = 0)} = \frac{f(\omega)}{2 \cdot N_\delta} = \ \sim \ 1/N_\delta \qquad (3.30)$$

Using some simple trigonometric relations, the magnitude ($|\cdot|$) of the normalized

spectral response function, can be written as:

$$|f_N(\omega)| = \frac{1}{N_\delta} \cdot \left| \frac{\sin(\dfrac{\omega \cdot N_\delta \cdot dT}{2})}{\sin(\dfrac{\omega \cdot dT}{2})} \right| \qquad (3.31)$$

While the on-resonance normalized response function is the same at $\omega = 0$ regardless

of N_δ, $f_N(\omega = 0) = 1$, the local off-resonance maxima (equation(3.26)) become smaller (for the

same amount of off-resonance ω), as N_δ increases (see results Figure 3-5).

When performing a 3D reconstruction at the frequency resolution $df = 1/T_{read}$

and N_δ spectral points in the range $-\Delta\delta/2$ to $\Delta\delta/2$, because the spectral response function

minima (equation(3.27)) are exactly located at the same positions as the reconstructed spectral

slices, the reconstructed object will appear only in the on-resonance spectral slice (Figure 3-9).

Figure 3-9 Trajectory length $N_\delta = 36$ petals, 3D reconstruction spectral resolution $df = 1/T_{read}$
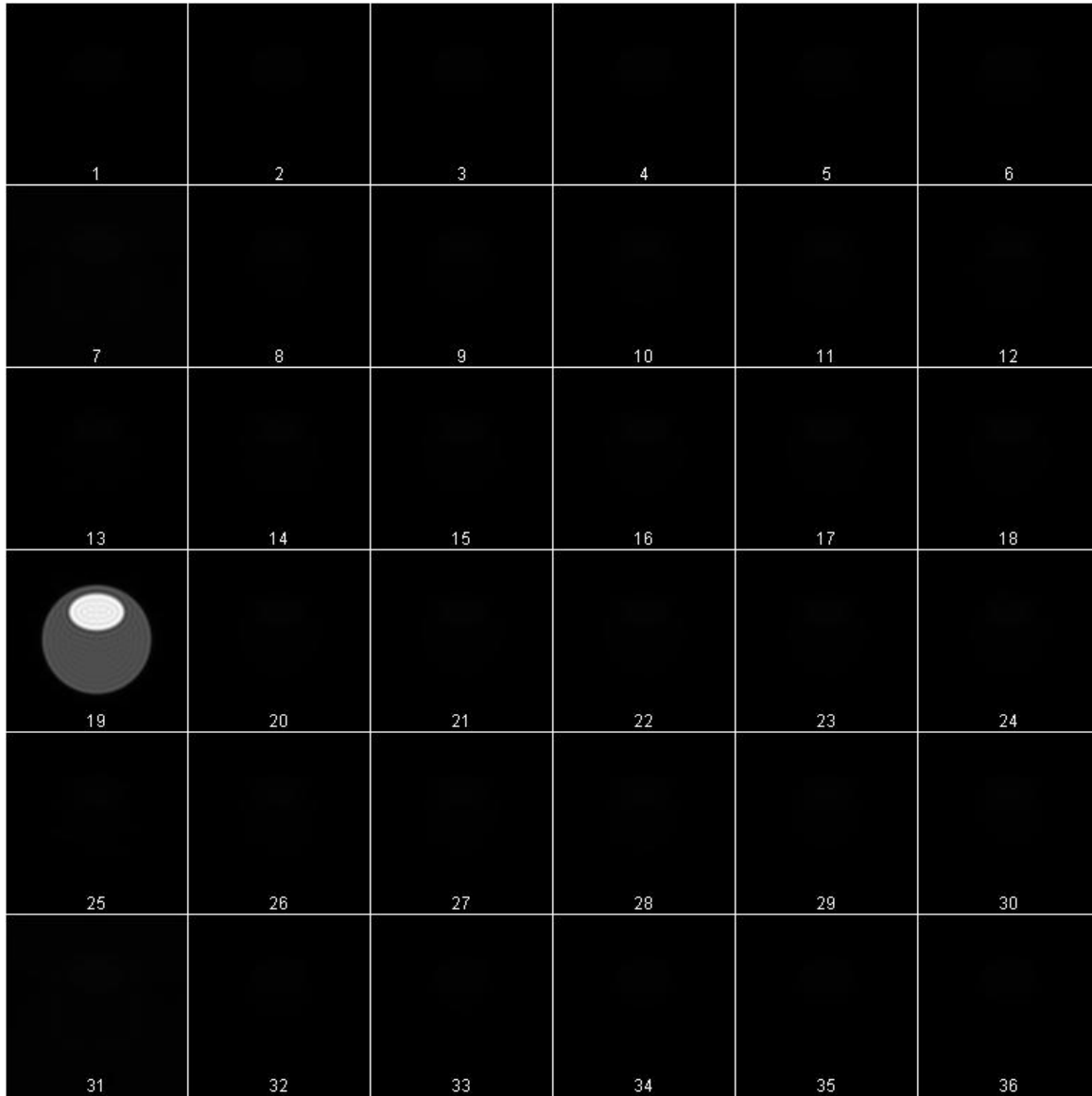
However, this result does not mean the 3D reconstruction is the solution to an acquisition with a problematic spectral response (e.g. an acquisition with large off-resonance response, as the one obtained for lower N_δ's). If the modulation plus 2D reconstruction was performed only at off-resonance frequencies in steps equal to $df = 1/T_{read}$, because they correspond to the minima positions (equation (3.27)), the evaluated spectral function would be a close to zero flat line except on-resonance, regardless of the trajectory length (determined by N_δ for a fixed dT).

For the 3D reconstruction, zero padding the temporal data and reconstructing at a smaller frequency resolution, reveals the otherwise hidden points in the spectral response function (Figure 3-7 and Figure 3-10).

Figure 3-10 Trajectory length $N_\delta = 36$ **petals, 3D recon, spectral resolution** $df = 1/4/T_{read}$
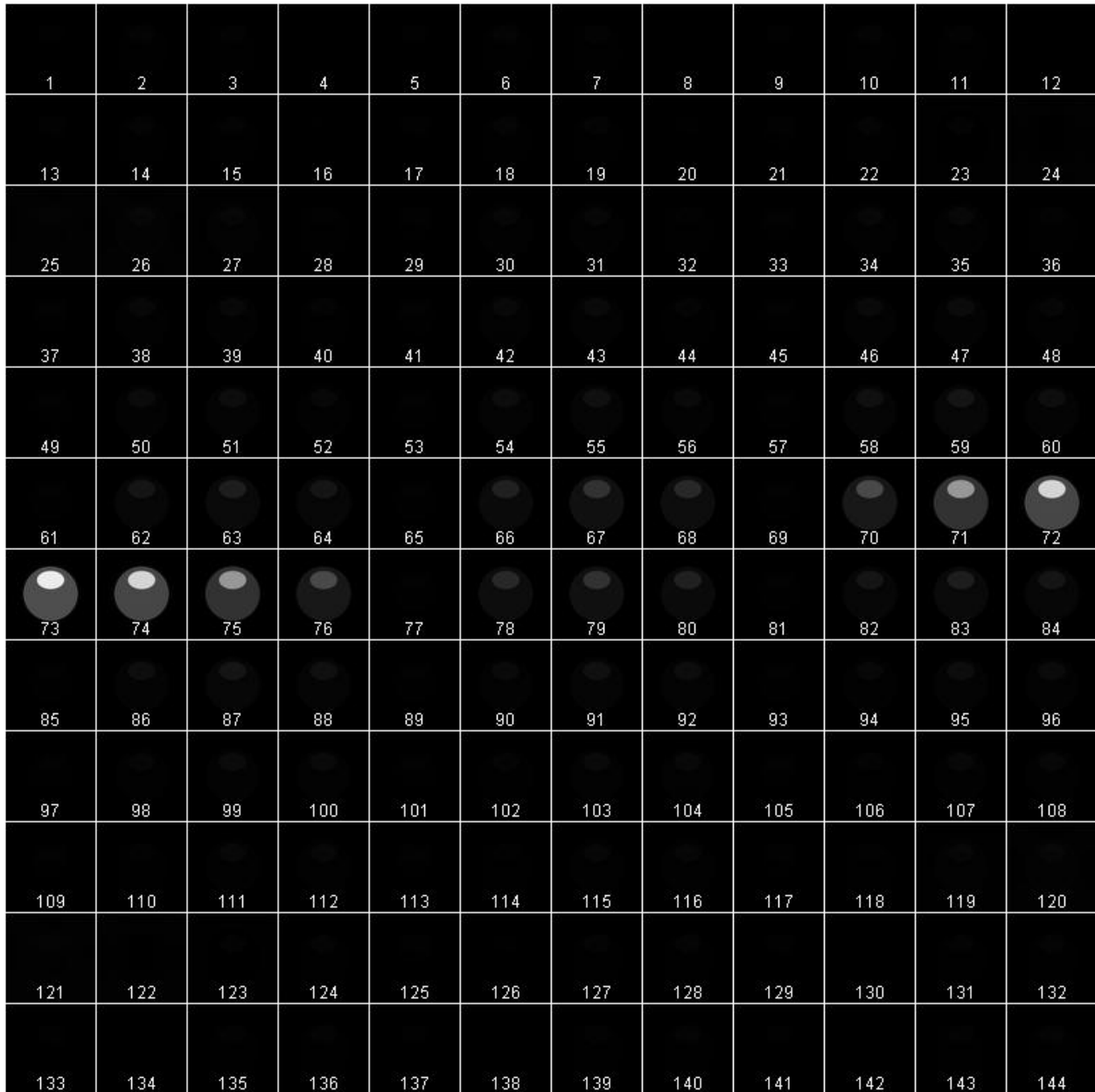
We did not consider the effect of the T_2 relaxation in equation(3.19) (total off-resonant

signal at a position α in K-space). If the T_2 effect is considered, equation(3.19) becomes:

$$S_\alpha = \sum_{j=1}^{2 \cdot N_\delta} A_\alpha \cdot e^{-t_\alpha^{(j)}/T_2} \cdot e^{i \cdot \varphi_\alpha} \cdot e^{i \cdot \omega \cdot t_\alpha^{(j)}} = \sum_{j=1}^{2 \cdot N_\delta} A_\alpha \cdot e^{i \cdot \varphi_\alpha} \cdot e^{i \cdot (\omega + \frac{i}{T_2}) \cdot t_\alpha^{(j)}} \tag{3.32}$$

Rather than carrying out all the calculations again, we note that $\omega \to \omega + i/T_2$, and

equation(3.24), becomes:

$$S_\alpha = A_\alpha \cdot e^{i \cdot \varphi_\alpha} \cdot \cos((\omega + \frac{i}{T_2}) \cdot \Delta t_\alpha) \cdot \frac{(e^{i \cdot (\omega + \frac{i}{T_2}) \cdot N_\delta \cdot dT} - 1)}{i \cdot \sin((\omega + \frac{i}{T_2}) \cdot dT / 2)} \tag{3.33}$$

The spectral response function in equation(3.25) can be written as:

$$f(\omega, T_2) = i \cdot \frac{(1 - e^{i \cdot (\omega + \frac{i}{T_2}) \cdot N_\delta \cdot dT})}{\sin((\omega + \frac{i}{T_2}) \cdot dT / 2)} = i \cdot \frac{(1 - e^{-N_\delta \cdot dT / T_2} \cdot e^{i \cdot \omega \cdot N_\delta \cdot dT})}{\sin(\omega \cdot dT / 2 + i \cdot dT / 2 / T_2)} \tag{3.34}$$

Using $\sin(i \cdot x) = i \cdot \sinh(x)$ and $\cos(i \cdot x) = -i \cdot \cosh(x)$, with $\sinh(x) = (e^x - e^{-x})/2$ and

$\cosh(x) = (e^x + e^{-x})/2$:

$$\sin(x + i \cdot y) = \sin(x) \cdot \cos(i \cdot y) + \cos(x) \cdot \sin(i \cdot y) = -i \cdot \sin(x) \cdot \cosh(y) + i \cdot \cos(x) \cdot \sinh(y) \tag{3.35}$$

$$f(\omega, T_2) = \frac{(1 - e^{-N_\delta \cdot dT / T_2} \cdot e^{i \cdot \omega \cdot N_\delta \cdot dT})}{\cos(\omega \cdot dT / 2) \cdot \sinh(dT / 2 / T_2) - \sin(\omega \cdot dT / 2) \cdot \cosh(dT / 2 / T_2)} \tag{3.36}$$

For an acquisition with a trajectory length $N_\delta = 36$ petals (37 $K = 0$ crossings), the

spectral response function was evaluated in the range 0 to $2 f_1 = 600 Hz$ at $145 = 36 \cdot 4 + 1$ off-

resonance points, using a $T_2 = T_{AQ} / 1.26$. The result is presented in Figure 3-11. The spectral

39

response for the same acquisition parameters but without T_2 relaxation was included for comparison. The 3D evaluation in the range $-\Delta\delta/2 = -f_1$ to $\Delta\delta/2 = f_1$ yields a similar result.

Figure 3-11 Spectral response with T_2 relaxation (modulation $e^{i\cdot\omega\cdot t}$ +2D reconstruction)
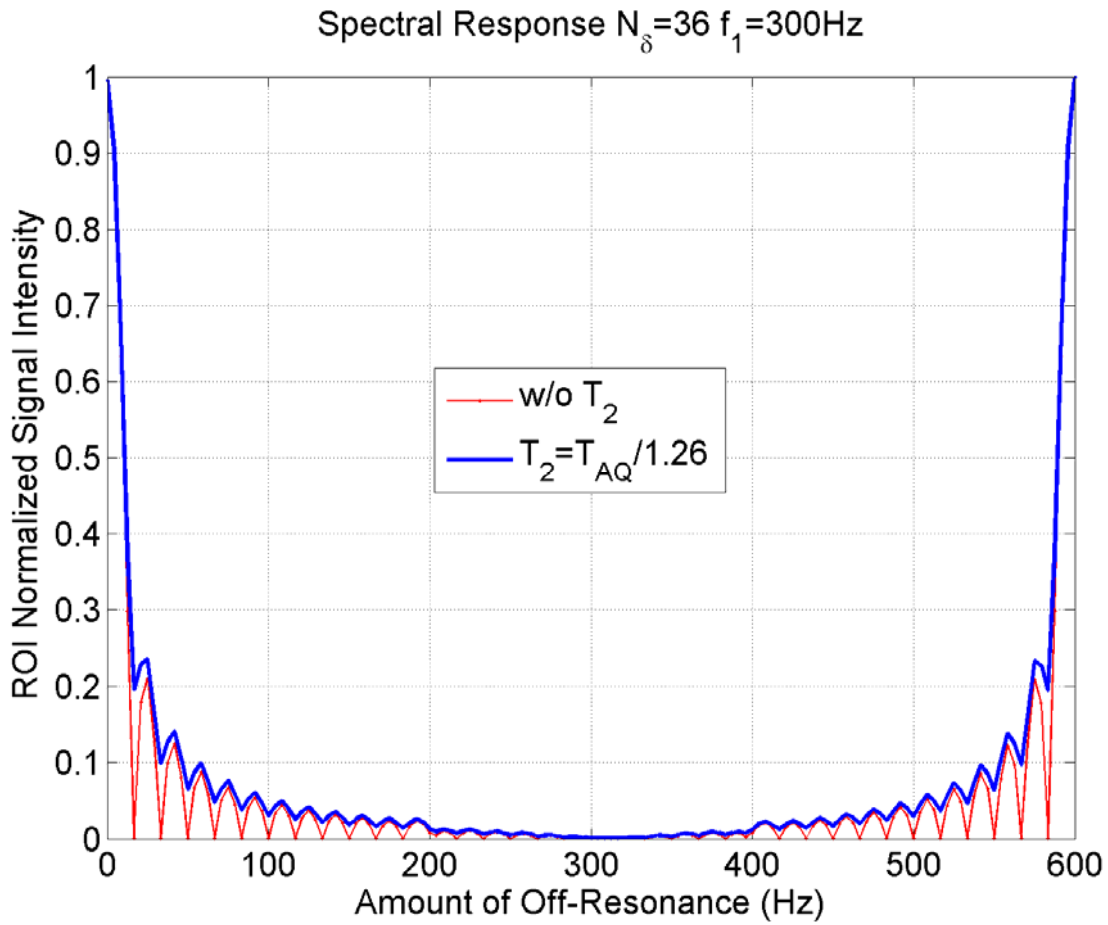
We have seen in this section that using longer trajectories, that cross $K = 0$ a greater number of times, improves the spectral response function. However, in a spectroscopic imaging experiment, the readout (or acquisition) time cannot be indefinitely long and is usually up to three times the relaxation time T_2^*. For free induction decays acquisition, for highest SNR per unit time, the optimal readout is $T_{AQ} = 1.26 \cdot T_2^*$, and for spin echo acquisitions $T_{AQ} = 2.52 \cdot T_2^*$. For

a fixed acquisition time, one way to increase the number of times the trajectory crosses the center of K-space is by increasing the radial oscillation frequency f_1, since $N_\delta = T_{AQ}/dT = T_{AQ} \cdot 2f_1$, or $N_\delta = T_{AQ} \cdot \Delta\delta$. However, for a fixed T_{AQ}, increasing f_1, results in an increase in the spectral bandwidth $\Delta\delta = 2 \cdot f_1$, while the spectral response for the same amount of off-resonance (in the original $\Delta\delta$) remains the same, as can be seen in Figure 3-12.

Figure 3-12 Spectral Response for a trajectory with same $T_{AQ} = 26.67ms$, twice $K = 0$ crossings
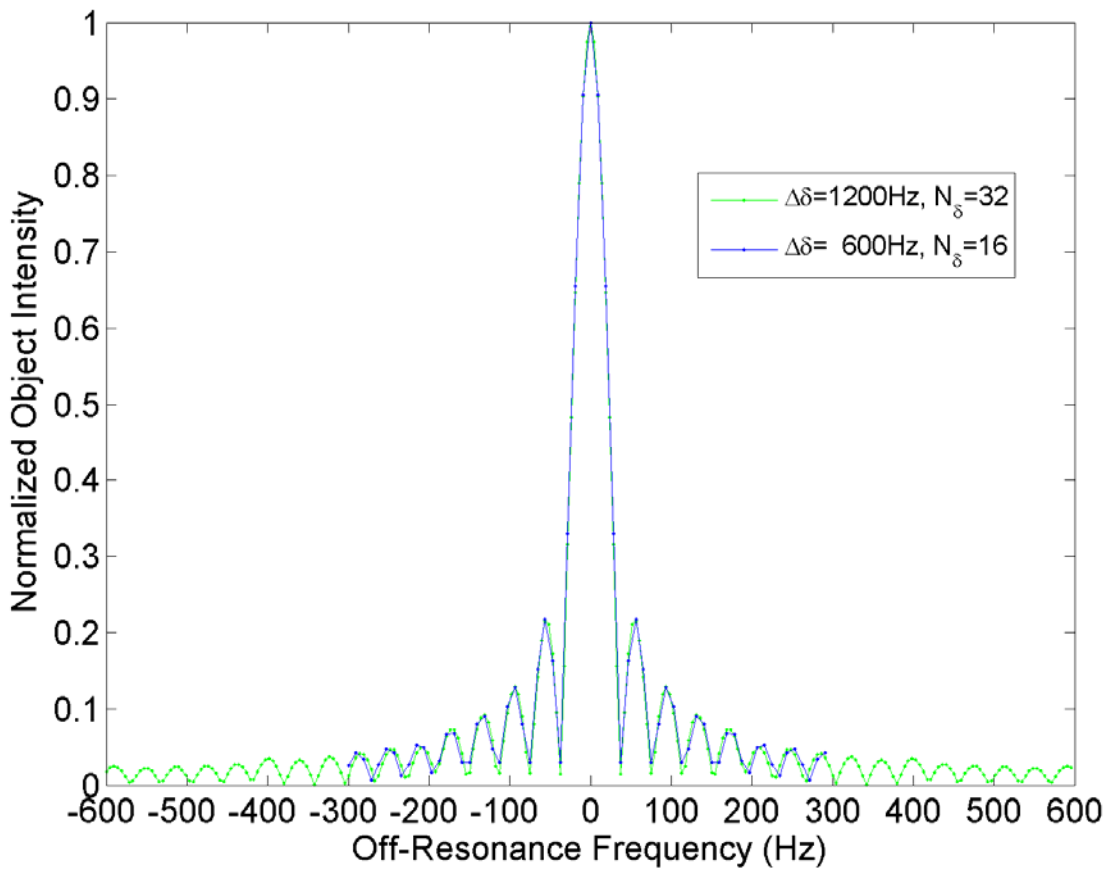
Due to its spectral response, the RSI acquisition might find it difficult to resolve metabolites with very short T_2^*'s and that are very close in frequency, but this is a problem for any spectroscopic method and techniques applied in these situations (like spectral editing, etc.)

41

could also be combined with RSI. For water-fat resonances separated by $\sim 450Hz$ at 3Tesla, an acquisition with only $N_\delta = 16$ petals and a spectral bandwidth $\Delta\delta = 600Hz$ (sufficient to separate the two resonances) corresponding to a readout as short as $T_{AQ} = 26.67ms$, has an off-resonance response at $f = 450Hz$ of approximately 6-7% (Figure 3-5). This figure represents how much the water/fat will contribute as background noise to the fat/water image. For comparison, Noll used an acquisition where the local peaks in the spectral response function have been reduced from ~15-20% to about 6-8% through a trajectory time delay scheme [37], or for a two shot acquisition, positioning the trajectories at an angle of 90^0 [39], rather than 180^0 that would provide more uniform angular coverage of K-space. The figure of ~6-7% for the spectral response function for $N_\delta = 16$ at $f = 450Hz$ is further improved when using longer readouts as seen in Figure 3-5 for $N_\delta = 32$ (~4%) and $N_\delta = 64$ (~2%). Optimally, for an RSI acquisition that resolves only two spectral resonances, because the spectral response function always has a minimum at $f_1 = \Delta\delta/2$ (Figure 3-5), the trajectories should be designed (Section 3.3) such the acquisition spectral bandwidth $\Delta\delta$ is twice the separation in frequency of the two resonances.

Looking at the result in equation(3.31), an interesting analogy with optical diffraction on N slits can be made. The observed amplitude at angle ϑ, for light of wavelength λ diffracted on N infinitely extended slits with opening a, with a distance between slits d is:

$$A(\vartheta) = A_0 \cdot \sin c(\frac{\pi a}{\lambda}\sin\vartheta) \cdot \frac{\sin(\frac{N\pi d}{\lambda}\sin\vartheta)}{\sin(\frac{\pi d}{\lambda}\sin\vartheta)} \tag{3.37}$$

The K-t space trajectories act like an optical diffraction grid for the off-resonance frequency ω, with N_δ infinitely thin slits ($a = 0$), with a separation between slits equal to dT.

While the results presented in this section correspond to rosette trajectories acquisitions, from the theoretical treatment of the spectral response function, it can be seen that the same kind of off-resonance behavior is to be expected from any spectroscopic imaging technique that uses self-rewinding trajectories that periodically sample the center and edges of K-space. The K-t profile parallel to the time axis through $K = 0$ for these techniques will look similar to the one depicted in Figure 3-8, and it is merely the $\Delta t_\alpha = \Delta t_\alpha(K_r)$ in equation (3.22) that will vary according to a function that is different than the one for the rosette trajectories.

3.3   TRAJECTORY DESIGN

As discussed in Chapter 2.0 , it is very important that K-t space be properly sampled to achieve the desired spatial resolution and spectral bandwidth. From Figure 3-2 where the rosette trajectories are depicted in K-t space, it can be seen that the largest separation along time axis between successive sampled points with same (K_x, K_y) position corresponds to data points at the center ($K = 0$) and the ones at the edge of K-space ($K_r = K_{max}$). This can also be seen in Figure 3-8, by looking at the intersection of sampling trajectories with the time axis (vertical red lines). The time separation between two successive $K = 0$ crossings is equal to half the radial oscillation period, thus $dT = 1/(2 \cdot f_1)$. According to the Shannon-Nyquist sampling theorem, this distance in time will dictate the largest spectral bandwidth $\Delta\delta = 1/dT = 2 \cdot f_1$ at which the reconstructed data will not exhibit spectral aliasing artifacts. Because the maximum speed along the trajectory

43

$G_{\max}$ is limited by either the signal bandwidth/sampling requirements or by hardware constraints (maximum scanner gradient $G_{\max} \le G_{\max}^{HW}$ and slew rate $S_{\max} \le S_{\max}^{HW}$), there will be a maximum achievable spectral bandwidth $\Delta\delta_{\max}$ for a given set of imaging parameters fov, N_x.

Because $\Delta\delta = 2 \cdot f_1$, trying to achieve the highest possible bandwidth is equivalent to using the highest possible radial oscillation frequency $f_1 = \omega_1 /(2\pi)$, or with trying to get as fast as possible from the center of K-space, to the edge and back to the center. In this case, depending on the imaging parameters, the trajectories might look like straight lines, since we want the angular oscillation frequency $f_2 = \omega_2 /(2\pi)$ to contribute as little as possible to the slew rate value (equation(3.17)). In fact, to allow for maximum $\omega_1 = 2\pi \cdot f_1 = \pi \cdot \Delta\delta$, by setting $\omega_2 = 0$ in equation(3.17), the requirement $S_{\max} \le S_{\max}^{HW}$ can be written ($K_{\max} = N_x /2/ fov$):

$$\frac{K_{\max}}{\gamma} \cdot \omega_1^2 = \frac{K_{\max}}{\gamma} \cdot (\pi \cdot \Delta\delta)^2 \le S_{\max}^{HW} \tag{3.38}$$

$$\Delta\delta_{\max}^{SR} = \frac{\sqrt{S_{\max}^{HW} \cdot \gamma / K_{\max}}}{\pi} = \frac{1}{\pi} \cdot \sqrt{\frac{2 \cdot S_{\max}^{HW} \cdot \gamma \cdot fov}{N_x}} \tag{3.39}$$

Setting $\omega_1 > \omega_2$ in equation(3.8), $G_{\max} \le G_{\max}^{HW}$ translates into:

$$\frac{K_{\max}}{\gamma} \cdot \omega_1 = \frac{K_{\max}}{\gamma} \cdot (\pi \cdot \Delta\delta) \le G_{\max}^{HW} \tag{3.40}$$

$$\Delta\delta_{\max}^{grad} = \frac{G_{\max}^{HW} \cdot \gamma}{\pi \cdot K_{\max}} = \frac{2 \cdot G_{\max}^{HW} \cdot fov \cdot \gamma}{\pi \cdot N_x} \tag{3.41}$$

The signal bandwidth Δf has to be smaller or equal to the sampling rate $1/dt$ (equation(2.41)) at any moment along the trajectory. The largest signal bandwidth will correspond to the largest gradient $G_{\max}$. Therefore,

$$\Delta f = \gamma \cdot G_{\max} \cdot fov + \Delta\delta = 1/dt \tag{3.42}$$

Since $\omega_1 = \pi \cdot \Delta\delta$, for $\omega_1 > \omega_2$, $G_{max} = N_x \cdot \pi \cdot \Delta\delta / \gamma / 2 / fov$ and equation (3.42) becomes:

$$N_x \cdot \pi \cdot \Delta\delta / 2 + \Delta\delta = 1/dt \tag{3.43}$$

$$\Delta\delta_{max}^{samp} = \frac{1}{dt \cdot (1 + \pi \cdot N_x / 2)} \tag{3.44}$$

The highest achievable spectral bandwidth for a field of view fov and a spatial resolution N_x is:

$$\Delta\delta_{max} = \min(\Delta\delta_{max}^{samp}, \Delta\delta_{max}^{grad}, \Delta\delta_{max}^{SR}) \tag{3.45}$$

The results in equations(3.39),(3.41),(3.44) were derived for one set of trajectories that start after the same time T_E, with respect to the RF excitation. It is apparent from these equations that, everything else being the same, as the spatial resolution increases, the maximum achievable spectral bandwidth decreases. However, adding a second set of trajectories starting at a time $T_E + dT/2$, also called temporal interleave, the largest separation along time axis between successive sampled points with same (K_x, K_y) position is halved (Figure 3-13), which in turn, increases the spectral bandwidth by a factor of two. This kind of acquisition (using two temporally interleaved sets of trajectories) will be demonstrated experimentally in Section 3.8 and Chapter4.0

Figure 3-13 Two sets of trajectories temporally interleaved $n_{TI} = 2$
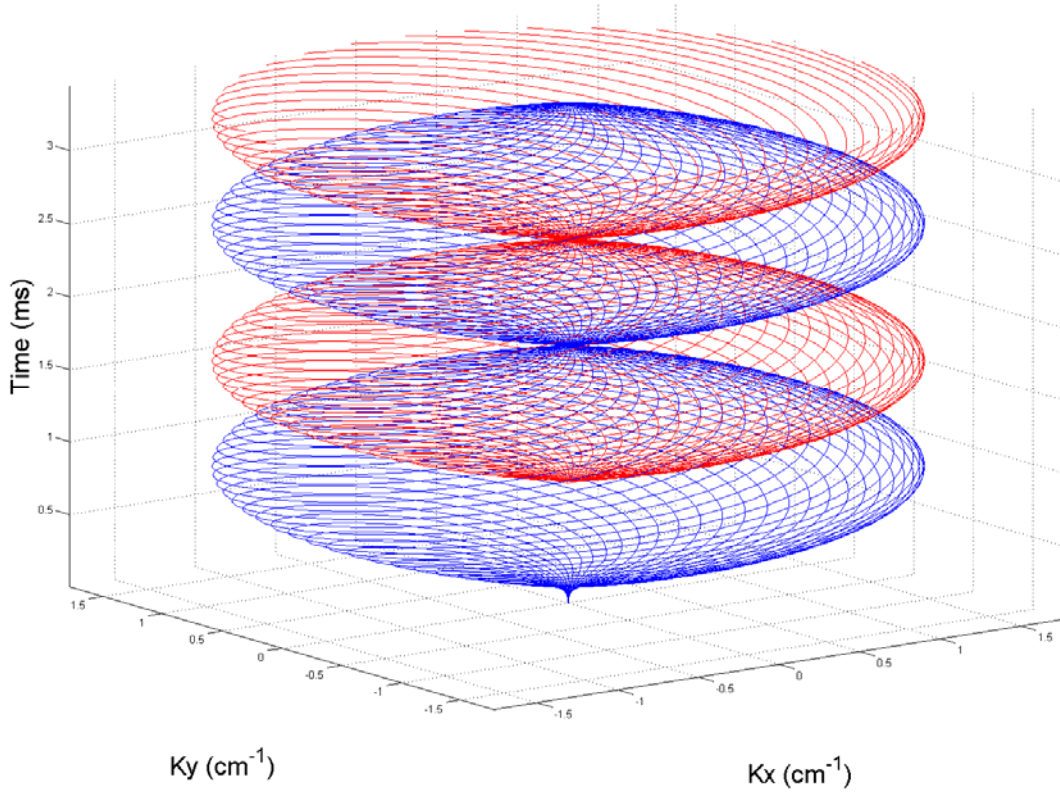
In general, a number n_{TI} of temporal interleaved sets of trajectories, spaced apart in time $dT / n_{TI} = 1/(n_{TI} \cdot 2 f_1)$, could be used. The corresponding spectral bandwidth is $\Delta \delta = n_{TI} \cdot 2 f_1$.

Therefore, $\omega_1 = 2\pi \cdot f_1 = \pi \cdot \Delta \delta / n_{TI}$. Equations(3.39),(3.41),(3.44) become:

$$\Delta \delta_{max}^{SR} = \frac{n_{TI}}{\pi} \cdot \sqrt{\frac{2 \cdot S_{max}^{HW} \cdot \gamma \cdot fov}{N_x}} \tag{3.46}$$

$$\Delta \delta_{max}^{grad} = \frac{n_{TI} \cdot 2 \cdot G_{max}^{HW} \cdot fov \cdot \gamma}{\pi \cdot N_x} \tag{3.47}$$

$$\Delta \delta_{max}^{samp} = \frac{1}{dt \cdot (1 + \dfrac{\pi \cdot N_x}{2 \cdot n_{TI}})} \tag{3.48}$$

The highest achievable spectral bandwidth when using n_{TI} temporally interleaved sets of trajectories, is the smallest of the ones allowed by the scanner slew rate(3.46), scanner maximum gradient(3.47), or signal bandwidth/sampling rate(3.48) constrains.

Figure 3-14 Maximum achievable spectral bandwidth ^{1}H ($\gamma = 42.576MHz/T$), $n_{TI} = 2$
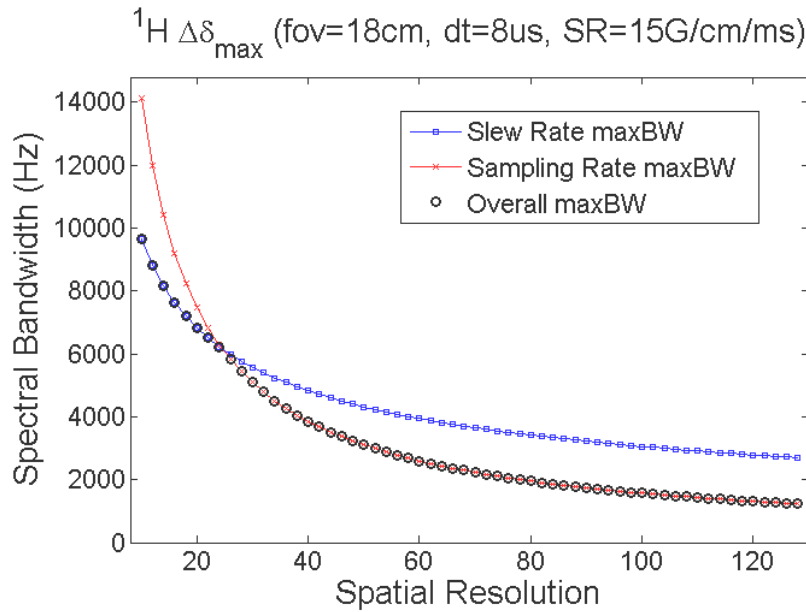
Figure 3-15 Maximum achievable spectral bandwidth ^{31}P ($\gamma = 17.235MHz/T$), $n_{TI} = 2$
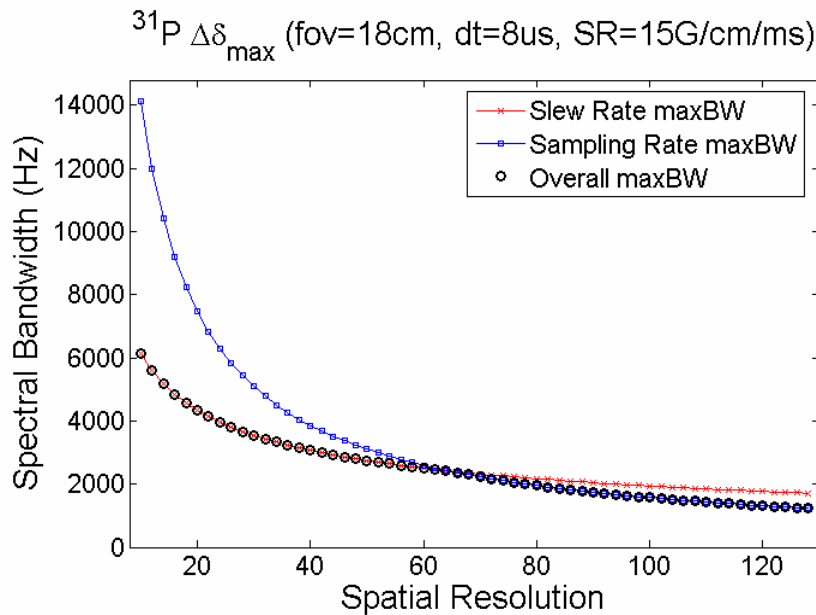
In Figure 3-14 and Figure 3-15, the maximum achievable spectral bandwidth using two ($n_{TI} = 2$) temporally interleaved sets of trajectories is presented for proton (^{1}H) and Phosphorous (^{31}P) RSI, as a function of spatial resolution N_x. The field of view is $fov = 18cm$, the complex data points sampling rate is $dt = 8us$, the maximum scanner gradient is $G_{max}^{HW} = 4G/cm$ and maximum scanner slew rate is $S_{max}^{HW} = 15G/cm/ms$. For the parameters chosen, the signal bandwidth constraint (equation (3.42) imposed on the trajectory, requires a maximum gradient G_{max} that is smaller than G_{max}^{HW}, and $\Delta\delta_{max}^{grad}$ (equation(3.47)) is greater than $\Delta\delta_{max}^{samp}$ and $\Delta\delta_{max}^{SR}$ at all spatial resolutions and was not plotted here. For both proton (^{1}H, gyromagnetic ratio $\gamma = 42.576MHz/T$) and Phosphorous (^{31}P, $\gamma = 17.235MHz/T$), the achievable spectral bandwidth is limited at lower spatial resolutions by the slew rate, while at higher spatial resolutions it is the sampling rate $1/dt$ that determines $\Delta\delta_{max}$.

At this point, for a field of view fov, desired spatial resolution N_x and spectral bandwidth $\Delta\delta \leq \Delta\delta_{max}$, the highest sampling spatial frequency K_{max} and the radial oscillation frequency ω_1 in the trajectory equation (3.1) are determined:

$$K_{max} = N_x / 2 / fov \tag{3.49}$$

$$\omega_1 = 2\pi \cdot f_1 = \pi \cdot \Delta\delta / n_{TI} \tag{3.50}$$

To define fully the trajectory, the angular oscillation frequency $\omega_2 = 2\pi \cdot f_2$ needs to be chosen. In imaging [37], ω_2 is chosen such the numbers of radial and angular oscillations are prime numbers among themselves. This is to avoid inefficient sampling of K-space where one trajectory would have two petals overlapped, sampling the same positions in K-space twice (one petal is the portion of trajectory delimited by two successive $K = 0$ crossings). For example, if $\omega_2 = \omega_1 / 2$ or $\omega_2 = \omega_1 / 3$ and the trajectory is more than two or respectively three petals long, the

petals following the second or the third one would sample the same positions in K-space again and again, requiring a larger number of excitations N_{sh} to fully cover the rest of K-space. However, for spectroscopic imaging using rosette trajectories, this requirement (e.g. prime numbers) is not necessary. Even if all the petals of a trajectory would fall on top of each other, as they would for $\omega_2 = \omega_1$, and the trajectory would sample the exact same positions in K-space, they would be at different moments in time, which allows the encoding of the spectral information.

We require that data samples collected in the interval $dT = 1/\Delta\delta$ are sufficient for forming an image with the desired spatial resolution N_x over a field of view fov (more on this in the following section 3.4), such N_δ images are formed over the entire acquisition at different echo times, dT apart. As long as, at the most, only one petal is included in a temporal slice of thickness dT, there is no concern this trajectory segment would sample the same K-space positions again (except for $\omega_2 = 0$, e.g. straight line). For example, for two temporally interleaved sets of trajectories ($n_{TI} = 2$), each individual trajectory will have only half a petal in each temporal slice. That is because, from equation(3.50), $dT = 1/(4 \cdot f_1)$, thus the time thickness of a temporal slice is equal to a quarter of the radial oscillation period which is the same as the time it takes for a trajectory to travel from $K = 0$ to $K = K_{max}$ -outgoing trajectory segment (or from $K = K_{max}$ to $K = 0$-incoming). In Figure 3-16, the K-space sampling of one temporal slice is depicted with the blue color for the outgoing trajectories corresponding to one of the temporally interleaved sets and the red color corresponding to the incoming trajectories from the other interleaved set.

When, at the most, only one petal is included in a temporal slice of thickness dT, there is a lot of freedom in choosing the angular oscillation frequency ω_2. We can choose ω_2 to be as large as possible allowed by the hardware (and this includes values greater than ω_1). The trajectories with more twist (larger ω_2) will require fewer excitations N_{sh} to cover K-space in each temporal slice, and therefore the K-t space.

For $\Delta\delta \le \Delta\delta_{max}$ and ω_1 fixed by(3.50), equation(3.17) and $S_{max} \le S_{max}^{HW}$ yields the highest ω_2 allowed by the slew rate:

$$\omega_2^{SR} = \sqrt{(\frac{S_{max}^{HW} \cdot \gamma}{K_{max}})^2 - \omega_1^2} \qquad (3.51)$$

Because we can have $\omega_2 > \omega_1$ and therefore $G_{max} = K_{max} \cdot \omega_2 / \gamma$, $G_{max} \le G_{max}^{HW}$ yields:

$$\omega_2^{grad} = \frac{G_{max}^{HW} \cdot \gamma}{K_{max}} \qquad (3.52)$$

Observing the signal bandwidth/sampling rate requirement (equation(3.42)) yields:

$$G_{max} = \frac{(\frac{1}{dt} - \Delta\delta)}{\gamma \cdot fov} \qquad (3.53)$$

$$\omega_2^{samp} = \frac{G_{max} \cdot \gamma}{K_{max}} \qquad (3.54)$$

The largest angular oscillation frequency ω_2 meeting all the imposed requirements:

$$\omega_2^{max} = \min(\omega_2^{SR}, \omega_2^{grad}, \omega_2^{samp}) \qquad (3.55)$$

The slew rate usually dictates the largest ω_2 (equation(3.51)) for spectral bandwidths $\Delta\delta$ much smaller than $\Delta\delta_{max}$ and/or for smaller spatial resolutions N_x; otherwise it is the sampling rate (equation(3.54)) that determines ω_2. With the three variables K_{max},

ω_1 and ω_2 determined in the way prescribed above, the rosette trajectory (equation(3.1)) is fully defined.

Figure 3-16 K-space sampling of a temporal slice using two temporally interleaved sets
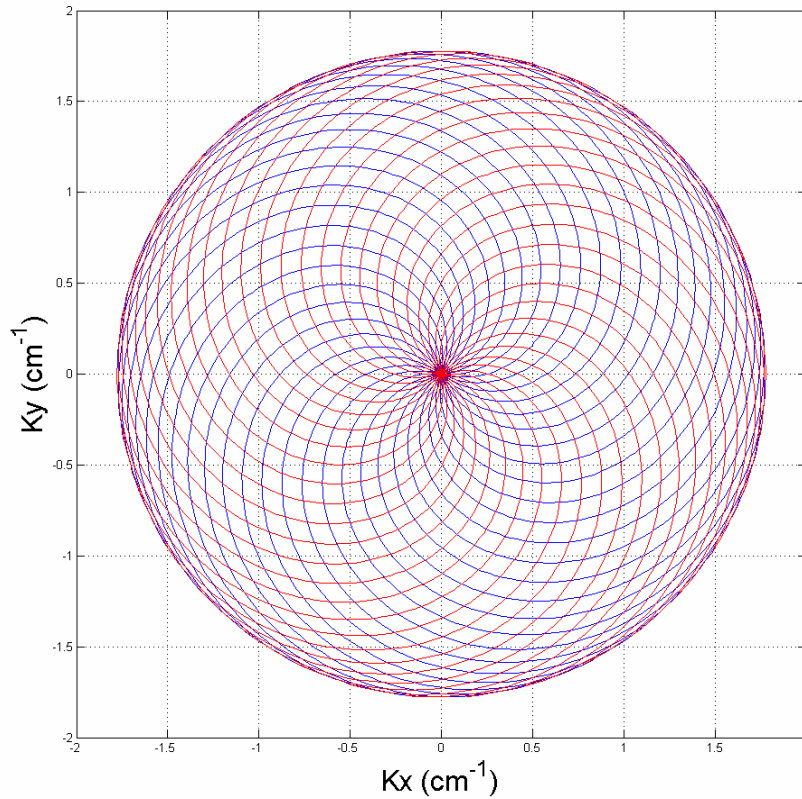
For lower spatial resolutions N_x, as can be seen in Figure 3-14 and Figure 3-15, RSI could achieve spectral bandwidths as large as a few kHz. When an acquisition with a spectral bandwidth of only a few hundred Hz may be enough to resolve all the resonances of an object, the trajectories may have a lot of twist, with ω_2 much larger than ω_1, and only a few shots N_{sh} may be needed for full K-t space coverage. However the trajectory doesn't realizes its full speed potential for sampling, because the slew rate that increases quadratic with ω_2 (equation(3.17)) is holding it back from achieving the maximum speed G_{max} allowed by the signal bandwidth/sampling rate (equation(3.42),(3.54)). There is an alternate way we can

generate the trajectories when, for a given field of view fov and spatial resolution N_x, the targeted spectral bandwidth is much smaller than the maximum achievable bandwidth $\Delta\delta_{max}(N_x)$. Further speedup in data acquisition may be obtained by allowing more than one petal from each trajectory in each temporal slice. The more petals from each trajectory are used in a temporal slice, the smaller the number of shots required to cover properly each individual temporal slice and ultimately the K-t space. An integer number of half petals n_{hptls} per each trajectory could also be used in each temporal slice, rather than using only whole petals. We are looking now for the largest n_{hptls} that can fit in the time $dT = 1/\Delta\delta$. Because each half-petal segment corresponds to a quarter of the radial oscillation period $-1/4/f_1$, we can write:

$$dT = \frac{1}{\Delta\delta} = \frac{n_{hptls}}{4 \cdot f_1} \tag{3.56}$$

$$n_{hptls} = \frac{4 \cdot f_1}{\Delta\delta} = \frac{2 \cdot \omega_1}{\pi \cdot \Delta\delta} \tag{3.57}$$

The larger ω_1, the more petals per trajectory will be used in each temporal slice, the smaller the number of excitations N_{sh} required. However ω_1 is constrained by the hardware requirements. Using the notation $[a]$ for the closest integer smaller than the real number a (e.g. $[3.72] = 3$), the slew rate, maximum scanner gradient and signal bandwidth constrains can be written as:

$$n_{hptls}^{SR} = [\frac{2 \cdot \sqrt{S_{max}^{HW} \cdot \gamma / K_{max}}}{\pi \cdot \Delta\delta}] \tag{3.58}$$

$$n_{hptls}^{grad} = [\frac{2 \cdot G_{max}^{HW} \cdot \gamma / K_{max}}{\pi \cdot \Delta\delta}] \tag{3.59}$$

$$n_{hptls}^{samp} = [\frac{4}{\pi \cdot N_x} \cdot (\frac{1}{dt \cdot \Delta\delta} - 1)] \tag{3.60}$$

$$n_{hptls} = \min(n_{hptls}^{SR}, n_{hptls}^{grad}, n_{hptls}^{samp}) \tag{3.61}$$

The result in equation(3.61) will be an integer greater or equal to two ($n_{hptls} \geq 2$), if the targeted spectral bandwidth $\Delta\delta$ is less than the maximum spectral bandwidth $\Delta\delta_{max}$ calculated for one set of trajectories (no time interleaves $n_{TI} = 1$, equation (3.39), (3.41), (3.44) and (3.45)). If $n_{hptls} = 1$, only half of a petal can be used in each temporal slice and two temporally interleaved sets of trajectories ($n_{TI} = 2$) are required to achieve the targeted spectral bandwidth $\Delta\delta$; if $n_{hptls} = 0$, more than two temporally interleaved sets are necessary.

Once n_{hptls} is determined, ω_1 and ω_2 can be calculated. From equation(3.57):

$$\omega_1 = \frac{\pi}{2} \cdot n_{hptls} \cdot \Delta\delta \tag{3.62}$$

Equations(3.51) through (3.55) will determine ω_2.

For example, for $N_x = 64$, $fov = 18cm$, $S_{max}^{HW} = 15G/cm/ms$, $dt = 8us$, the maximum achievable bandwidth with one set of trajectories is $\Delta\delta_{max} = 1231Hz$. In Table 1, the number of half petals possible per shot in each temporal slice is given for different spectral bandwidths $\Delta\delta \leq \Delta\delta_{max}$. For $\Delta\delta = 100Hz$, as many as twelve whole petals ($n_{hptls} = 24$) can be used in a temporal slice if $f_1 = 600Hz$ (equation(3.62)), instead of $f_1 = 50Hz$ (equation(3.50), $n_{TI} = 1$). In both cases, $f_2 = 621Hz$ ((3.51) through(3.55)) is limited by signal bandwidth/sampling rate. The number of excitations required for proper K-t space coverage, calculated with a simulation program as discussed in Section 3.4, is reduced from $N_{sh} = 15$ when one petal/shot is used in each temporal slice to $N_{sh} = 8$ when twelve petals/shot/temporal slice are used, effectively doubling the speed of the acquisition.

Table 1 Number of possible half petals (n_{hptls}) per shot in each temporal slice ($N_x = 64$)

$\Delta\delta(Hz)$	100	200	300	400	500	600	700	800	900
n_{hptls}	24	12	8	6	4	4	3	3	2

In Figure 3-17 (close up in Figure 3-18), the K-space coverage for one temporal slice is depicted for this alternative trajectory design method. For $\Delta\delta = 900Hz$, only one whole petal ($n_{hptls} = 2$) per shot can be used in each temporal slice.

Figure 3-17 One temporal slice K-space coverage using multiple petals per shot in each temporal slice

54
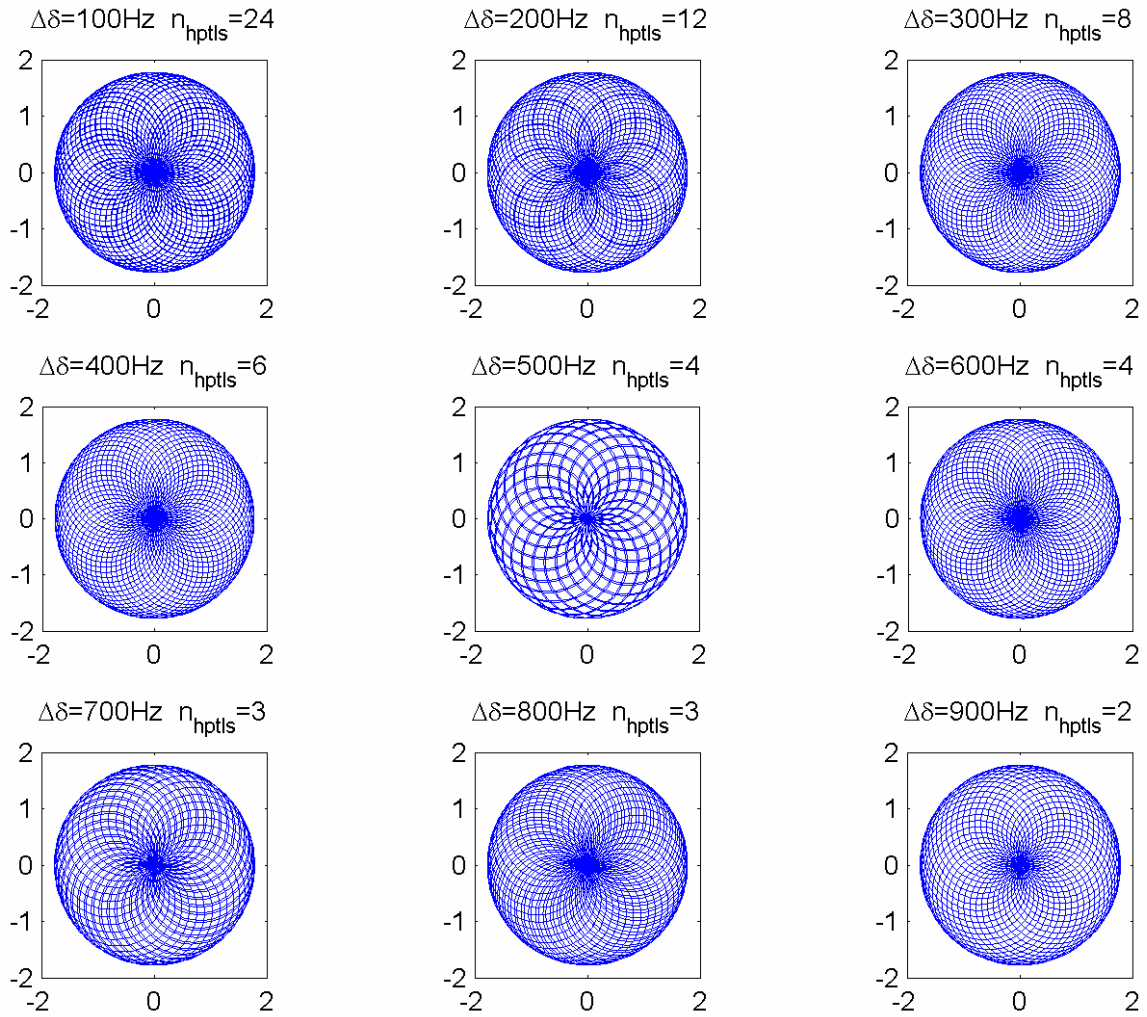
In Figure 3-18, it can be seen easier that the drawback to this alternative method to design trajectories is the increased non-uniformity in sampling, which is also illustrated in Figure 3-19, where the 2D Voronoi weights for samples in one temporal slice at $\Delta\delta = 200Hz$, $n_{hptls} = 12$, were calculated as described in Section 3.5.

Figure 3-18 Increased non-uniform sampling for more than one petal/shot/temporal slice
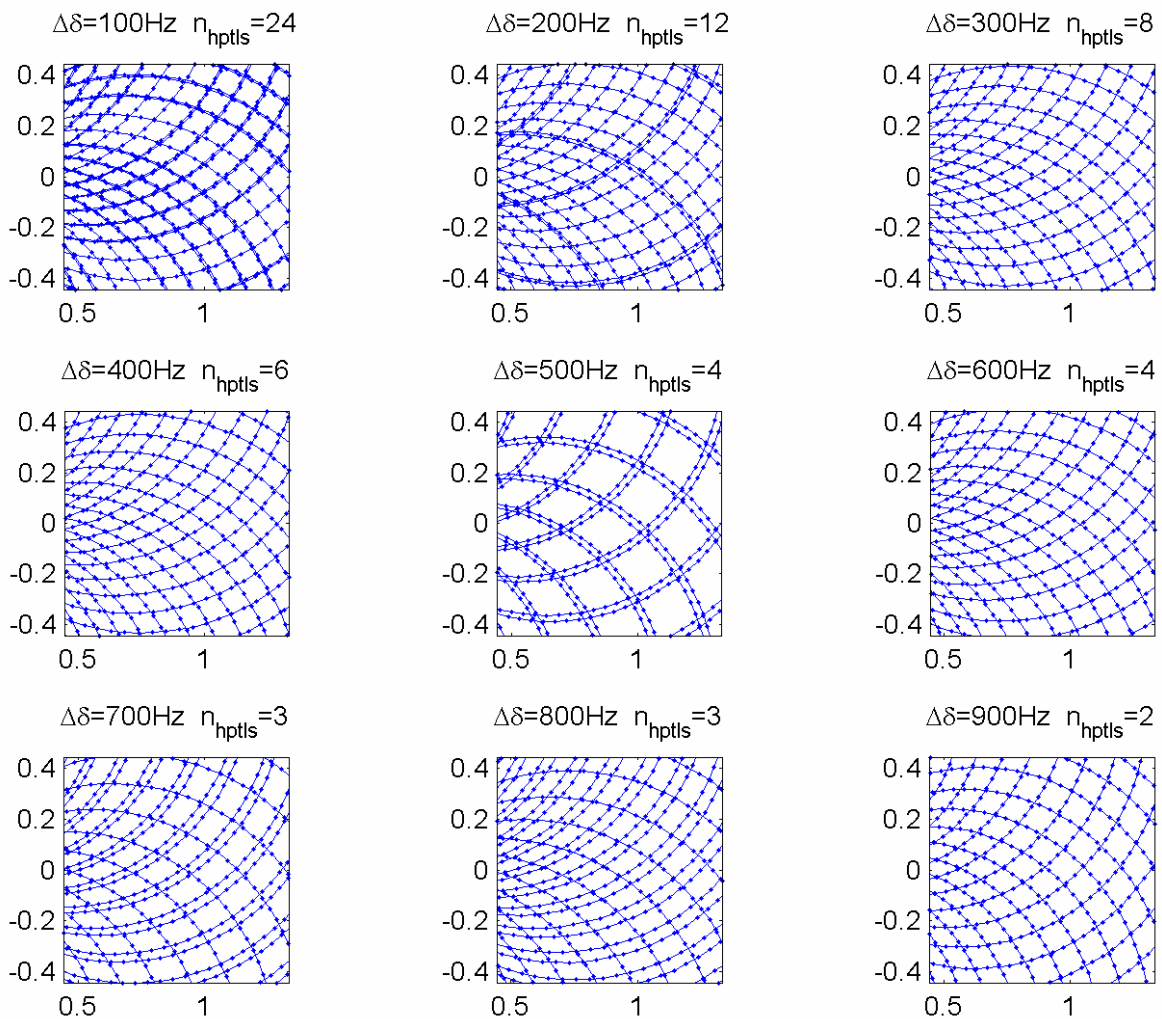
Figure 3-19 2D Voronoi weights for one temporal slice when $n_{hptls} = 12$ (six whole petals/shot/slice)
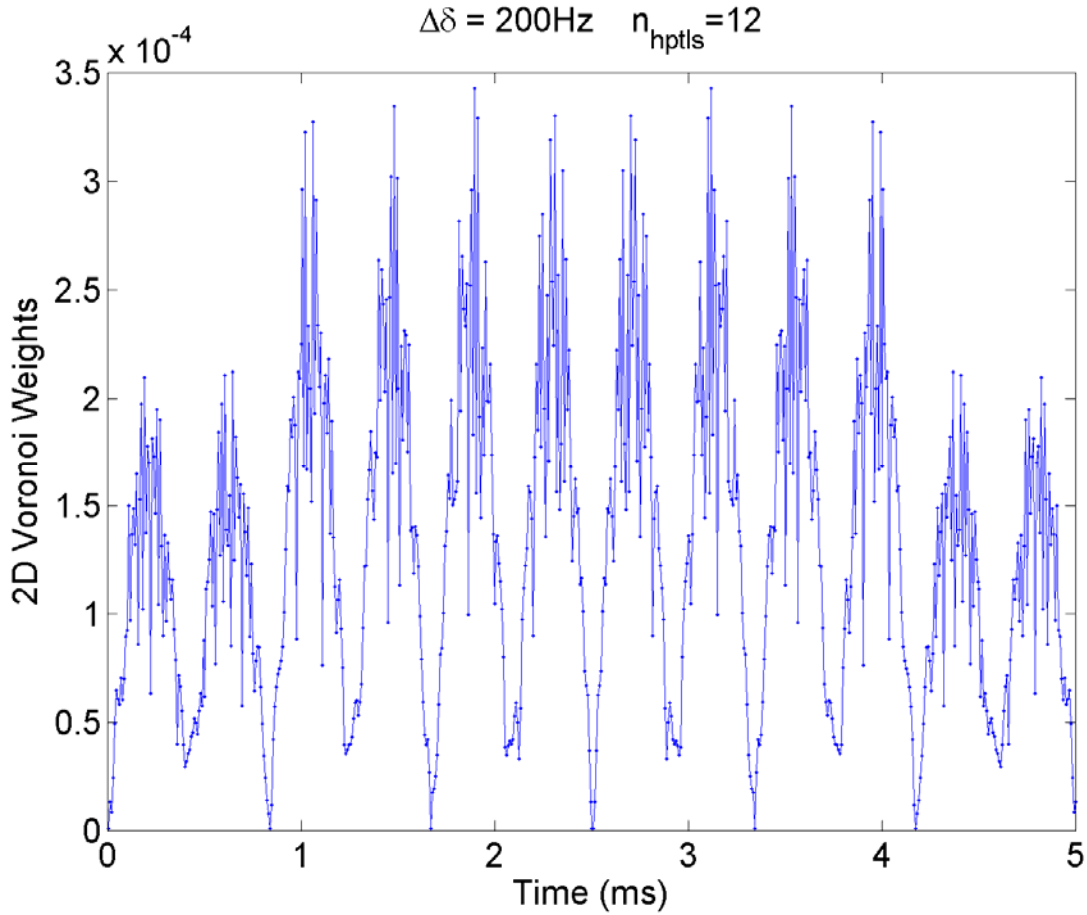
In general, when designing trajectories that include more than one petal per shot in each temporal slice, instead of choosing the largest value for ω_2, more uniform sampling can be achieved by selecting an adequate value for ω_2 / ω_1 and the number of excitations used N_{sh}. Rather than choosing the largest ω_2 allowed by hardware/sampling requirements as done above (equation(3.51) through(3.55)), ω_2 can be chosen based on each individual situation. For example, when $n_{hptls} = 6$ (three petals/shot/temporal slice), we could select $\omega_2 = \omega_1 / 3$ and a number of excitations N_{sh} that is not divisible by three (e.g. 7, 8, 10, 11, etc...). If $n_{hptls} = 7$, we can choose to use only three petals/shot/slice, setting $n_{hptls} = 6$, followed by setting $\omega_2 = \omega_1 / 3$,

and so on. This way, while preserving the benefit of faster data acquisition through using more than one petal per shot in each temporal slice, we are not giving up entirely on sampling uniformity.

When implementing the gradient waveforms on the scanner, because the theoretical gradients do not start at zero at $t = 0$, $K = 0$ (equation(3.5), (3.13)), a warping function $\eta(t)$ is used to ramp up the gradients. The gradient waveforms will evaluate in time as $G_{x,y}(\eta(t))$ (Figure 3-20) instead of as $G_{x,y}(t)$ (Figure 3-3), where:

$$
\eta(t) =
\begin{cases}
\dfrac{t^2}{2 \cdot t_c}, & 0 \le t < t_c \\[4mm]
t - \dfrac{t_c}{2}, & t_c \le t \le T_{AQ}
\end{cases}
\qquad
t_c = \dfrac{2 \cdot G_{max}}{S_{max}^{HW}}
\qquad\qquad (3.63)
$$

G_{max} is the maximum gradient along the trajectory and is given by equation(3.8).

When the trajectory ends at $K = 0$, the gradient has a non-zero value. To avoid hanging the scanner, the gradients (x and y) are independently decreased to zero at a slew rate smaller than $S_{max}^{HW} / 2$, while at the same time rewinding the trajectory back to $K = 0$, to avoid leaving an accumulated phase/magnetization in K-space. This is necessary especially when short repetition times are used. Spoiler gradients (very large gradients played for a few milliseconds at the end of the sequence, after each excitation and collection of data), can also be applied to dephase the residual transverse magnetization. We employ both, trajectory rewinding to $K = 0$ (concomitant with bringing the gradients to zero), followed by spoiler gradients.

Figure 3-20 Gradient Ramp Up using a warping function $\eta(t)$
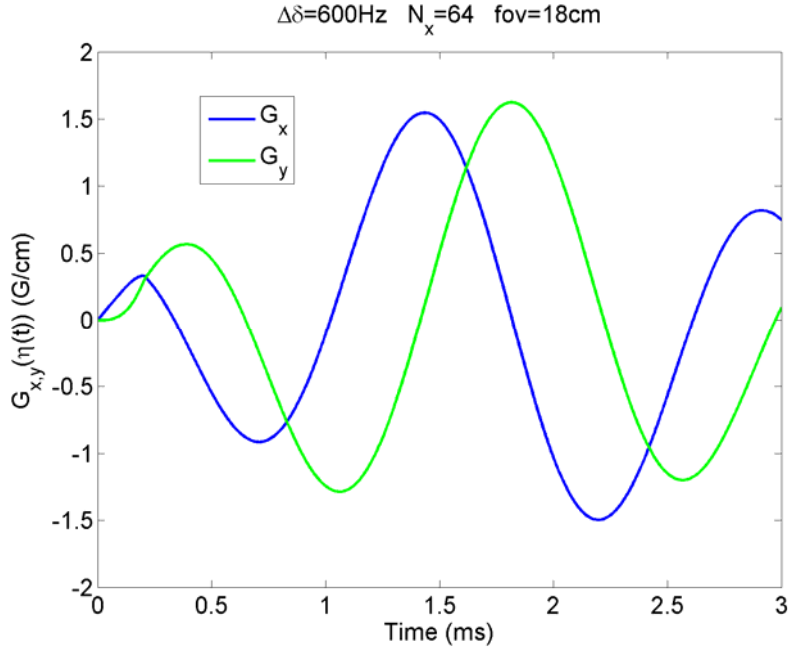
3.4 RSI: NUMBER OF EXCITATIONS

The previous section 3.3 addressed the problem of achieving properly sampled K-t space along the time axis and choosing all the rosette trajectory parameters ($K_{max}, \omega_1, \omega_2$). In this section, we will concern ourselves with properly sampling K-space in each temporal slice and therefore with choosing the number of excitations N_{sh} required to achieve this. Based on the way the temporal slices are selected (namely, they are delimited by successive $K = 0$ crossings), because of the periodicity of the trajectory, if one temporal slice is properly sampled, all temporal slices will be properly sampled.

To determine the minimum number of excitations N_{sh} required for proper coverage of K-space in each temporal slice, we employ a simulation program that generates N_{sh} trajectories

with $2\pi / N_{sh}$ angular separation between each other, to obtain uniform angular distribution. The trajectories are generated with parameters K_{max}, ω_1 and ω_2 calculated as described in the previous section 3.3, discretely sampled every dt seconds. Because of the discrete sampling, except for the start of the trajectory corresponding to $K = 0$, the closest points in distance to $K = 0$ are identified and used for defining the temporal slices. In each temporal slice, for all the samples on one trajectory, the K-space distance (in x and y) to all the points on the other $N_{sh} - 1$ trajectories is measured. The smallest of these distances is verified against the inverse of the field of view as required by the Nyquist Criterion to avoid aliasing $dK \leq 1 / fov$. (Note that along each trajectory, Nyquist is already observed when designing the trajectory, equation(3.42)). The number of excitations N_{sh} is increased until $dK \leq 1 / fov$ in all temporal slices. At this point, the program stops, as this is the minimum number of excitations required for proper K-t space coverage as defined by the Nyquist Criterion.

While, for fastest possible coverage of K-t space, the number of excitations will be determined through direct measurement of the distance between the samples, by the above simulation program, it is desirable we could use a number of excitations N_{sh} that can be estimated analytically based on the scanning parameters, even if it is an approximation. The following calculations are intended to determine the number N_{sh} that provides proper K-space coverage for an individual temporal slice and therefore, proper coverage for K-t space. The derivation is based on using two temporarily interleaved sets of trajectories with half a petal/shot/temporal slice. The same arguments are applicable to one set of trajectories, with one

59

petal per shot in each temporal slice. Note: For two sets of trajectories ($n_{TI} = 2$), the total number of excitations required is $N^{RSI} = 2 \cdot N_{sh}$.

The number of times one outgoing/incoming shot will intersect the incoming/outgoing shots inside a temporal slice is (round down to the closest integer):

$$N_{cross} = N_{sh} \cdot \omega_2 / (2 \cdot \omega_1) \tag{3.64}$$

The crossing points are arranged on N_{cross} concentric circles. On each circle, there are N_{sh} crossings of two trajectories and the angular separation between these crossings is $2 \cdot \pi / N_{sh}$. The crossings on the odd numbered circles are aligned along radial lines (angular separation between these lines $2 \cdot \pi / N_{sh}$). Crossings on the even numbered circles are also aligned along radial lines $2 \cdot \pi / N_{sh}$ apart and shifted by π / N_{sh} with respect to the radial lines on which the odd number circles' crossings reside.

The distance to the center of K-space ($K = 0$) for the crossing points is:

$$K_r^{(n)} = K_{max} \cdot \sin(\frac{\pi}{2} - \frac{\omega_1}{\omega_2} \cdot \frac{\Delta\beta_0}{2} - \frac{\omega_1}{\omega_2} \cdot \frac{\pi}{N_{sh}} \cdot (n-1)) \tag{3.65}$$

$n = 1, 2 ... N_{cross}$ is the circle on which the crossings reside, $n = 1$ being the circle closest to the edge of K-space ($K - > K_{max}$) and $n = N_{cross}$ being the circle closest to the center of K-space ($K - > 0$). For one set of trajectories $\Delta\beta_0 = 0$ and the circle with $n = 1$ corresponds exactly to $K = K_{max}$ where the outgoing trajectory begins returning to $K = 0$, thus becoming an incoming trajectory; for two sets of trajectories $\Delta\beta_0$ ($0 \le \Delta\beta_0 < 2 \cdot \pi / N_{sh}$) is the angular separation measured at $K = K_{max}$, between two trajectories that cross on the circle with $n = 1$ (the most outward).

Equation (3.65) was derived as follows:

The angular separation as measured at $K = K_{max}$ between trajectories those cross on circle n is:

$$\Delta\beta = \Delta\beta_0 + \frac{2 \cdot \pi}{N_{sh}} \cdot (n-1) \tag{3.66}$$

The total angle swapped by a trajectory from $K = 0$ to $K = K_{max}$ during one quarter of radial oscillation period $T_1 = 1/f_1$:

$$\Delta\varphi = \omega_2 \cdot \frac{T_1}{4} = \frac{\pi\omega_2}{2\omega_1} \tag{3.67}$$

The angle swapped by the trajectory from $K = 0$ to $K = K_r^{(n)}$ is:

$$\omega_2 \cdot t^{(n)} = \Delta\varphi - \frac{1}{2}\Delta\beta \tag{3.68}$$

Therefore,

$$t^{(n)} = \frac{\pi}{2\omega_1} - \frac{\Delta\beta_0}{2\omega_2} - \frac{1}{\omega_2} \cdot \frac{\pi}{N_{sh}} \cdot (n-1) \tag{3.69}$$

To obtain (3.65) plug $t^{(n)}$ in:

$$K_r^{(n)} = K_{max} \cdot \sin(\omega_1 \cdot t^{(n)}) \tag{3.70}$$

The distance between two adjacent trajectories is approximated as:

$$d(C_1, C_2) = \max(\min(d_1, d_2, d_3)) \tag{3.71}$$

d_1, d_2, d_3 are defined as in Figure 3-21

Figure 3-21 Definition of distances d_1, d_2, d_3 between two adjacent trajectories
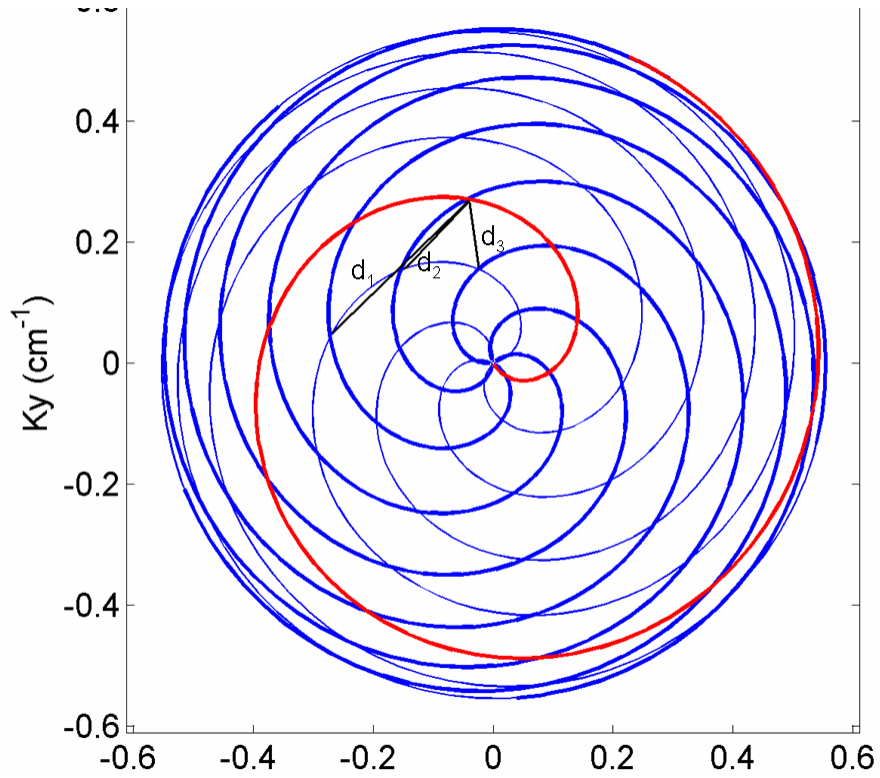
Figure 3-22 Definition of distances d_1, d_2, d_3 (close up)
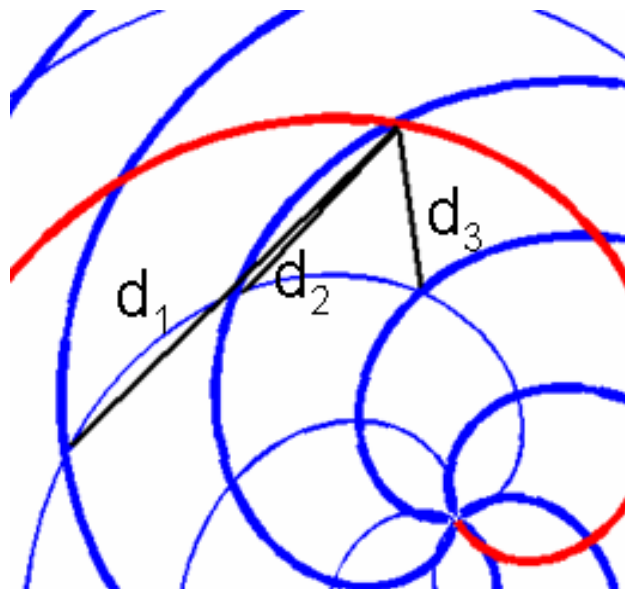
The distance d_1 between two crossings at same radial distance from the center of K-space, situated on a circle of radius $K = K_r^{(n)}$ is approximated to be equal to the length of the circular arc connecting them:

$$d_1 = \frac{2\pi}{N_{sh}} \cdot K \qquad (3.72)$$

The distance d_2 between two crossings sitting on consecutive circles on adjacent trajectories is the hypotenuse for the triangle with one side along the radial direction ΔK_r and the other side tangential to the circle ΔK_θ :

$$\Delta K_r^{(n,n+1)} \cong \frac{\Delta K_r^{(n,n+2)}}{2} = \frac{\pi \omega_1}{\omega_2 N_{sh}} \sqrt{K_{max}^2 - K^2} \qquad (3.73)$$

$$\Delta K_\theta = \frac{\pi}{N_{sh}} \cdot K \qquad (3.74)$$

$$d_2 = \sqrt{\Delta K_r^2 + \Delta K_\theta^2} = \frac{\pi \omega_1}{\omega_2 N_{sh}} \cdot \sqrt{K_{max}^2 - (1 - \frac{\omega_2^2}{\omega_1^2}) \cdot K^2} \qquad (3.75)$$

The distance d_3 between crossings sitting on circles $n, n+2$ on the same radial axis is:

$$d_3 = \Delta K_r^{(n,n+2)} = K_r^{(n)} - K_r^{(n+2)} = 2K_{max} \sin(\frac{\pi \omega_1}{\omega_2 N_{sh}}) \cdot \cos(\frac{\pi}{2} - \frac{\Delta \beta_0}{2} \cdot \frac{\omega_1}{\omega_2} - \frac{\pi}{N_{sh}} \cdot \frac{\omega_1}{\omega_2} \cdot n) \ (3.76)$$

From equation(3.65), we can write:

$$\cos(\frac{\pi}{2} - \frac{\Delta \beta_0}{2} \cdot \frac{\omega_1}{\omega_2} - \frac{\pi}{N_{sh}} \cdot \frac{\omega_1}{\omega_2} \cdot n) = \sqrt{1 - (\frac{K_r^{(n+1)}}{K_{max}})^2} \qquad (3.77)$$

$$d_3 \cong \frac{2\pi \omega_1}{\omega_2 N_{sh}} \cdot \sqrt{K_{max}^2 - K^2} \qquad (3.78)$$

Comparing directly d_1, d_2 and d_3 yields $\min(d_1, d_2, d_3)$ equal to

$$\min(d_1, d_2, d_3) = \begin{cases} d_1 & \text{in Reg. 1} & 0 \leq K \leq \dfrac{K_{\max}}{\sqrt{1 + \dfrac{3 \cdot \omega_2^2}{\omega_1^2}}} = K_1 \\[3em] d_2 & \text{in Reg. 2} & K_1 = \dfrac{K_{\max}}{\sqrt{1 + \dfrac{3 \cdot \omega_2^2}{\omega_1^2}}} \leq K \leq \dfrac{K_{\max}}{\sqrt{1 + \dfrac{\omega_2^2}{3 \cdot \omega_1^2}}} = K_2 \\[3em] d_3 & \text{in Reg. 3} & K_3 = \dfrac{K_{\max}}{\sqrt{1 + \dfrac{\omega_2^2}{3 \cdot \omega_1^2}}} \leq K \leq K_{\max} \end{cases}$$

$$d(C_1, C_2) = \max(d_1(\operatorname{Re} g1), d_2(\operatorname{Re} g2), d_3(\operatorname{Re} g3)) \tag{3.79}$$

For $\omega_2 / \omega_1 \leq 1$

$$d(C_1, C_2) = \max(d_1(K_1), d_2(K_1), d_3(K_3)) \tag{3.80}$$

$$d(C_1, C_2) = \frac{2\pi K_{\max}}{N_{sh}} \cdot \max\left(\frac{1}{\sqrt{1 + \dfrac{3\omega_2^2}{\omega_1^2}}}, \frac{1}{\sqrt{1 + \dfrac{3\omega_2^2}{\omega_1^2}}}, \frac{1}{\sqrt{3 + \dfrac{\omega_2^2}{\omega_1^2}}}\right) \tag{3.81}$$

$$d(C_1, C_2) = \frac{2\pi K_{\max}}{N_{sh}} \cdot \frac{1}{\sqrt{1 + \dfrac{3\omega_2^2}{\omega_1^2}}} \tag{3.82}$$

$$N_{sh}(\frac{\omega_2}{\omega_1} \leq 1) = \frac{\pi \cdot N_x}{\sqrt{1 + \frac{3\omega_2^2}{\omega_1^2}}} \tag{3.83}$$

For $\omega_2 / \omega_1 > 1$

$$d(C_1, C_2) = \max(d_1(K_1), d_2(K_2), d_3(K_3)) \tag{3.84}$$

$$d(C_1, C_2) = \frac{2\pi K_{max}}{N_{sh}} \cdot \max(\frac{1}{\sqrt{1 + \frac{3\omega_2^2}{\omega_1^2}}}, \frac{1}{\sqrt{3 + \frac{\omega_2^2}{\omega_1^2}}}, \frac{1}{\sqrt{3 + \frac{\omega_2^2}{\omega_1^2}}}) \tag{3.85}$$

$$d(C_1, C_2) = \frac{2\pi K_{max}}{N_{sh}} \cdot \frac{1}{\sqrt{3 + \frac{\omega_2^2}{\omega_1^2}}} \tag{3.86}$$

$$N_{sh}(\frac{\omega_2}{\omega_1} > 1) = \frac{\pi \cdot N_x}{\sqrt{3 + \frac{\omega_2^2}{\omega_1^2}}} \tag{3.87}$$

Nyquist: $dK = d(C_1, C_2)$ and $dK \leq dK_{Nq} = N_x / 2 / fov$

The estimated number of excitations required (equations(3.83), (3.87)) is lower than the number required for a projection imaging acquisition ($N_{PI} = \pi N_x$) and decreases as the trajectory twist (ω_2 / ω_1 ratio) increases. Moreover, they represent an overestimate, because the true distance between C_1, C_2, is smaller than any of the three segments d_1, d_2, d_3 for which approximations also have been made. Segment d_1, for example, is approximated to be equal to the length of the circular arc rather than the straight line connecting the points. We have found, the estimated number of excitations given be equation(3.83) or equation (3.87), can be between

10-15% to around a factor of two larger than the minimum number N_{sh} required for proper K-t space coverage, calculated through direct measurement using the program we described at the beginning of this section. In fact, because of the way the requirement for proper sampling was imposed in the N_{sh} theoretical derivation (the largest K-space separation between adjacent trajectories $d(C_1, C_2)$ obeys Nyquist), this is equivalent to requiring the outgoing trajectories be enough to properly sample one temporal slice. Because the calculations for two adjacent incoming trajectories would be the same as the ones that were presented above, this also means the incoming trajectories alone properly sample the temporal slice and are sufficient to produce an image at the spatial resolution targeted N_x.

We decided to investigate how the number of excitations N_{sh} affects the sampling uniformity η (see also Appendix):

$$\eta = \frac{\sum\limits_{i=1}^{N} w_i}{\sqrt{N \cdot \sum\limits_{i=1}^{N} w_i^2}} \leq 1 \tag{3.88}$$

For a fixed spatial resolution $N_x = 64$ ($fov = 18cm$) and fixed spectral bandwidth $\Delta\delta = 1200Hz$, and trajectory twist $\omega_2 / \omega_1 = .9737$, we calculated with the simulation program the minimum number of excitations for proper K-t space coverage to be $N_{sh}^{\min} = 56$ shots. The theoretical number of excitations required is (equation(3.83), rounded to the closest integer): $N_{sh}^{est} = 103$ shots. Keeping everything else the same, we increment in steps of one the number of excitation N_{sh} (angular separation between trajectories is $2\pi / N_{sh}$), measure the 2D Voronoi weights w_i in each temporal slice, as described in Step 1D in section 3.5, and calculate η in equation (3.88) in each of the $N_\delta = 74$ temporal slices. The number of excitations is increased

from N_{sh}^{min} to $1.1 \cdot N_{sh}^{est}$. The results are compared to the theoretical sampling efficiency based on

$$w_i = dA_i \sim K_r^{(i)} \sqrt{K_{max}^2 - (K_r^{(i)})^2}$$ (equation(3.93)) and displayed in Figure 3-23. As shown in the

Appendix, the theoretical sampling efficiency based on these weights is $\eta^{est} = 2\sqrt{2}/\pi \simeq .90$ (blue

crosses). The length of the error bars is equal to the standard deviation for η in all

$N_\delta = 74$ temporal slices. While η calculated over all the sampled points closely matches the

curve displayed in Figure 3-23, we chose to display η as an average (with error bars) of the

sampling efficiencies calculated in each slice because, as seen in Figure 3-24 and Figure 3-25,

the 2D Voronoi weights do not match the 3D Voronoi weights for lower N_{sh}.

Figure 3-23 Sampling Efficiency η as a function of number of shots N_{sh} used
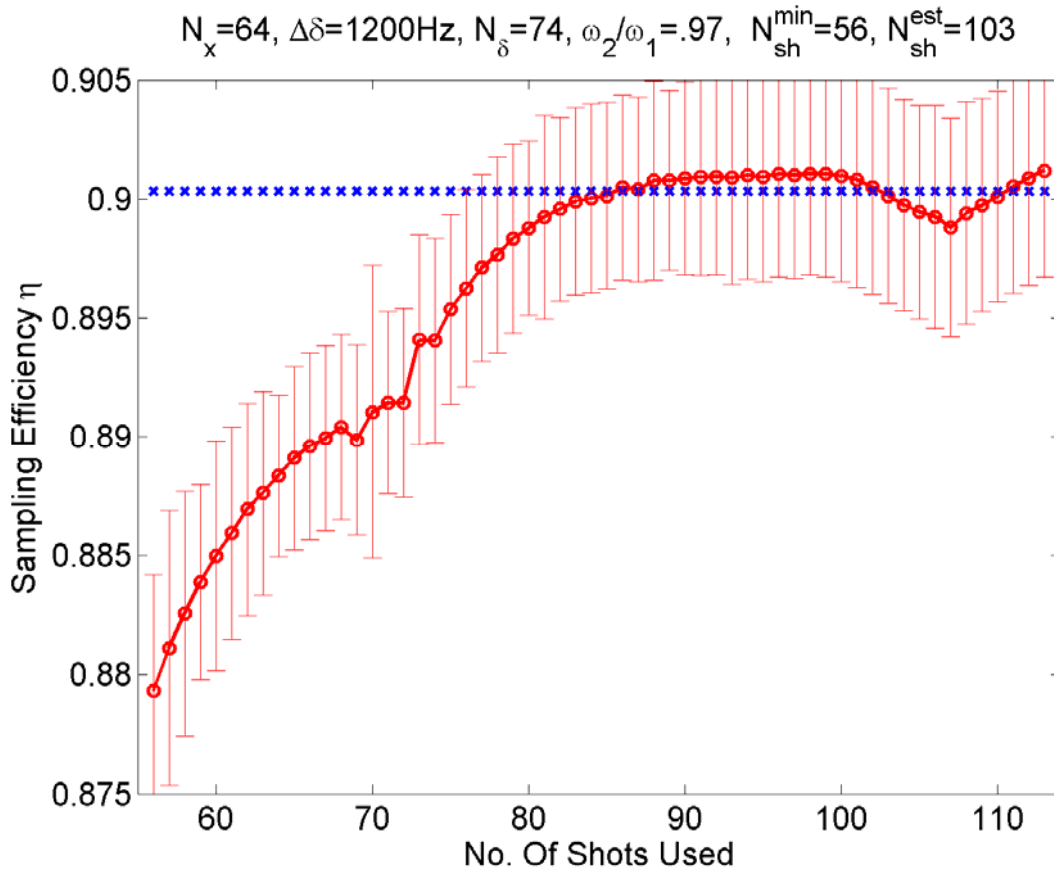
The sampling efficiency goes asymptotically to the the theoretical estimated value η^{est} as N_{sh} increases. It reaches this value around $N_{sh} = 85$ suggesting the number estimated by equation(3.82), $N_{sh}^{est} = 103$ shots is a ~20% overestimate.

Figure 3-24 $N_{sh}^{min} = 56$ **Weights: Analytical (blue) and 2D (green) and 3D (red) Voronoi**
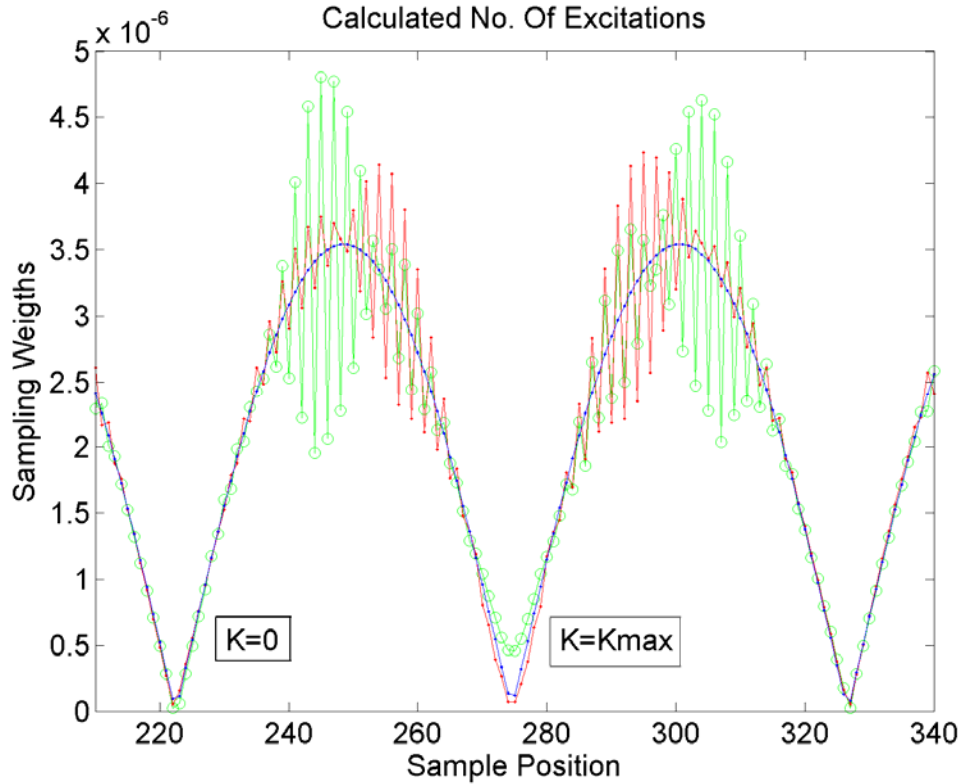
At $N_{sh} = N_{sh}^{est}$ (Figure 3-25), the 2D Voronoi weights calculated in each temporal slice are the same as the 3D Voronoi volumes and they are equal to the weights estimated analytically $w_i = dA_i$ (equation(3.93)). This is very beneficial in the reconstruction process as discussed in data reconstruction section 3.5.

Figure 3-25 $N_{sh}^{est} = 103$ **Weights: Analytical (blue) and 2D (green) and 3D (red) Voronoi**
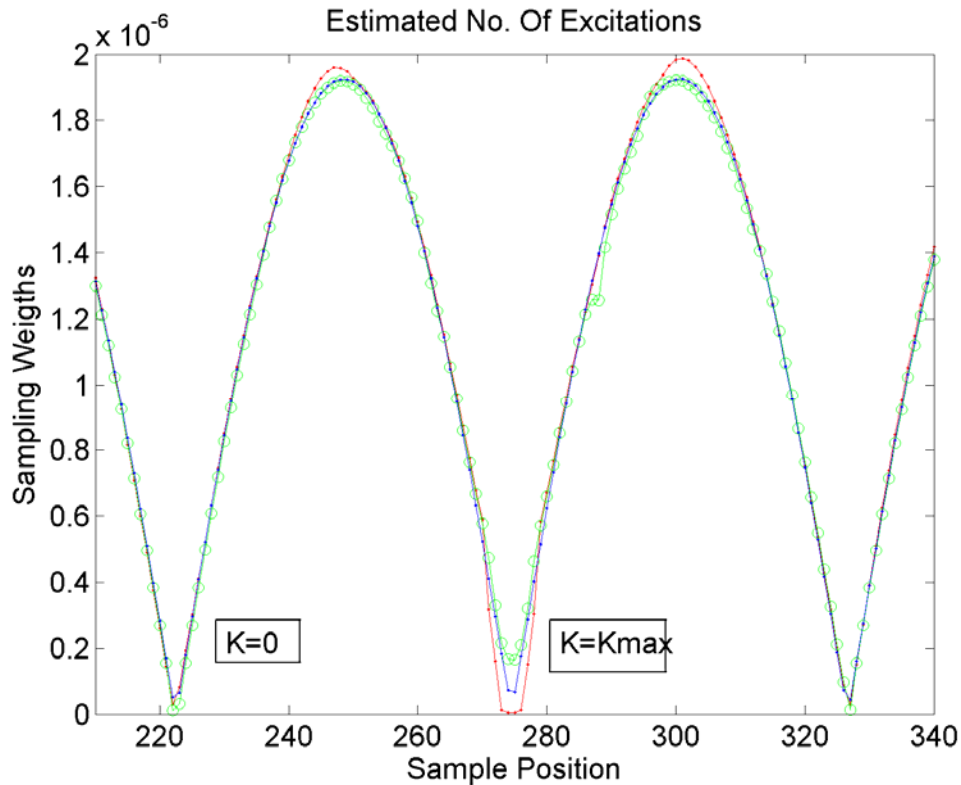
3.5   DATA RECONSTRUCTION

3.5.1   Data reconstruction

Reconstruction of data not falling on a Cartesian grid has been extensively investigated and described in the scientific literature. This is a Fourier inversion problem, usually solved using convolution interpolation, a process also known as gridding. An overview of the main issues (and typical solutions) involved with reconstructing non-Cartesian MRI data can be found in John Pauly's 2005 notes at: http://www.stanford.edu/class/ee369c/notes/non_cart_recon.pdf.

Because this is an external link subject to change, where appropriate, references will be provided. In this section, we will only present how we implemented the reconstruction and give some examples relevant to this work.

The data reconstruction process for an RSI acquisition involves the following steps:

1) Precompensation of K-t space data

2) Filtering

3) Convolution Gridding

4) Post Compensation

5) Zero Padding and Fourier Transform

6) Apodization -> Image

Step 1) Precompensation

Good treatments of the density compensation ($\rho_i = 1/w_i$, w_i-precompensation weights) are given in [49] and [51]. After density precompensation, the K-space energy should be flat [31]. We have tried the following precompensation weights:

A) A ramp filter as used in projection imaging reconstruction and used by Noll [37] was first considered. This is a geometrical factor accounting for the fact data is sampled on a disk (cylinder in K-t space), and there is more data samples at the center of K-space ($K = 0$) than at the edge $K = K_{max}$.

$$w_i = K_r^{(i)} \tag{3.89}$$

B) Better results are obtained when in addition to the geometrical factor the speed of the trajectory ($|\vec{G}|$, equation(3.7)) is taken into account. When the trajectory moves faster through

K-space, the distance between data samples increases and the sampling density decreases, thus larger weights need to be assigned to those samples; the corresponding weights are:

$$w_i = K_r^{(i)} \cdot |\vec{G}^{(i)}| = K_r^{(i)} \cdot \frac{K_{max} \cdot \omega_1}{\nmid} \cdot \sqrt{1 - (1 - \frac{\omega_2^2}{\omega_1^2}) \cdot \frac{(K_r^{(i)})^2}{K_{max}^2}} \qquad (3.90)$$

However, for increased amounts of trajectory twist (approx. above $\omega_2 / \omega_1 > 3$), the product between the geometrical factor ($K_r^{(i)}$) and the speed of the trajectory ($|\vec{G}^{(i)}|$) assigns incorrectly too much weight to the high spatial frequency samples (closer to K_{max}) which can result in inaccurate reconstruction.

C) The theoretical area associated with each data sample in K-space

$$w_i = dA_i = dK_r^{(i)} \cdot dK_g^{(i)} = (\nmid \cdot G_r^{(i)} \cdot dt) \cdot (\nmid \cdot G_g^{(i)} \cdot dt) \qquad (3.91)$$

Using equations (3.11),(3.12) and (3.2) we can rewrite(3.91) as:

$$w_i = K_{max}^2 \cdot dt^2 \cdot \omega_1 \cdot \omega_2 \cdot \sin(\omega_1 t^{(i)}) \cdot \cos(\omega_1 t^{(i)}) = \omega_1 \cdot \omega_2 \cdot dt^2 \cdot K_r^{(i)} \cdot \sqrt{K_{max}^2 - (K_r^{(i)})^2} \quad (3.92)$$

Discarding the constant factor $\omega_1 \cdot \omega_2 \cdot dt^2$:

$$w_i = K_r^{(i)} \cdot \sqrt{K_{max}^2 - (K_r^{(i)})^2} \qquad (3.93)$$

The result in equation(3.93) performs best when used in conjunction with the theoretical number of excitations derived in section 3.4 (equation(3.83),(3.87)).

D) In each temporal slice, we measure the area associated with each data sample [51] using the Matlab functions *voronoin* and *convhulln*. The median lines between each neighboring pair of points form polygons for which area is calculated. The relevant part of the program is listed below (kx, ky represent the position vectors for all data points in one temporal slice):

```
[vv,vc]=voronoin([kx ky]);
for i = 1:length(kx)
    if all(vc{i}~=1)
        [ktemp, va(i)] = convhulln(vv(vc{i}, :));
    end
end
```

Data points very close in position, as the ones very close to the center of K-space ($K = 0$) or where the trajectories cross each other, could pose a problem and result in an error message generated by the Matlab program. If N_{pts} are found within a distance $< \Delta k / 10$ ($\Delta k = 1 / fov$), we replace them with one point. After the Voronoi calculation, the area calculated for the problematic point is equally divided between the original N_{pts}, which are reinstated in the data set. In addition, at the edge of K-space ($K = K_{max}$), the median lines between sampled points could converge very far away ($K \gg K_{max}$), resulting in polygons with large areas that would inaccurately describe the weight of those points. We temporarily add 512 data samples on a circle at $K = 1.01 \cdot K_{max}$, calculate the areas for all data points and then remove these temporary points. The sampling density ($\rho_i = 1 / w_i$) and the sampling density profile for one temporal slice are shown in Figure 3-26.

Figure 3-26 Sampling density in one temporal slice (2D Voronoi)
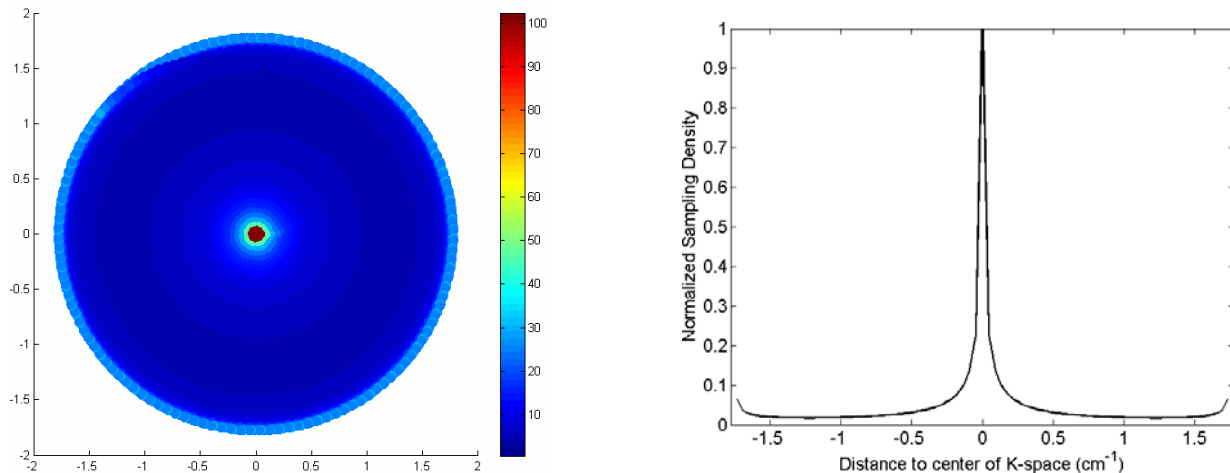
The reasoning behind using 2D Voronoi weights calculated as described above, or using the weights given by equations(3.89), (3.90) or (3.93) in a 3D reconstruction where the volume associated with the data samples would be more appropriate, is found analyzing Figure 3-8. Regardless of the position in K-space, the time axes (the two vertical red lines positioned at arbitrary distances from $K = 0$) are sampled twice in each temporal slice. The length of the time segment associated with each of these two points is equal to half the thickness of a temporal slice $dT/2$ and is the same for all data points. The 3D volume in K-t space is equal to the area associated with the data point in K-space multiplied by the height $dT/2$.

Step 2) Filtering

When comparing the SNR performance of RSI *vs.* CSI in section 3.7, no filters are applied. However, especially for objects with sharp edges, to eliminate the Gibbs ringing associated with the way the Fourier Transform behaves at a discontinuity jump, filtering the data may be indicated. While this step may be applied after the convolution gridding and before the inverse FT, we obtained reconstructions that are more accurate if we filtered the data before gridding. When filtering is applied, we use the following spatial and temporal Hanning filters:

$$F_{x,y} = (1 + \cos(\pi \cdot \frac{K_r}{K_{max}}))/2 \tag{3.94}$$

$$F_t = (1 + \cos(\pi \cdot \frac{t}{T_{read}}))/2 \tag{3.95}$$

These low pass filters attenuate the high spatial/spectral frequencies. Some loss in details is to be expected. In general, low-pass filters have the effect of decreasing the effective resolution in the final image accompanied by an increase in SNR.

Step 3) Convolution Gridding

73

Data is convoluted on a two-fold oversampled grid in each dimension (x, y, t) with a Kaiser-Bessel kernel [21]:

$$C(u) = \frac{1}{W} \cdot I_o[B \cdot \sqrt{1 - (2u/W)^2}] \tag{3.96}$$

I_0 is the modified Bessel function of the first kind of order zero. $|u| \le W/2$ is the distance in K-space between the sampled position (k_α) and position on the grid (k_p): $u_x = k_{x,\alpha} - k_{x,p}$. W is the kernel width. $C(|u| > W/2) = 0$. B is a parameter calculated to minimize the relative amount of aliasing energy; the values calculated by Jackson *et al.* [21] for a two-fold oversampled grid and used by us are:

Table 2 Kaiser-Bessel kernel parameters for a two-fold oversampled grid

W	1.5	2.0	2.5	3.0	3.5	4.0
B	6.6875	9.1375	11.5250	13.9086	16.2734	18.5547

Larger kernel windows produce results that are more accurate but require longer computation times. Typical values used by us in reconstruction are $W_x = W_y = 3.5$ and $W_t = 2.5$. We presample the kernel in 2048 points between zero and $I_0(B)/W$ and use nearest neighbor interpolation to determine $C(u)$ for each sample position/grid position. This reduces computation time by approx. 5-10 times compared to calculating the kernel every time.

Before actual 3D gridding of the data points, for each sampled position α, the sum of the gridding kernels is calculated

$$S_\alpha = \sum_p \sum_q \sum_m C(u_{\alpha p}) \cdot C(v_{\alpha q}) \cdot C(t_{\alpha m}) \tag{3.97}$$

The data points are gridded on the 3D grid using a normalized kernel $C(u_{\alpha p}) \cdot C(v_{\alpha q}) \cdot C(t_{\alpha m}) / S_{\alpha}$. This ensures no additional weighting is introduced by the gridding process.

Step 4) Post Compensation

When the precompensation weights are not accurate, one way to correct for it is to use post-compensation. The precompensation weights are gridded in parallel with the precompensated data. At the end of the gridding process, the gridded data matrix is divided to the matrix on which the precompensated weights alone were gridded. In principle, the postcompensation process should work even without precompensation if the density of the trajectory does not change significantly over a region of K-space the size of the convolution kernel [31]. In section 3.7, when comparing the SNR performance of RSI *vs.* CSI, no post compensation is used.

Step 5) Zero Padding and Fourier Transform

Besides filtering, smoother images can be obtained using zero padding, which is similar to a digital zoom. For images with a spatial resolution $N_x < 128$, we use a zero filling factor $zN_x = zN_y = 128 / N_x$, and for the spectral response function using the 3D reconstruction and evaluation method in section 3.2, we use a zero filling factor along the time axis $zN_2 = 128 / N_{\delta}$. An inverse Fourier transform (IFT) along each direction (preceded and followed by *ifftshift* in Matlab), generates the reconstructed image.

Step 6) Apodiziation

Because data was reconstructed on a two-fold oversampled grid, if the image size after IFT is $2N \cdot 2N \cdot 2M$, the central image $(-N/2, N/2; -N/2, N/2; -M/2, M/2)$ is subtracted and used further. Because of the convolution gridding, the reconstructed data needs to be

75

apodized by dividing to $c(x) \cdot c(y) \cdot c(f)$, where $c(x)$ is the IFT of the gridding kernel in equation(3.96):

$$c(x) = \frac{\sin \sqrt{\pi^2 W^2 x^2 - B^2}}{\sqrt{\pi^2 W^2 x^2 - B^2}} \qquad (3.98)$$

The parameters W, B are the same as the ones used in equation(3.96), and can be found in Table 2.

The effect of some of the reconstruction operations described is illustrated in the next figures. The same object used in section 3.2 (Figure 3-4) and a trajectory length $N_\delta = 36$ are used. When no precompensation ($w_i = 1$) or postcompensation is performed, the reconstructed object in the on-resonance slice looks like the one in Figure 3-27, with a y-axis profile through $K = 0$ shown in Figure 3-28 (blue line). The spectral response (section 3.2) through the region of interest (Figure 3-29 blue line) shows a lot of leakage in the off-resonance slices. Post compensation in this case ($w_i = 1$), greatly improves the reconstruction (Figure 3-28 green line) and reduces the spectral leakage in the off-resonance slices (Figure 3-29 green line) but it does not eliminate it. Even without postcompensation, appropriate precompensation weights result in a more accurate reconstruction (Figure 3-28 and Figure 3-29, red line). The ringing in object profiles in Figure 3-28 is normal Gibbs ringing which is eliminated through filtering.

Figure 3-27 Reconstructed RSI image with no precompensation ($w_i = 1$) and no postcompensation

On-Resonance Slice No Pre/Post Compensation (w$_i$=1)
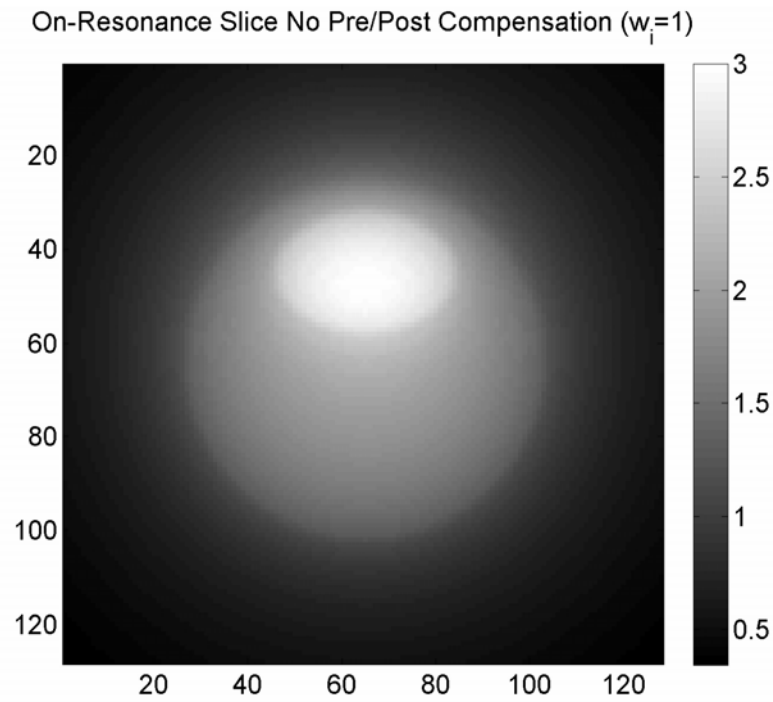
Figure 3-28 Object Profile Comparison: $w_i = 1$ (w/ and w/o postcomp) and for $w_i = dA_i$

On-Resoance Slice Profile || y-axis through K=0

w$_i$=1 no post
w$_i$=1 postcomp
w$_i$=dA$_i$ no post
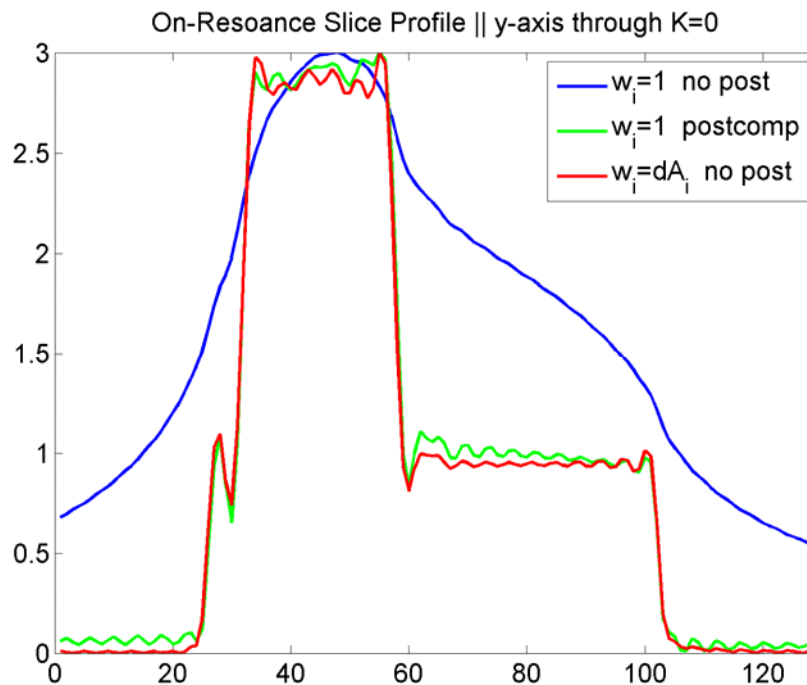
Figure 3-29 Spectral leakage produced by incorrect data weighting
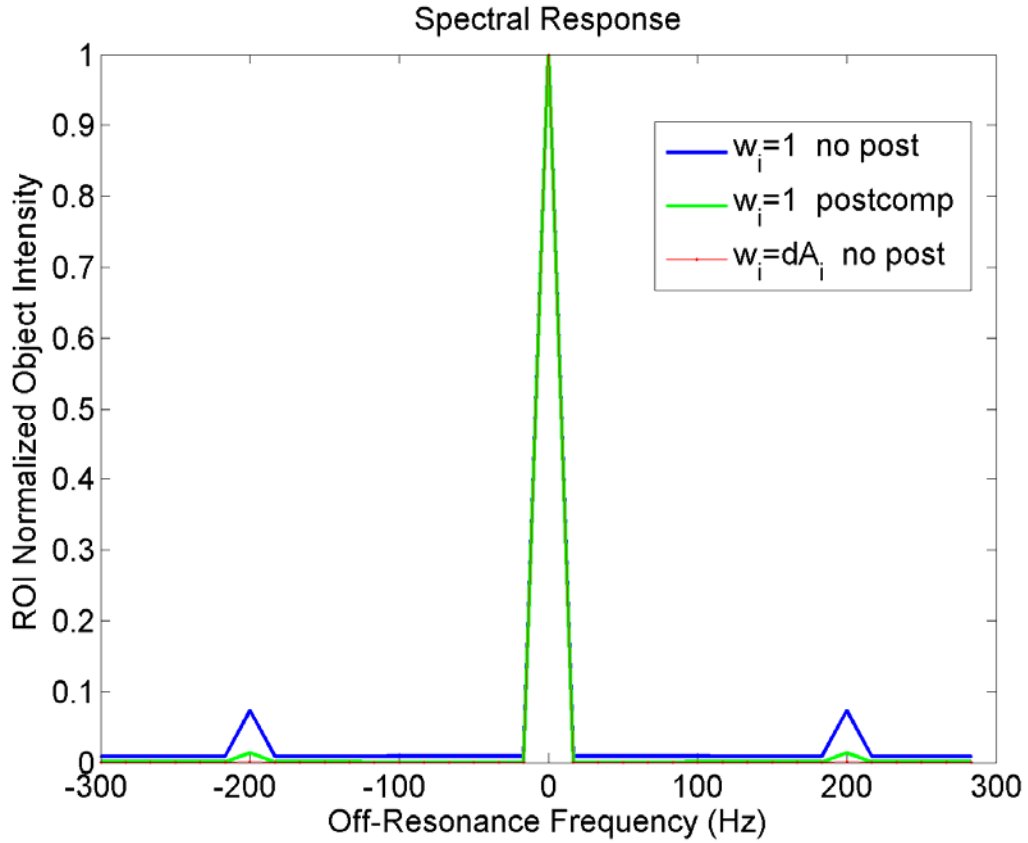
3.5.2 Correcting for B_0 inhomogeneities

Once a B_0 field map is available (a self-derived map can be obtained as in section 3.8.3), the reconstruction can be adapted to correct for B_0 inhomogeneities. We implement the algorithm developed by Irarrazabal *et al.* [19]. This is a linear correction in which only the linear terms of the field inhomogeneities $f(x, y)$ are considered. $f(x, y)$ is approximated as $\hat{f}(x, y)$, with α and β, constants determined through a maximum likelihood fitting procedure:

$$\hat{f}(x, y) = f_0 + \alpha \cdot x + \beta \cdot y \tag{3.99}$$

78

The original K-t space trajectories (k_x, k_y) are substituted in reconstruction by the corrected for linear inhomogeneities trajectories (k_x', k_y'):

$$k_x' = k_x + \alpha \cdot t$$
$$k_y' = k_y + \beta \cdot t$$

(3.100)

3.6   RSI PERFORMANCE

3.6.1   Sensitivity of a CSI experiment

An extensive analysis [50] compared a number of fast CSI methods to the gold standard Cartesian CSI in terms of sensitivity (defined as the ratio of the SNR to the square root of the total acquisition time) and minimal duration of the experiment. The study found that, while all the techniques provide for a speed-up in data acquisition, their sensitivity per unit time is generally lower than for classical CSI acquisition. A short overview of the work presented in the above-mentioned analysis follows below.

Introduced by Parker *et al.* [42] as an efficiency figure of merit in an imaging context, the SNR divided by the square root of the imaging time, the sensitivity of a spectroscopic imaging experiment is [50]:

$$\Psi = \frac{SNR}{\sqrt{T_{tot}}} = \frac{1}{N_x \cdot N_y} \cdot \frac{A \cdot f_x \cdot f_y \cdot f_\delta \cdot V_{prep}}{a \cdot \sqrt{N_x \cdot N_y \cdot N_\delta \cdot \Delta f} \cdot \sqrt{T_{tot}}}$$

(3.101)

The first term $1/(N_x \cdot N_y)$ describes the voxel size: the higher the spatial resolution, the smaller the voxel size and the signal originating in one voxel.

When a large number of repetitions are used, the system approaches a steady state and the amplitude of the Free Induction Decay (FID) in the time domain represented by the factor A, is the same for every excitation:

$$A_{FID}(T_R, \alpha) = M_0 \cdot \frac{1 - e^{-T_R/T_1}}{1 - \cos \alpha \cdot e^{-T_R/T_1}} \cdot \sin \alpha \qquad (3.102)$$

For a spin echo experiment, which consists of an $(180^0 - \alpha)$ excitation pulse followed after a time $T_E/2$ by a 180^0 refocusing pulse:

$$A_{echo}(T_R, T_E, \alpha) = M_0 \cdot e^{-T_E/T_2} \cdot \frac{1 - e^{-T_R/T_1} + 2e^{-(T_R - 1/2 T_E)/T_1} - 2e^{-(T_R - 3/2 T_E)/T_1}}{1 - \cos \alpha \cdot e^{-T_R/T_1}} \cdot \sin \alpha \quad (3.103)$$

M_0 is the magnetization of the sample imaged in thermal equilibrium.

A_{FID}, A_{echo} are maximized by Ernst angle: $\cos \alpha_{Ernst} = e^{-T_R/T_1}$. For an FID experiment, the optimum acquisition time is $T_{AQ} \simeq 1.26 \cdot T_2^*$ and optimum repetition time T_R is between $1.2 \cdot T_2^*$ and $1.3 \cdot T_2^*$. For spin-echo experiments, the optimum acquisition time is $T_{AQ} = 2.52 \cdot T_2^*$ and the optimum T_R is between T_1 and $2 \cdot T_1$, depending on both T_1 and T_E.

f_x, f_y, f_δ describe the effect of the Fourier transformation on the signal in the two spatial and one spectral dimension.

V_{prep} is a method-dependent factor, which describes processes during the preparation period (phase encoding, etc.).

$T_{tot} = N_{rep} \cdot T_R$ is total acquisition time with N_{rep} being the total number of repetitions.

The standard deviation of the noise caused by electron fluctuations in coil and sample is given by the Johnson noise formula [50]:

$$< \sigma_t >= \sqrt{4 k_B T_c R} \cdot \sqrt{\Delta f} = a \cdot \sqrt{\Delta f} \qquad (3.104)$$

$$a = \sqrt{4 k_B T_c R} \tag{3.105}$$

a is a constant that depends on the temperature of the coil T_c and the coil resistance and Δf is the bandwidth of the filter used to avoid aliasing.

An FID is sampled in discrete time intervals according to the Shannon criterion:

$$\Delta t = 1 / \Delta f \tag{3.106}$$

The standard deviation of the noise in the frequency domain is:

$$< \sigma_\nu >^2 = \sum_{n=1}^{N} < \sigma_t >^2 = N < \sigma_t >^2 \tag{3.107}$$

$$< \sigma_\nu >= a \cdot \sqrt{N \cdot \Delta f} \tag{3.108}$$

This generates the $a \cdot \sqrt{N_x \cdot N_y \cdot N_\delta \cdot \Delta f}$ factors in the denominator in Equation(3.101).

The sensitivity of the classical CSI experiment is:

$$\Psi_{CSI} = \frac{A_{FID}(\alpha, T_R) \cdot e^{-\tau_G / T_2^*}}{a N_x N_y \sqrt{N_\delta \cdot \Delta \delta \cdot T_R}} \cdot f_{FID}(T_{AQ}, \Delta \delta) \tag{3.109}$$

The amplitude right after the excitation pulse is $A = A_{FID}(\alpha, T_R)$ (Equation(3.102)).

This is reduced by a factor $V_{prep} = e^{-\tau_G / T_2^*}$ due to the T_2^* decay during the time τ_G needed for phase encoding.

The effect of N_x phase encoding steps is a signal enhancement by N_x, giving rise to the factors $f_x = N_x$ and $f_y = N_y$.

The Fourier transform in the spectral dimension causes a factor

$$f_\delta = f_{FID}(T_{AQ}, \Delta \delta) = \sum_{n=0}^{N_\delta - 1} e^{-n \Delta t / T_2^*} \approx \frac{1}{\Delta t} \cdot \int_0^{T_{AQ}} e^{-t / T_2^*} dt = T_2^* \cdot \Delta \delta \cdot (1 - e^{-T_{AQ} / T_2^*}) \tag{3.110}$$

The transition from sum to an integral is possible in the approximation the dwell time Δt is much shorter than T_2^*, condition that is fulfilled in most CSI experiments.

A quality factor Ω, which relates the sensitivity of all fast methods to the classical CSI sequence as a function of the relevant experimental parameters, is defined:

$$\Omega_{sequence} = \frac{\Psi_{sequence}}{\Psi_{CSI}} \qquad (3.111)$$

In the work of Pohmann *et al.* it is determined that the sensitivity of the fast CSI experiments is lower than the sensitivity for classical CSI or spin echo CSI (SE-CSI) in all cases, with a few exceptions. We will investigate one of the claimed exceptions here because it can shed some light into how to design an efficient acquisition scheme and set the groundwork for comparing the RSI performance to CSI. It is claimed SPLASH (spectroscopic FLASH – Hasse *et al.* 1987) can achieve a sensitivity greater than CSI at very high spatial resolution N_x and very low spectral resolutions N_δ.

SPLASH consists of a gradient echo, the position of which is shifted with reference to the excitation pulse by a variable delay t_δ in N_δ subsequent repetitions. (A gradient echo is formed when the phase accumulated due to gradient encoding becomes zero $\int G(t) \cdot dt = 0$). Similar to echo-time encoding, one spectral point is sampled per repetition, already resolved in one spatial dimension. The second spatial dimension is phase encoded by a gradient between excitations and acquisition. For an entire experiment, $N_\delta \cdot N_y$ repetitions are needed, and in each of them, a gradient echo with N_x points is acquired. The repetition time is equal to that of optimized CSI sequence (called FLASH-CSI) with

$$T_R = T_{AQ} + \tau_G \approx T_{AQ} \qquad (3.112)$$

and $\alpha = \alpha_{Ernst}$, resulting in a difference in the total duration of $T_{CSI} / T_{SPLASH} = N_x / N_\delta$. The factor f_x in Equation (3.101) is replaced by the signal of the gradient echo. Since the acquisition in the presence of a read gradient usually is much shorter than T_2^* even for quite small gradients, this factor is approximately equal to N_x, which is the same as for phase encoding:

$$f_x = f_{FID}(T_{AQ}, \Delta f) = T_2^* \cdot \Delta f \cdot (1 - e^{-T_{AQ}/T_2^*}) \cong T_2^* \cdot \frac{1}{\Delta t_x} \cdot \frac{T_{AQ}}{T_2^*} = \frac{T_{AQ}}{\Delta t_x} = N_x \qquad (3.113)$$

$\Delta t_x = 1/\Delta f$ is the spatial dwell time.

The total difference in sensitivity of these two experiments thus is

$$\Omega_{SPLASH} = \sqrt{\frac{\Delta \delta \cdot T_{CSI}}{\Delta f \cdot T_{SPLASH}}} = \sqrt{\frac{\Delta \delta \cdot N_x}{\Delta f \cdot N_\delta}} \qquad (3.114)$$

It is claimed SPLASH can achieve a higher sensitivity than CSI for a very small spectral and high spatial resolution, and from the expression in equation(3.114), it appears it may be so. However, based only on equation(3.114), we claim this is not the case.

Using $\Delta t_x = 1/\Delta f$ and $\Delta t_\delta = 1/\Delta \delta$ (spectral dwell time), we rewrite Equation (3.114) as:

$$\Omega_{SPLASH} = \sqrt{\frac{\Delta \delta \cdot N_x}{\Delta f \cdot N_\delta}} = \sqrt{\frac{\Delta t_x \cdot N_x}{\Delta t_\delta \cdot N_\delta}} = \sqrt{\frac{T_{read}^{spatial}}{T_{read}^{spectral}}} \qquad (3.115)$$

$T_{AQ}^{SPLASH} = T_{read}^{spatial} = N_x \cdot \Delta t_x$ is the gradient echo readout or the time during which data is collected for one SPLASH repetition and $T_{AQ}^{CSI} = T_{read}^{spectral} = N_\delta \cdot \Delta t_\delta$ is the FID readout or the time during which data is collected for one CSI repetition.

While the claim made in [50] is correct for $T_{read}^{spectral} < T_{read}^{spatial}$ it involves using an FID readout that is shorter than T_2^* (the assumption $T_{read}^{spatial} < T_2^*$ was used to estimate f_x in Equation(3.113)). More importantly for the comparison of the two methods, since both sequences use the same repetition time T_R, it implies that the CSI readout is shorter than T_R (neglecting the gradient encoding

time τ_G required by both sequences). This corresponds to an artificial shortening/truncation of the CSI readout and contradicts the initial assumption/setting that the repetition time is approximately equal to the acquisition time (Equation(3.112)). If the setting in Equation(3.112) is observed, while for small spectral bandwidths SPLASH sensitivity can approach CSI sensitivity, however its performance is always sub unitary $\Omega_{SPLASH} < 1$ since $T_{read}^{spectral} > T_{read}^{spatial}$ and it falls rapidly as the spectral resolution increases, approximately as $1/\sqrt{N_\delta}$. In fact, because $T_{AQ}^{SPLASH} = \tau_G + (N_\delta - 1) \cdot \Delta t_\delta + T_{read}^{spatial}$, the only time the sensitivity of the SPLASH experiment equals the one for CSI is for imaging ($N_\delta = 1$). The delays t_δ (and the time from the end of the gradient echo acquisition to the beginning of the next excitation for that matter) during which the receiver is closed and no data is collected make the SPLASH sequence less efficient than CSI.

Allowing for more general sampling schemes, Cartesian and uniform, we propose a demonstration for the result of equation (3.115) as follows:

Theorem: The quality factor (SNR performance) of a fast CSI method using the same experimental setup, same flip angle (the same initial transversal magnetization) and the same repetition time as classical CSI is proportional to the square root of the ratio of the method's readout time to the CSI readout. For a fast CSI method with uniform K-t space coverage and square/cubic support, if the noise is white and uncorrelated, the quality factor is equal to $\sqrt{T_{method}^{read} / T_{CSI}^{read}}$.

Proof:

Let $N_{pts}^{total} = N_x \cdot N_y \cdot N_z \cdot N_\delta$ be the total number of points that properly sample the K-t space and let $N_{CSI}^{(1)} = N_\delta$ and $N_{method}^{(1)}$ the number of points sampled during one repetition time, with corresponding dwell times $\Delta t_\delta = 1/\Delta\delta$ and $\Delta t_{method} = 1/\Delta f$. The number of repetitions required for full coverage of K-t space are $N_{CSI}^{rep} = N_x \cdot N_y \cdot N_z = N_{pts}^{total} / N_{CSI}^{(1)}$ and $N_{method}^{rep} = N_{pts}^{total} / N_{method}^{(1)}$. Note that this implies uniform K-t space coverage; the *method* fully samples K-t without acquiring a point twice (non-uniform coverage will be considered later).

The signal at sampled point P in K-t space is (from equation (2.17) updated to include T_2^* relaxation):

$$S_P = \iiint_V M_{xy}(\vec{r}, t = 0) \cdot e^{-t_P / T_2^*} \cdot e^{-i \cdot 2\pi \cdot \vec{k}_P \cdot \vec{r}} \cdot d\vec{r} \qquad (3.116)$$

$P = (m, n, l, p)$ is a discrete position in K-t, sampled at time $t_P = p \cdot \Delta t_\delta$ and $\vec{k}_P = (k_x, k_y, k_z) = (m \cdot \Delta k_x, n \cdot \Delta k_y, l \cdot \Delta k_z)$, with m, n, l, p integer numbers.

Both methods compared have the same initial magnetization profile $M_{xy}(\vec{r}, t = 0)$, the T_2^* relaxation effect is the same e^{-t_P / T_2^*}, if the time position t_P is the same, and the phase accumulated $\varphi(\vec{k}_P) = -2\pi \vec{k}_P \cdot \vec{r}$ is the same for a position $\vec{k}_p$ in K-space, regardless of how position P was reached (regardless of the shape of the trajectory). Therefore, the signal at each point on the K-t grid is the same for the two methods:

$$S_{(m,n,l,p)}^{method} = S_{(m,n,l,p)}^{CSI} \qquad (3.117)$$

However, $\sigma_{(m,n,l,p)}^{CSI} = \sigma_{CSI} = a \cdot \sqrt{\Delta\delta}$ and $\sigma_{(m,n,l,p)}^{method} = \sigma_{method} = a \cdot \sqrt{\Delta f}$ for any position in K-t space; we can write:

$$\frac{SNR_{method}}{SNR_{CSI}} = \frac{S_{method} / \sigma_{method}}{S_{CSI} / \sigma_{CSI}} = \frac{\sigma_{CSI}}{\sigma_{method}} = \sqrt{\frac{\Delta\delta}{\Delta f}} \qquad (3.118)$$

$$\Omega_{method} = \frac{SNR_{method} / \sqrt{T_{method}^{total}}}{SNR_{CSI} / \sqrt{T_{CSI}^{total}}} = \sqrt{\frac{\Delta\delta}{\Delta f}} \cdot \sqrt{\frac{N_{CSI}^{rep}}{N_{method}^{rep}}} = \sqrt{\frac{\Delta\delta \cdot N_{method}^{(1)}}{\Delta f \cdot N_{CSI}^{(1)}}} = \sqrt{\frac{\Delta t_{method} \cdot N_{method}^{(1)}}{\Delta t_{\delta} \cdot N_{\delta}}} \quad (3.119)$$

$$\Omega_{method} = \sqrt{\frac{T_{method}^{read}}{T_{CSI}^{read}}} \quad\quad (3.120)$$

For a fast spin-echo CSI method, when using the same echo time T_E as for classical spin-echo CSI (SE-CSI), the result in equation(3.120) becomes:

$$\Omega_{SE-method} = \frac{\Psi_{SE-method}}{\Psi_{CSI}} = \frac{\Psi_{SE-CSI}}{\Psi_{CSI}} \cdot \frac{\Psi_{SE-method}}{\Psi_{SE-CSI}} = \Omega_{SE-CSI} \cdot \sqrt{\frac{T_{SE-method}^{read}}{T_{SE-CSI}^{read}}} \quad\quad (3.121)$$

It appears from the arguments and results presented above, an efficient acquisition scheme should try to acquire as much data as possible during one repetition. A pulse sequence that does that is PREP (projection-reconstruction echo planar imaging). An oscillating read gradient generates a train of N_{δ} gradient echoes with an echo spacing equal to the spectral dwell time Δt_{δ}, scanning a plane in K-t space in the spectral and one spatial dimension at each repetition. The gradient is rotated in each subsequent repetition in a projection imaging (PI) fashion, allowing for a reconstruction with a back-projection algorithm. The sensitivity of the experiment is optimized by using short repetition times and the Ernst angle. The acquisition time is as long as in classical CSI so, in principle, it could reach the same sensitivity. However because a finite time τ_s is needed for gradient switching at the edge of K-space, when the gradient is optimized such that only one spectral dwell time is used up with the gradient switching and acquisition of N_x points, Pohmann et al. [50] calculate the relative sensitivity of the PREP acquisition to CSI to be:

$$\Omega_{PREP} = \sqrt{1 - \tau_s \cdot \Delta\delta} \quad\quad (3.122)$$

We can rewrite equation (3.122) as:

$$\Omega_{PREP} = \sqrt{\frac{T_{read}^{USED}}{T_{read}}}$$ (3.123)

In this form, it is apparent again that the SNR performance of a fast CSI experiment is proportional to the square root of the length of the (useful) readout compared to the readout of the classical CSI experiment.

Different acquisition schemes could use different spectral (Δt_{δ}) and spatial (Δt_x) dwell times corresponding to different spectral $\Delta\delta$ and signal bandwidths Δf. We can explain the results obtained for the performance of the fast CSI methods in terms of "elementary" data samples collected by the scanner - the data samples collected at the fastest sampling rate dt corresponding to the fixed receiver bandwidth $\Delta f_{MAX} = BW_{RCV} = 1/dt$.

Equation (3.104) expresses the standard deviation of the noise as a function of the sampling bandwidth. For an elementary data sample:

$$<\sigma_0> = a \cdot \sqrt{\Delta f_{MAX}} = a \cdot \sqrt{BW_{RCV}}$$ (3.124)

When a spectral dwell time $\Delta t_{\delta} = N_{tmp} \cdot dt = 1/\Delta\delta$ is used, the signal from each K-t space cell can be envisioned as a simple average of N_{tmp} elementary data points. The effective standard deviation of the noise for the averaged data is:

$$<\sigma_{tmp}> = <\sigma_0> \cdot \sqrt{N_{tmp}} / N_{tmp} = <\sigma_0> / \sqrt{N_{tmp}}$$ (3.125)

It can be easily seen this is the same as:

$$<\sigma_{tmp}> = <\sigma_0> / \sqrt{N_{tmp}} = a \cdot \sqrt{BW_{RCV} / N_{tmp}} = a / \sqrt{dt \cdot N_{tmp}} = a / \sqrt{\Delta t_{\delta}} = a \cdot \sqrt{\Delta\delta}$$ (3.126)

For the spatial dimension, using a dwell time $\Delta t_x = N_{spatial} \cdot dt = 1/\Delta f$, $N_{spatial}$ elementary data points are averaged in each K-t space cell, resulting in:

$$<\sigma_{spatial}> = <\sigma_0> / \sqrt{N_{spatial}} = a \cdot \sqrt{BW_{RCV} / N_{spatial}} = a \cdot \sqrt{\Delta f} \qquad (3.127)$$

For the purpose of data reconstruction, K-t space is made up of $N_{pts}^{total} = N_x \cdot N_y \cdot N_z \cdot N_\delta$ unit cells. Each cell, or voxel, has a volume $\Delta V = \Delta k_x \cdot \Delta k_y \cdot \Delta k_z \cdot \Delta t_\delta$. While a fast CSI method covers K-t space in a shorter time than classical CSI, sampling more unit cells during one repetition, it deposits in each cell only $N_{spatial} = (\sigma_0 / a)^2 / \Delta f$ (equation(3.127)) elementary points vs. classical CSI that deposits $N_{tmp} = (\sigma_0 / a)^2 / \Delta \delta$ (equation (3.126)). $N_{tmp} > N_{spatial}$ since $\Delta \delta < \Delta f$. While the noise in each grid cell is proportional to $\sigma_0 \cdot \sqrt{N_{spatial}}$ and $\sigma_0 \cdot \sqrt{N_{tmp}}$ respectively, the signal is proportional to the number of points $N_{spatial} \cdot S$ and $N_{tmp} \cdot S$, therefore $SNR = S / \sigma$ is proportional to $\sqrt{N_{spatial}}$ and $\sqrt{N_{tmp}}$. The faster the acquisition method, the greater the signal bandwidth Δf, the smaller the number of points deposited in one cell during one repetition, the larger the number of averages necessary to match the number of points (thus, the SNR) deposited in a K-t space cell by classical CSI. The number of averages required to match the SNR is $NEX = N_{tmp} / N_{spatial} = \Delta f / \Delta \delta$. The assumption we made here is all elementary data points within one cell are equal to each other: not only is the noise the same for every point sampled, but in addition, the signal for all the points within a cell of K-t space is the same. This is a reasonable assumption if the volume of the cell is sufficiently small, the signal variation will be relatively small. However, when the volume of the cell becomes large, if a large spectral dwell time Δt_δ, or a large Δk is used, there could be large variations in signal amplitude and phase within one voxel.

Consider the Echo-Time Encoding experiment, which is similar to SPLASH described above, but spin echoes are used this time. $N_\delta \cdot N_y$ repetitions are needed instead of $N_x \cdot N_y$ for classical CSI. A read gradient is used for spatial encoding in one direction. The position of this gradient is shifted in subsequent repetitions by a variable time t_δ with respect to the maximum of the spin echo, thus encoding the spectral information. The second spatial dimension is resolved using a phase gradient. Pohmann *et al.*, calculate the total sensitivity of this experiment to be:

$$\Omega_{echo-time} = \sqrt{\frac{\Delta\delta \cdot N_x}{\Delta f \cdot N_\delta}} \cdot \Omega_{SE-CSI} \qquad (3.128)$$

Using the same arguments we used when we analyzed the SPLASH experiment ($\Delta\delta = 1/\Delta t_\delta$, $\Delta f = 1/\Delta t_x$), the result in equation(3.128) is the same as the result of our derivation in equation(3.121). In addition, observing the conditions set for comparing the performance of the two experiments, because $T_{read}^{spectral} \geq T_{read}^{spatial}$ (equality when $N_\delta = 1$), from equation(3.121), we obtain $\Omega_{echo-time} \leq \Omega_{SE-CSI}$. Based on the result derived, the two experiments have the same sensitivity only for imaging ($N_\delta = 1$), otherwise, for $N_\delta > 1$, the sensitivity of the spin-echo variant of classical CSI is always greater.

The Dixon method [14] to resolve water and fat, is an echo-time encoding experiment where the spectral resolution $N_\delta = 2$. For the first spectral point, the gradient echo takes place at the same time as the spin echo. The second spectral point is collected by positioning the gradient echo after or before the maximum of the spin echo by a time interval:

$$t_{\delta=2} = \pm\frac{1}{2\cdot(f_{Water} - f_{Fat})} \qquad (3.129)$$

For the first spectral point, the water and fat spins are in-phase and the image created is a sum of the water and fat images. The second spectral image, acquired at the time given by

(3.129), has the transversal magnetization of water and fat opposed (in anti-phase), and the image generated is the difference of the water and fat images. We have already shown based on the arguments presented above that the SNR performance of the Dixon method is lower than for a spin-echo variant of the classical CSI experiment ($\Omega_{echo-time} < \Omega_{SE-CSI}$ for $N_\delta = 2$). However, the demonstration was based on the assumption the signal within a voxel in K-t space is approximately the same. For a CSI experiment with two spectral points $N_\delta = 2$, that uses a spectral dwell time as large as the one in equation(3.129), the assumption of homogenous cells in K-t space is not correct anymore. During one spectral dwell time, the magnitude of the signal changes from a sum to a difference of two components of comparable strength. While classical CSI achieves a lower standard deviation for the noise by averaging more elementary points ($N_{tmp} = (\sigma_0/a)^2/\Delta\delta$) than the Dixon method ($N_{spatial} = (\sigma_0/a)^2/\Delta f$; $\Delta\delta < \Delta f$), it does so at the expense of averaging data points with largely different signal strengths, which decreases its spectral resolving power, making the Dixon method more suitable in this kind of experiment with very low spectral resolution ($N_\delta = 2$).

The arguments we used to explain why the performance of the classical CSI acquisition in this situation ($N_\delta = 2$) is lower than when using the Dixon method (namely, averaging the elementary data samples with widely different amplitudes is detrimental to spectral resolving power), can be applied to spatial encoding for both imaging and spectroscopic imaging. When using spatial dwell times larger than dt (the dwell time corresponding to the highest sampling rate available), it appears that for gradient echoes, multiple elementary data points are combined and assigned one position in K-space while they belong to slightly shifted positions along the echo. This suggests that, whenever possible, sampling the trajectories as often as possible, using a

90

sampling rate matching or as close as possible to the highest rate available on the scanner, provides a benefit trough better assignment of data to positions in K-space. This agrees with Parker *et al.* [42] who demonstrated that as long as the voxel size is maintained constant, one could image as many pixels in the readout direction as desired with no loss in SNR. However, this is done at the cost of higher computational time in data processing, which in the case of 3D imaging or spectroscopic imaging can become significant since data sets are already large.

So far, the SNR discussions have assumed only white thermal Johnson noise (equation(3.104)). The total noise in an MR image consists of at least three different noise sources [24]:

$$\sigma = \sqrt{\sigma_T^2 + \sigma_S^2 + \sigma_P^2} = \sqrt{\sigma_0^2 + \sigma_P^2} \qquad (3.130)$$

The thermal noise σ_T (equation(3.104)) and the systematic noise σ_S can be treated together as σ_0 (equation(3.124), different value for constant a). The physiological noise includes contributions from fluctuations in the basal brain metabolism and thus is signal dependent: $\sigma_P = \lambda \cdot S$. In a neuroimaging study at 1.5T and 3T, Kruger *et al.* [24] showed that, the increasing influence of the physiological noise would limit the achievable SNR at higher magnetic fields. They also argued that writing $SNR = S / \sigma$, one obtains:

$$SNR = \frac{SNR_0}{\sqrt{1 + \lambda^2 \cdot SNR_0^2}} \qquad (3.131)$$

$SNR_0 = S / \sigma_0$ is the SNR when no physiological noise is present and λ is a system-independent constant.

Using equation(3.131) and the result in equation(3.120), when physiological noise is considered in comparing the SNR performance of a fast CSI method to classical CSI:

$$\Omega_{method} = \sqrt{\frac{T_{method}^{read}}{T_{CSI}^{read}}} \cdot \sqrt{\frac{1 + \lambda^2 \cdot SNR_{0,CSI}^2}{1 + \lambda^2 \cdot SNR_{0,CSI}^2 \cdot \frac{T_{method}^{read}}{T_{CSI}^{read}}}} \tag{3.132}$$

Thus, a fast CSI method will perform somewhat better than $\sqrt{T_{method}^{read} / T_{CSI}^{read}}$ when the used acquisition time is shorter than the one for classical CSI ($T_{method}^{read} < T_{CSI}^{read}$) and signal dependant noise is present.

Kruger's study found that the physiological noise is of increasing influence at higher flip angles (larger signals), in fully relaxed images (long T_R's). Therefore, while the physiological noise might play a larger role in spin-echo experiments that use longer repetition times and larger flip angles, its effect on the SNR performance of a fast CSI method compared to classical CSI, will be less relevant for experiments optimized to use short T_R's and Ernst angle.

3.6.2 RSI Performance

As described in the introductory section, the Rosette trajectories consist of a radial and angular oscillation and they generate a train of N_δ gradient echoes with an echo spacing equal to the spectral dwell time Δt_δ (section3.3), encoding simultaneously the two spatial and the spectral dimension. The gradient radial component becomes null at the edge of K-space ($K = K_{max}$) and they return to the center of K-space ($K = 0$) in a periodic fashion and no time is spent for gradient switching that would be unusable in data reconstruction. The acquisition time can be as long as for CSI. Furthermore, the acquisition can start immediately after the end of the excitation pulse, unlike CSI where phase encoding gradients are required.

The first obvious difference between RSI and CSI is the rosettes encode a disk of radius $R = K_{max}$ in K-space (cylinder in K-t space) while in the case of CSI a square is encoded with the side equal to $L = 2 \cdot K_{max}$; the second obvious difference is data encoded with CSI is laying on a Cartesian grid while for RSI it is not.

Because RSI has circular support it is more appropriate to compare it to a disk supported CSI which encodes only the K-space positions inside a circle of radius $R = K_{max}$ rather than the whole square and thus, the total acquisition time for the disk supported CSI is only $\pi/4$ of the square supported CSI. As noted by Bernstein *et al.* [4], techniques covering a disk rather than a square in $K_x - K_y$ space may have an intrinsic SNR advantage. In fact, our results (Section 3.7) show an increase in SNR of $\cong \sqrt{4/\pi}$ for a disk supported CSI vs. the square supported CSI acquisition, which suggest the high-frequency information in the corners of K-space contribute little power to the measured signal. Since the time required for a CSI acquisition with K-space disk support is $\pi/4$ shorter than for a CSI with square support,

$$\Omega_{diskCSI} = \sqrt{4/\pi} / \sqrt{\pi/4} = 4/\pi \simeq 1.27 \qquad (3.133)$$

Equation (3.133) is valid when no spatial filters are applied. However, spatial filters are typically used in the reconstruction process and for a filter that completely removes the corners of K-space of a square supported CSI acquisition, the SNR will become the same as for the disk supported CSI acquisition. The advantage provided by a faster total acquisition due to a lower number of phases encoded remains:

$$\Omega_{diskCSI} = 1/\sqrt{\pi/4} = \sqrt{4/\pi} \simeq 1.13 \qquad (3.134)$$

In general, for a filter that does not completely remove the corners of K-space (e.g. Fermi filter, etc.):

$$\Omega_{diskCSI} = b \tag{3.135}$$

b will have a value in between the ones given by equations (3.133) and (3.134):

$$b \in [\sqrt{4/\pi}; 4/\pi] \tag{3.136}$$

The second difference between RSI and CSI is that in the case of RSI the data is collected using non-Cartesian trajectories. More importantly, unlike CSI, the sampling is not uniform. To understand how non-uniform sampling affects the SNR, please see Pipe *et al.* 1995 [48]. For the same acquisition time, the trajectory with non-uniform sampling will have lower SNR than the one sampling uniformly.

Thus, the RSI performance relative sensitivity to the disk supported CSI is:

$$\Omega_{RSI} = \eta \cdot \Omega_{diskCSI} \tag{3.137}$$

As shown in section 3.4, when the number of excitations approaches the number given by equations (3.83) and (3.87), the rosette trajectories achieve their highest sampling efficiency $\eta_{RSI} = 1/\sqrt{\pi^2/8} = .90$.

In addition to the two main differences between RSI and CSI discussed above, the rosette acquisition can start immediately after the end of the RF excitation pulse, unlike CSI where encoding gradients of duration τ_G are necessary for encoding the K-space positions before an FID is collected. During this time τ_G, because of the T_2^* relaxation, the CSI signal becomes smaller by a factor e^{τ_G/T_2^*}.

In conclusion:

$$\Omega_{RSI} = \eta_{RSI} \cdot b \cdot e^{\tau_G/T_2^*} \tag{3.138}$$

The SNR performance of RSI compared to CSI is affected by four factors. Since the rosette trajectories do not spend time covering the corners of K-space, gives RSI an advantage of up to 27% (b factor). Secondly, this advantage is reduced by the non-uniform sampling by ~10%

(η_{RSI} factor). Third, because the RSI acquisition, unlike CSI, can start right after the end of the RF pulse, there is potential signal to be gained (e^{τ_G/T_2^*} factor). Finally, the same acquisition time ($T_{read}^{RSI} = T_{read}^{CSI}$) puts the two methods on the same footing. Because the acquisitions are already optimized for a readout time equal to $1.26 \cdot T_2^*$ that maximizes the SNR [50], the possible longer readout for RSI ($T_{read}^{RSI} = T_{read}^{CSI} + \tau_G$), can only help in slightly increasing the spectral resolution $df = 1/T_{read}$. Readouts longer than $1.26 \cdot T_2^*$ result in lower SNR for an unfiltered FID. However, the SNR lost because of the longer acquisition time can be completely recovered using a matched temporal filter e^{-t/T_2^*}.

In the light of the arguments presented, we also update the relation for the performance of the PREP technique:

$$\Omega_{PREP} = \eta_{PI} \cdot b \cdot \sqrt{1 - \tau_s \cdot \Delta\delta} \qquad (3.139)$$

$\eta_{PI} = \sqrt{3}/2 \simeq .87$ is the sampling efficiency of the PI acquisition technique.

3.7   SIMULATION STUDIES

For all the simulation studies (spectral response-section3.2, etc…), we used synthetically generated ellipses and disks. The analytical expression for an on-resonance ellipse of major semi axes a, b with the center at a_0, b_0, sampled in K-space at position (k_x, k_y) can be shown to be:

$$E(k_x, k_y) = \frac{a \cdot b}{\sqrt{(a \cdot k_x)^2 + (b \cdot k_y)^2}} \cdot J_1(2\pi \cdot \sqrt{(a \cdot k_x)^2 + (b \cdot k_y)^2}) \cdot e^{-i \cdot 2\pi \cdot (a_0 \cdot k_x + b_0 \cdot k_y)} \quad (3.140)$$

$J_1(\cdot)$ is the Bessel function of the first kind, of order one, with the limit at the center of K-space ($k_x = 0, k_y = 0$):

$$\lim_{x \to 0}(\frac{J_1(2\pi \cdot x)}{x}) = \pi \tag{3.141}$$

An elliptical object at off-resonance frequency ω, with relaxation T_2^*, will be described by a time dependent function:

$$E(k_x, k_y, \omega, t, T_2^*) = E(k_x, k_y) \cdot e^{i \cdot \omega \cdot t} \cdot e^{-t/T_2^*} \tag{3.142}$$

Multiple objects with different spatial and spectral positions were generated and reconstructed in order to verify the fidelity of the reconstruction program.

We proceed to verify the predictions made for the RSI sensitivity performance in section 3.6.2, equation(3.138). The e^{τ_G/T_2^*} factor was neglected and the readout for the CSI and RSI acquisitions was set the same for a given spatial resolution N_x and spectral bandwidth $\Delta\delta$. The spatial resolution was first fixed to $N_x = 64$ and the spectral bandwidth $\Delta\delta$ was allowed to take values between $100\,Hz$ and $900\,Hz$ in steps of $50\,Hz$. The trajectories were designed as in section 3.3, for one set of trajectories (no temporal interleaves, $n_{TI} = 1$), and one petal per trajectory per temporal slice (two half petals, $n_{hptls} = 2$). Maximum twist (greatest ω_2/ω_1) allowed by hardware constraints (G_{max}^{HW}, S_{max}^{HW}) and signal bandwidth/sampling rate (equation(3.42)) was used. One disk at the center of the field of view with a diameter $D = .6 \cdot fov$, was generated on-resonance using the minimum number of excitations N_{sh}^{calc} determined using the simulation program described at the beginning of section 3.4 and also the theoretically estimated number N_{sh}^{est} given by equations(3.83), (3.87). Uncorrelated white noise with the same standard deviation was added to the imaginary ($\sigma_0^2/2$) and real data ($\sigma_0^2/2$). The precompensation weights were taken to be equal to the 2D Voronoi weights calculated in each temporal slice as described in section 3.5.1,

step 1D. The simulated object and the regions inside the on-resonance frequency slice used to measure the SNR are shown in Figure 3-30.

Figure 3-30 Simulated Object and Signal and Noise regions used to measure the SNR
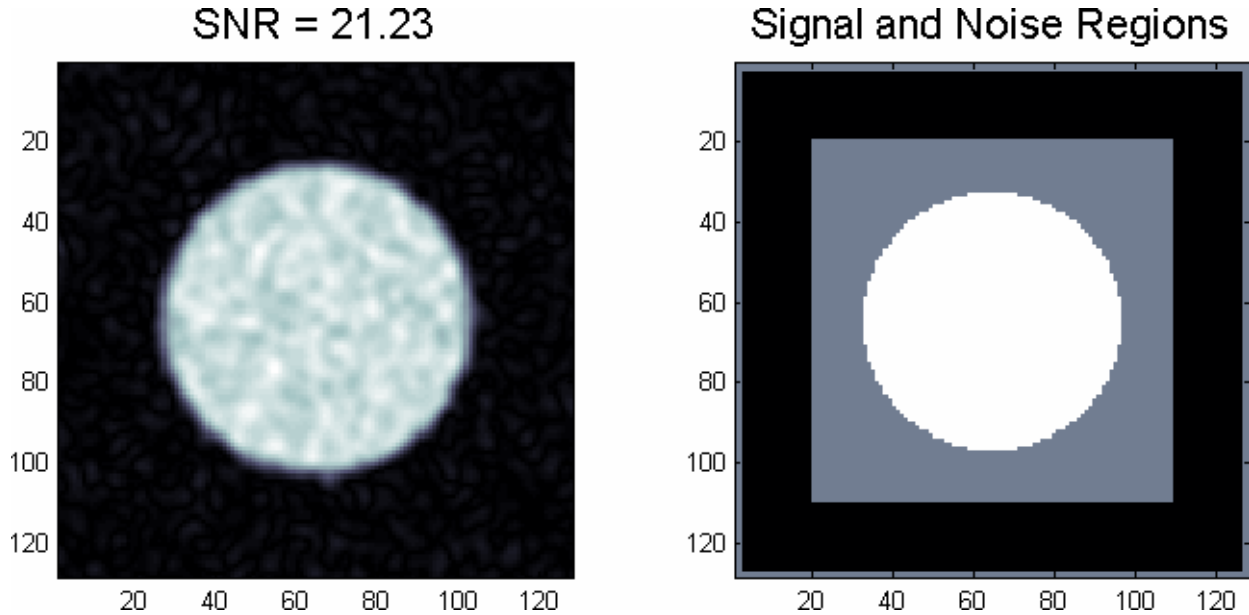
Before proceeding to compare the RSI results to the CSI results, we realized that, while for the theoretically estimated number of excitations N_{sh}^{est}, the reconstructions using postcompensation produce barely different SNR results compared to when no postcompensation is used (approx. 2-6% increase), for the minimum number of excitations N_{sh}^{calc}, the increase in SNR when using postcompensation was up to 40%. We conclude the postcompensation process, while indispensable when precompensation is not used (section 3.5.1) or the precompensation weights are not correctly calculated (Figure 3-24), should be regarded as filtering (that is, in addition to explicit filters typically applied during reconstruction (section 3.5.1, step 2). Our conclusion is supported not only by the increased in SNR observed by us when using postcompensation, but also by observations made by others that noted a reconstruction performed with appropriate precompensation weights produces a better image than the same reconstruction when in addition, postcompensation is used [31]. The "better" image refers to

more detail, which is lost when postcompensation is applied, an effect similar to filtering. The effect of approx. 30-40% increase in SNR is small compared to the increase obtained when applying the Hanning filters discussed in data reconstruction section, equations(3.94), (3.95) (approx. 350% increase in SNR for the object/geometry considered). However, it is comparable in size to the SNR advantage (~14%) we expect the RSI acquisition will have *vs.* CSI. For this reason, we will compare only RSI acquisitions using the theoretically estimated number of excitations N_{sh}^{est}, for which the analytically estimated precompensation weights are the same as the 3D Voronoi weights (Figure 3-25) and no postcompensation will be used.

For spatial resolution $N_x = 64$, $T_{AQ} \simeq 130ms$, spectral bandwidth $\Delta\delta$ from 100 to 900 Hz, in steps of 50 Hz, we simulate and reconstruct the RSI data, the CSI data with K-space square and disk support, a number of 10^3. Noise is added to the simulated data using the *randn* function in Matlab, each time with a different starting seed. The sensitivity ($\Psi = SNR/\sqrt{T_{tot}}$), the ratio of the SNR measured to the square root of the total acquisition is calculated for RSI ($S_{RSI}(\Delta\delta) \pm e_{RSI}(\Delta\delta)$), CSI ($S_{CSI}(\Delta\delta) \pm e_{CSI}(\Delta\delta)$) and disk CSI ($S_{dCSI}(\Delta\delta) \pm e_{dCSI}(\Delta\delta)$), where $S(\Delta\delta)$ and $e(\Delta\delta)$ represent the mean and standard deviation of the sensitivity for the 10^3 measurements. In Figure 3-31, we plot the results normalized to the CSI sensitivity, which is assigned a unitary value (for all $\Delta\delta$'s). The relative sensitivity displayed for RSI is:

$$\frac{S_{RSI}(\Delta\delta)}{S_{CSI}(\Delta\delta)} \pm \frac{e_{RSI}(\Delta\delta) + e_{CSI}(\Delta\delta)}{S_{CSI}(\Delta\delta)} \tag{3.143}$$

Thus, the mean value displayed is $S_{RSI}(\Delta\delta)/S_{CSI}(\Delta\delta)$ with the size of the error bars equal to $(e_{RSI}(\Delta\delta) + e_{CSI}(\Delta\delta))/S_{CSI}(\Delta\delta)$.

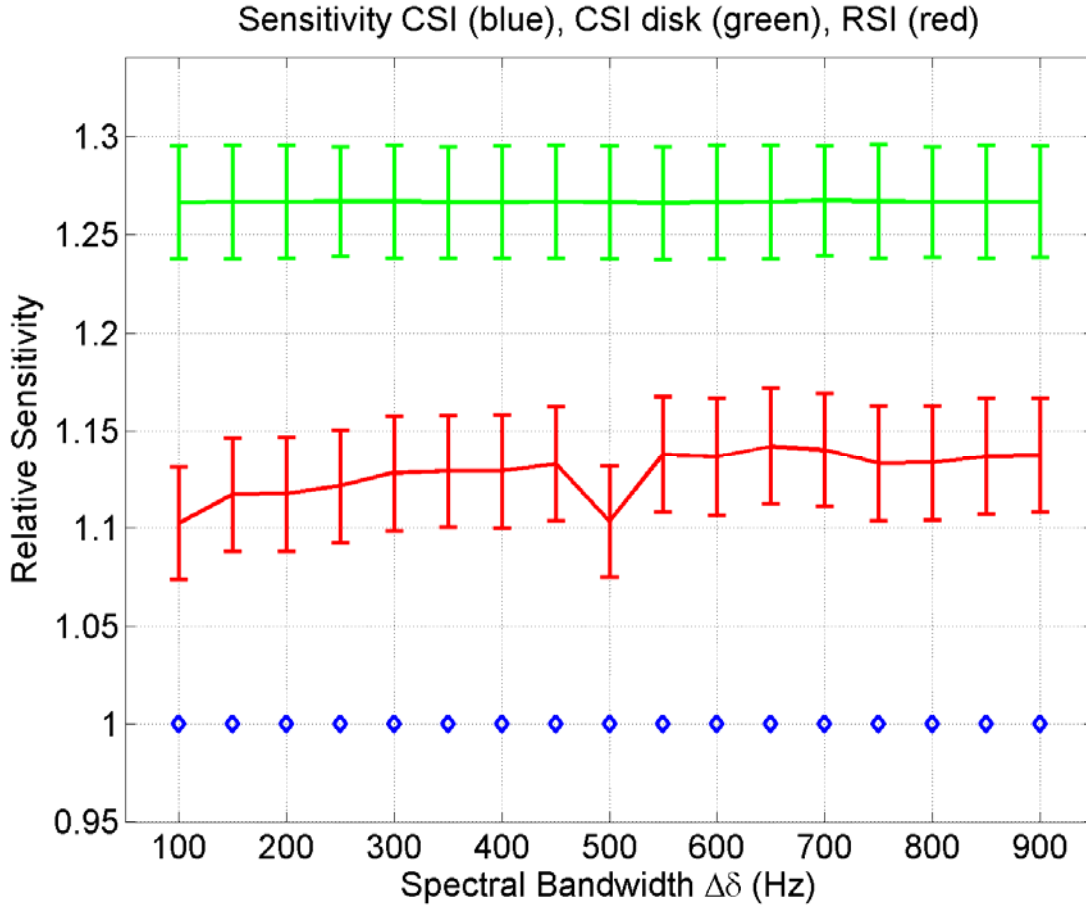The relative sensitivity displayed for CSI with K-space disk support is

98

$$\frac{S_{dCSI}(\Delta\delta)}{S_{CSI}(\Delta\delta)} \pm \frac{e_{dCSI}(\Delta\delta) + e_{CSI}(\Delta\delta)}{S_{CSI}(\Delta\delta)} \qquad (3.144)$$

Figure 3-31 RSI relative SNR sensitivity $N_x = 64$ $(10^3$ **noise seeds)**

Neglecting again e^{τ_G/T_2^*}, keeping spectral bandwidth fix at $\Delta\delta = 600 Hz$, $N_\delta = 34$,

$fov = 18cm$ we verify the prediction of equation(3.138) for spatial resolutions from $N_x = 20$ to

$N_x = 128$ (in increments of two). A thousand (10^3) different seeds are used for noise added to

RSI, CSI (disk and square supported) data. Normalizing again the CSI sensitivity to unity, the

relative RSI and disk CSI sensitivity (and error bars) displayed in Figure 3-32 are defined as in

equations(3.143), (3.144), but now they are functions of the spatial resolution N_x. At lower

spatial resolutions N_x, the error bars are larger than at higher N_x's since fewer points are used in

reconstruction. In addition, for disk CSI, due to the discrete nature of K-space sampling, at small N_x's a slightly smaller or larger number of points than the theoretical $\pi \cdot N_x^2 / 4$ will make it into the reconstruction. The RSI relative sensitivity to square supported CSI closely approaches the theoretical value for unfiltered reconstruction: $\Omega_{RSI} \approx 1.14$. In addition, the disk supported CSI relative sensitivity: $\Omega_{dCSI} \approx 1.27$.

Figure 3-32 RSI relative SNR sensitivity $\Delta\delta = 600$ (10^3 noise seeds)

Sensitivity CSI (blue), CSI disk (green), RSI (red)
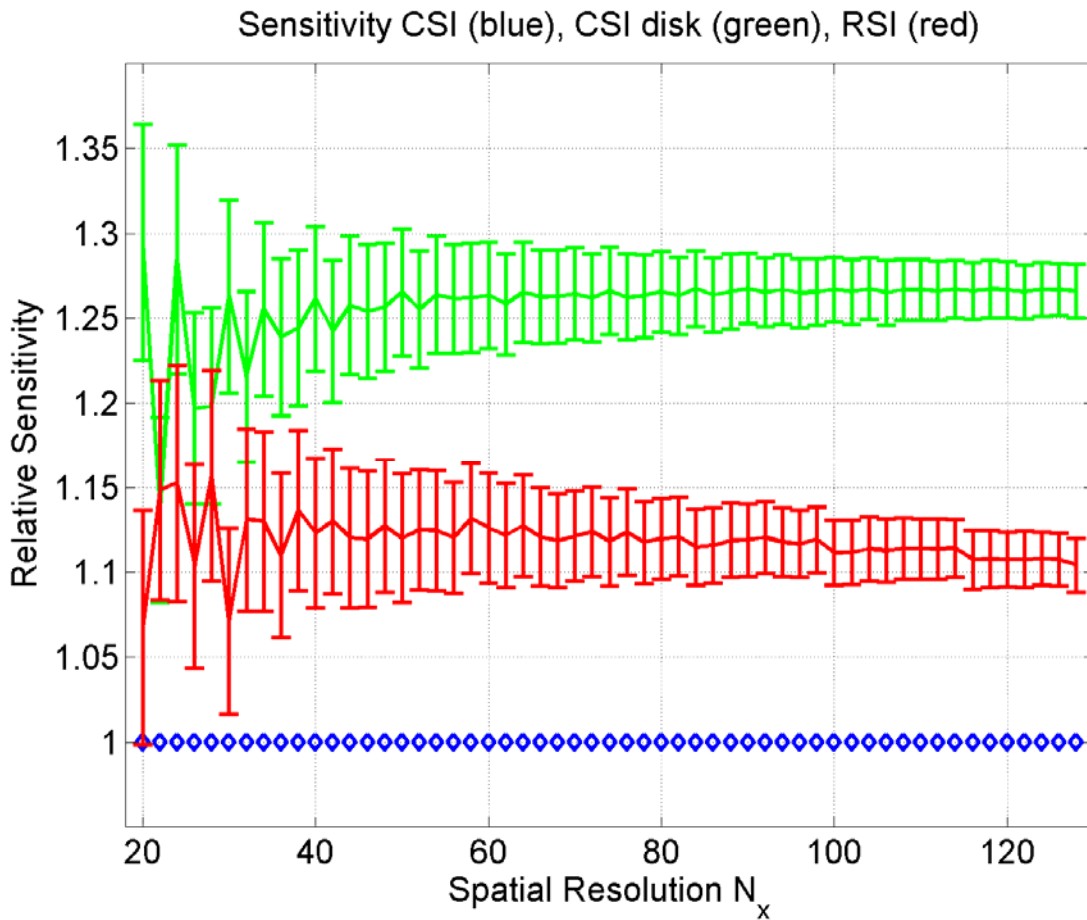
3.8 EXPERIMENTAL RESULTS

To demonstrate experimentally the RSI technique, we wrote a pulse sequence in EPIC (Environment for Pulse programming In C) and implemented on a General Electric 3Tesla whole body MRI scanner. For this machine, the peak gradient can reach $G_{max}^{HW} = 4G/cm$ and the slew rate $S_{max}^{HW} = 15G/cm/ms$. A slice selection pulse with an RF waveform and G_z gradient identical to the one used in the standard CSI sequence available on the scanner was implemented in the sequence. The magnetization flip angle was optimized such a maximum signal from the excited slice is obtained. This was done before actual acquisition, by varying the transmission gain (TG) and collecting a number of FIDs for each TG value, with the readout/encoding gradients amplitude set to zero and the repetition time the same as the one used for data collection. Because the RF slice selection pulse is the same as the one used in the standard FIDCSI sequence, an approach to obtaining a better excitation slice profile would be to use custom designed RF composite spin-echo pulses tailored for the flip angle used [26]. The gradient waveforms, tailored for each spatial resolution and spectral bandwidth, designed as in section 3.3, are loaded as external waveforms at run time.

3.8.1 Phantom experiments

A plastic bottle filled with commercial Canola oil was used to determine the technique's ability to resolve multiple spectral resonances. Two ($n_{TI} = 2$) temporally interleaved sets of trajectories with $f_1 = 300Hz, f_2 = 584Hz$ were used to achieve a spatial resolution $N_x = 64$ and a spectral bandwidth $\Delta\delta = 1200Hz$. The number of shots to cover K-t space was chosen $N_{sh}^{RSI} = 2 \cdot 64$

which is greater than the minimum number of excitations determined using the simulation program $N_{min} = 2 \cdot 34$, but about 20% less than the theoretical number calculated using equation(3.87), $N_{th}^{RSI} = 2 \cdot 77$. Slice thickness was $\Delta z = 2mm$, repetition time $T_R = 285ms$ and the readout (acquisition) time $T_{AQ} = 62.5ms$. Data was sampled every $dt = 8us$. The spectral resolution, after discarding during reconstruction the data collected in the first temporal slice for the first set of trajectories and data in last temporal slice for the second time-interleaved set, was $N_\delta = 74$. An enhancement in spatial resolution by a factor of two was used by zeropadding the data in the x, y directions. Only the central 64 spectral slices (out of 74) are displayed in Figure 3-33 covering a range of 1038Hz (out of 1200Hz).

Figure 3-33 RSI: Spectroscopic Image of an oil bottle phantom, RSI acquisition
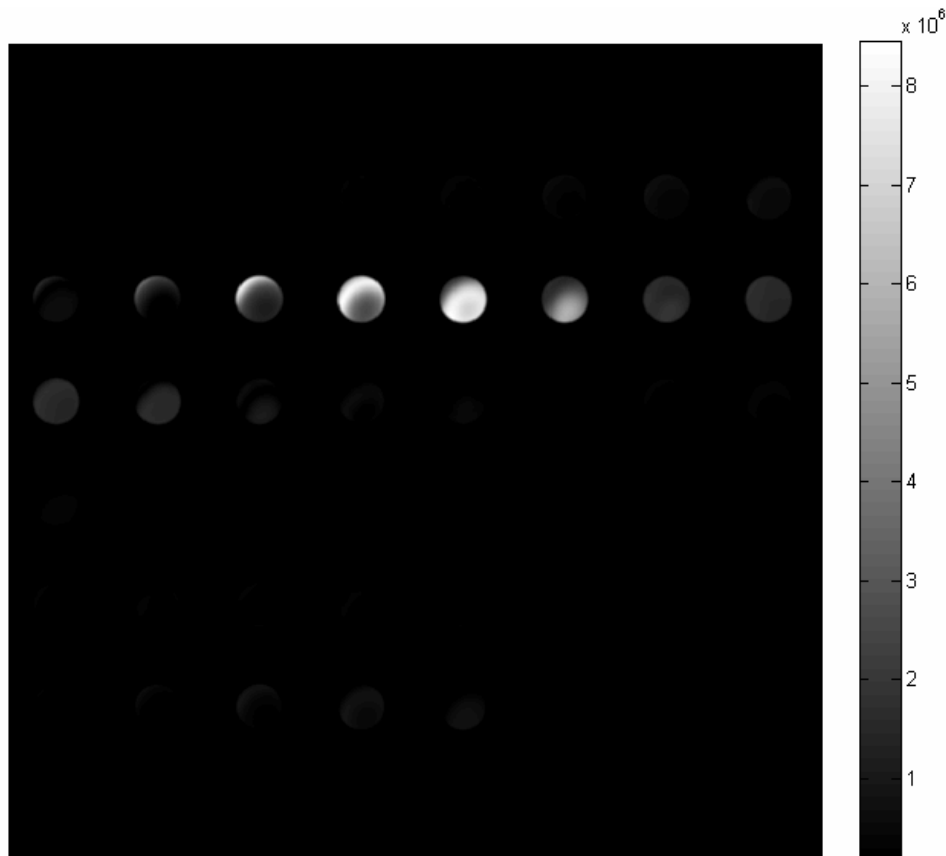
While a self-derived B_0 map can be obtained as in section 3.8.3 and the B_0 correction performed as in 3.5.2, in this case, because of the simplicity of the phantom, we chose the easier approach of aligning the spectra. For each spatial position, the location of the strongest resonance is determined and over the entire phantom, a median position for this resonance is calculated, with the difference between the two giving also a self-derived map Figure 3-34. Next, spectra in each spatial voxel are shifted in frequency such the new location for the strongest resonance is the same for each voxel and equal to the median position calculated (Figure 3-35).

Figure 3-34 Oil bottle B_0 map (Hz)
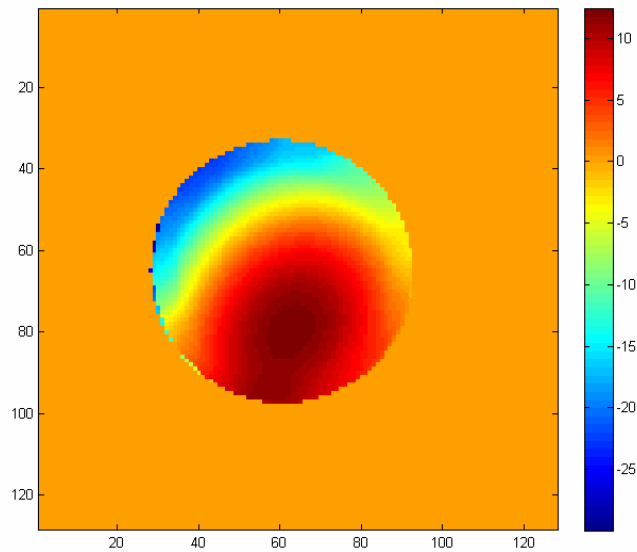
Figure 3-35 RSI: Oil bottle with B_0 correction
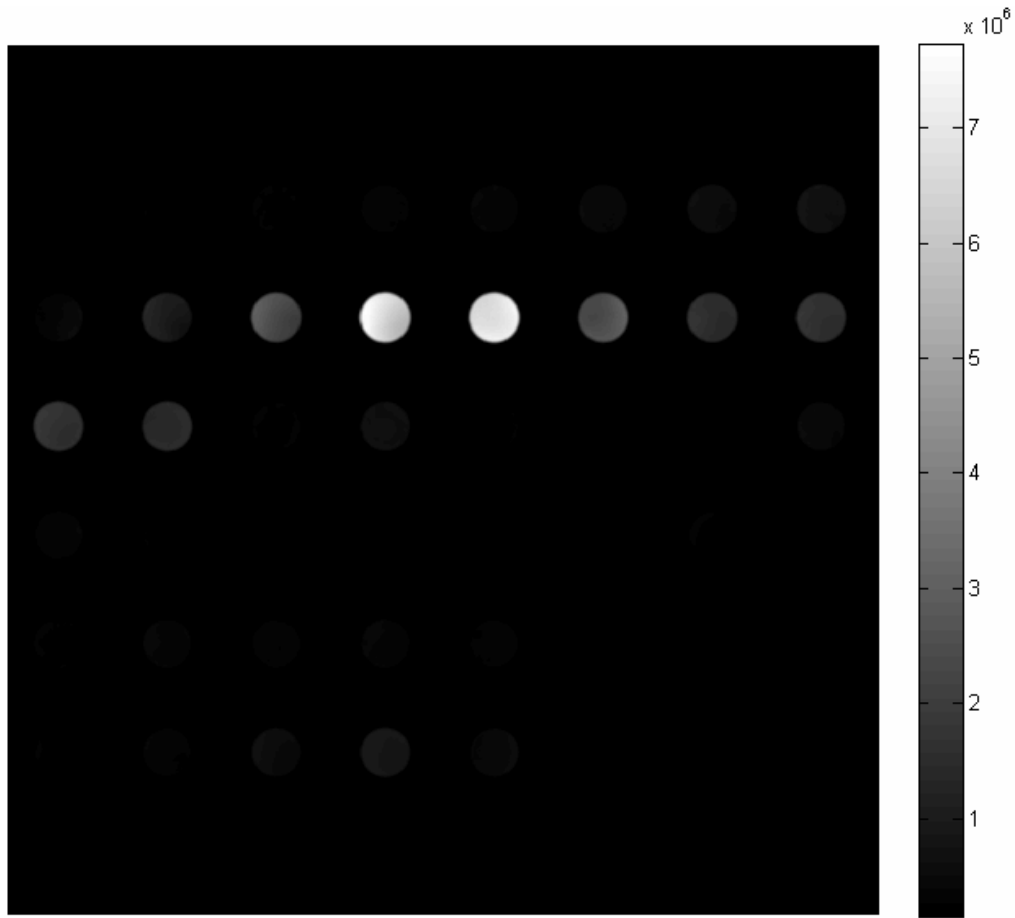
The spectral profile for the RSI acquisition (Figure 3-36), which we calculated (after correcting for B_0) as intensity of the signal over the entire FOV in each spectral slice, is compared to the spectral profile for a standard CSI acquisition (Figure 3-37). The same experimental setup (same phantom, excitation pulse, T_R) was used and the spatial/spectral resolution were the same as for RSI ($N_x = 64$, $N_\delta = 74$, $\Delta\delta = 1200 Hz$).

Figure 3-36 Spectral Profile, RSI Acquisition Oil Bottle with B_0 correction

Figure 3-37 Spectral Profile, FIDCSI Acquisition Oil Bottle with B_0 correction

3.8.2 *In Vivo* Experiments

In the early stages of the technique's development, ^{31}P data was collected from a leg of a healthy human volunteer. One multishot set of $N_{sh} = 32$ rosette trajectories was employed, with
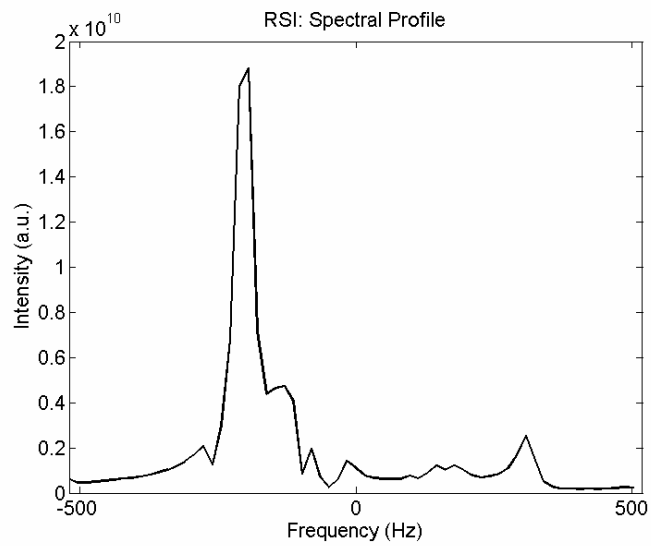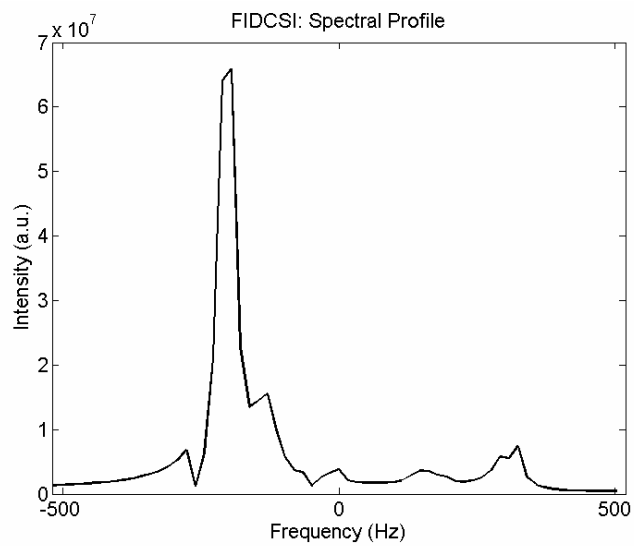
$f_1 = 1196Hz$ and $f_2 = 372Hz$. Two averages $NEX = 2$ were used. Spatial resolution was $N_x = 14$ and spectral bandwidth $\Delta\delta = 2 \cdot f_1 = 2392Hz$. Slice thickness was $\Delta z = 2cm$, $fov = 20cm$, repetition time $T_R = 4seconds$ and the readout (acquisition) time $T_{AQ} = 50.2ms$. Data was sampled every $dt = 8us$. Out of the $N_\delta = 120$ reconstructed slices, only the ones in the range -1000Hz to 400Hz are displayed in Figure 3-38, with a 20Hz separation between them. Spatial resolution was digitally enhanced to $N_x = 64$, through zeropadding the data in the x, y directions. Besides the central resonance, one can identify three other resonances at -800Hz, -400Hz and at 200Hz (Figure 3-38 and Figure 3-39).

Because of hardware problems with the MRI scanner's broadband multinuclei channel that occurred a few months after this ^{31}P data set was collected, we were not able to acquire at a later time new ^{31}P data using optimized parameters for higher spatial resolution images and/or shorter repetition times.

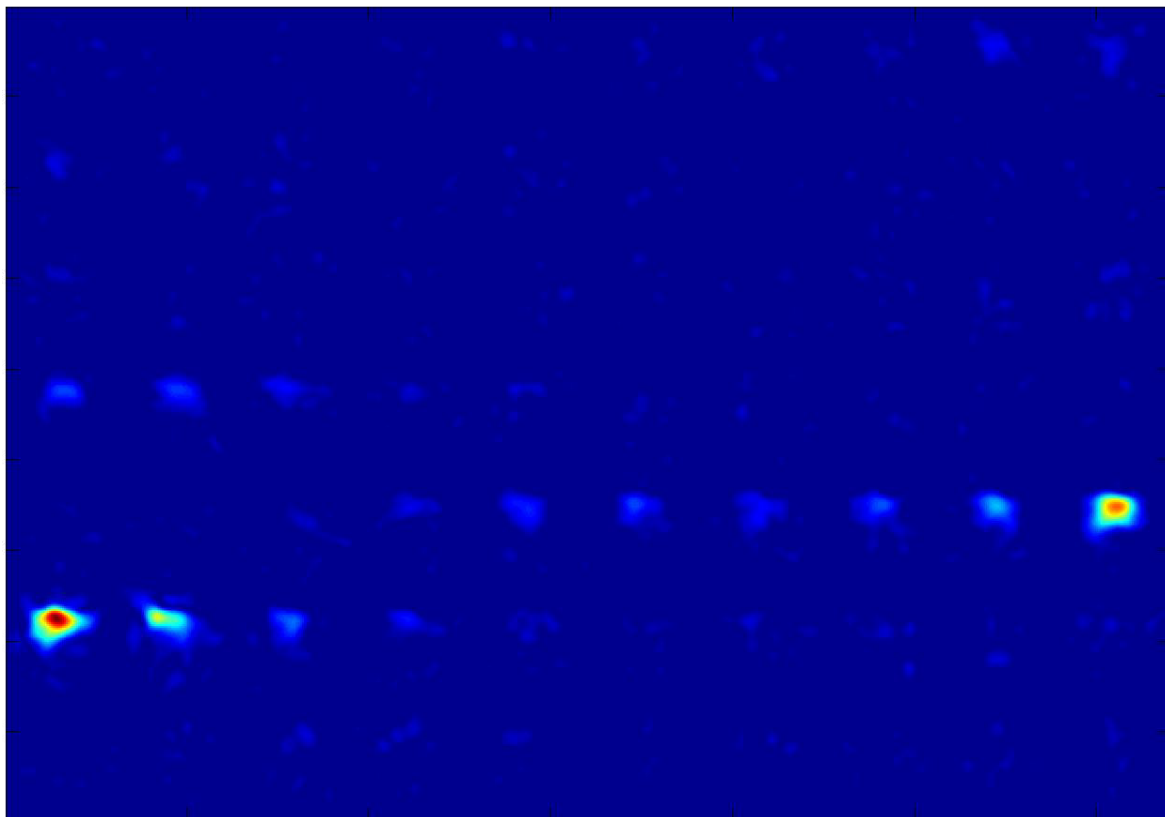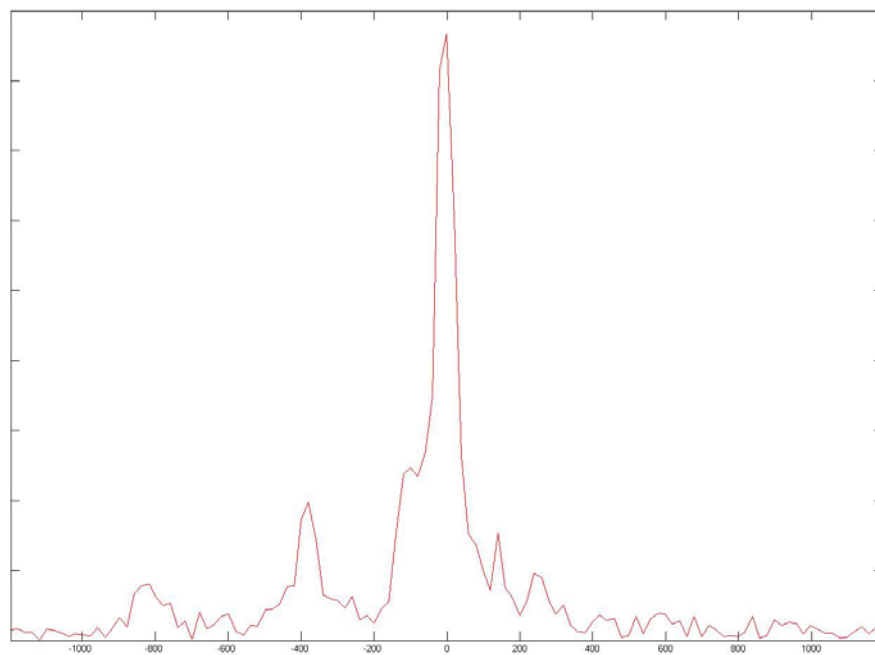**Figure 3-38 RSI: Leg ^{31}P Spectroscopic Image $N_x = 14$, $\Delta\delta = 2.4kHz$. Displayed -1 kHz to 400Hz**

Figure 3-39 Leg ^{31}P RSI: Spectral Profile through all slices (image intensity in each spectral slice)

Proton ^{1}H *in vivo* spectroscopic images in a leg of a healthy human volunteer were acquired using two temporally interleaved sets of trajectories ($n_{TI} = 2$) with $f_1 = 300Hz$ and $f_2 = 284Hz$. The number of shots for each set was $N_{sh} = 128$ for a total of $N_{sh}^{RSI} = 2 \cdot 128 = 256$, which is somewhat greater than the minimum required for proper K-t space coverage as determined by the simulation program described at the beginning of Section 3.4, $N_{min} = 2 \cdot 107 = 214$. Spatial resolution was $N_x = 128$ and spectral bandwidth $\Delta\delta = n_{TI} \cdot (2 \cdot f_1) = 1200Hz$. Slice thickness $\Delta z = 2mm$, $fov = 18cm$, sampling rate $dt = 8us$ and repetition time was $T_R = 100ms$. No averages were used ($NEX = 1$), which resulted in a total scan time (including the $dda = 4$ equilibrium excitations at the beginning of the scan) of $T_{scan} = 26s$. Spectral resolution was $N_\delta = 74$, given by the useable readout time $T_{read} = 61.67ms$ for each excitation, with a separation of $1/T_{read} = 16.2Hz$ between spectral slices. In Figure 3-40, the spectral images of lipid (top) and water (bottom) resonances are displayed, with a separation between the central top image and central bottom image of 420Hz. The magnitude sum of the lipid (top) and water (bottom) images is shown in Figure 3-41.

Figure 3-40 Leg ^{1}H RSI: spectral images lipid (top) and water (bottom) $N_x = 128$, $fov = 18cm$, $T_{scan} = 26s$
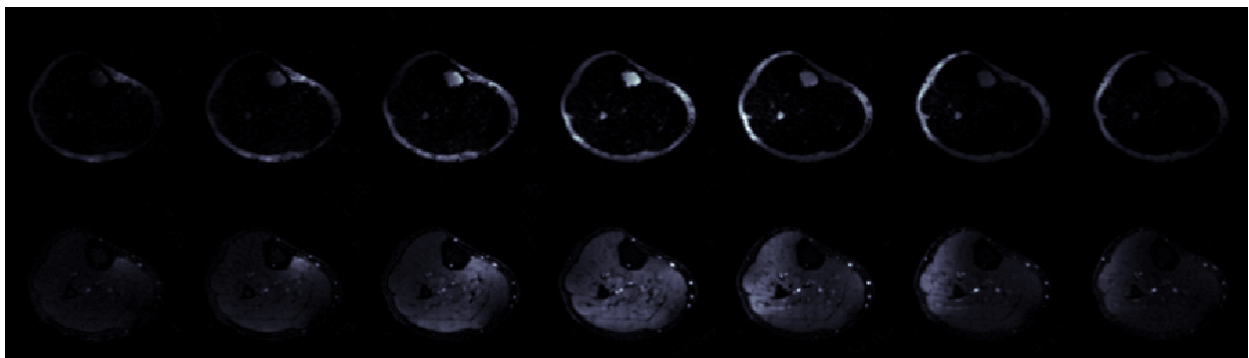
Figure 3-41 RSI: Sum of lipid images (top) and water (bottom) same intensity scale
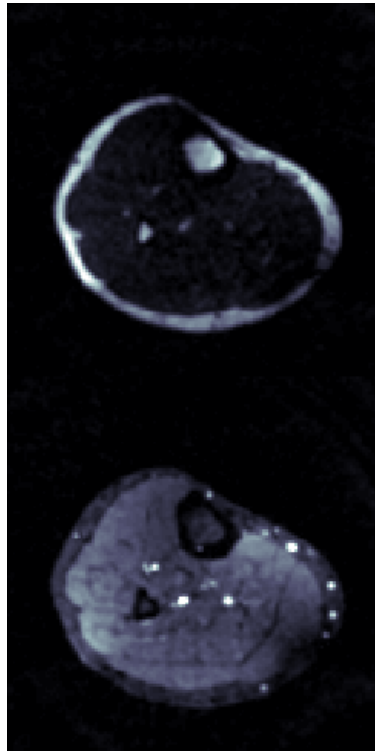
3.8.3 Self-Derived B_0 Map

Up to this point, we barely mentioned the B_0 main field inhomogeneities. The object inside the magnet bore modifies the field locally and this causes the resonant frequency $\omega_0 = \gamma \cdot B_0$ to vary as a function of position. This change is in addition to the one induced by the gradients played during the acquisition and, if not accounted for, during reconstruction will result in an assignment of information to spatial/spectral positions different than the real positions in space or spectrum. Especially for acquisitions with long readout times, as is the case with RSI, the B_0 inhomogeneities have an increased effect. Gradients on the scanner, called shimming gradients, are used preceding the actual data acquisition to minimize this problem; however, they do not eliminate it.

To determine the local resonant frequency map $f(x, y)$, two images are typically acquired at different echo times. The first image can be expressed as $M_1(x, y) = m_1(x, y) \cdot e^{i \cdot \varphi_1(x, y)}$ and the second image acquired at an echo time Δt later, can be expressed as $M_2(x, y) = m_2(x, y) \cdot e^{i \cdot \varphi_2(x, y)}$. The field map is given by:

$$f(x, y) = \frac{\varphi_2(x, y) - \varphi_1(x, y)}{2\pi \cdot \Delta t} \qquad (3.145)$$

This can also be computed as (M_1^* complex conjugate of M_1) [19]:

$$f(x, y) = \frac{angle(M_1^*(x, y) \cdot M_2(x, y))}{2\pi \cdot \Delta t} \qquad (3.146)$$

This expression is computationally more robust to angles of M_1, M_2 wrapping around 2π.

The K-t space data can be segmented [37, 38] in groups defined by the $K = 0$ crossings. In fact, we can have as many as N_δ groups (the number of temporal slices, section 3.3) that would generate as many full resolution images. However, because of the problematic spectral response function for very low N_δ, we choose to group the data in larger sets that include more temporal slices. The first group will include the first through $N_\delta - N_{maps}$ temporal slices; the second group will include the second temporal slice through $N_\delta - N_{maps} + 1$, and so on, with last set including temporal slices $N_{maps} + 1$ through N_δ. Each set generates a 2D image for a total of $N_{maps} + 1$ images acquired at echo times $\Delta t = m \cdot dT$, $m = 0, 1, ... N_{maps}$. Reconstructing data at the water resonance (if not already on-resonance, data is modulated to the water resonance frequency first), N_{maps} phase maps are calculated using $\Delta \varphi(x, y, \Delta t) = angle(M_1^*(x, y) \cdot M_2(x, y, \Delta t))$, where M_1^* is the complex conjugate of the first image acquired at $\Delta t = 0$ and M_2 is the image acquired at $\Delta t = m \cdot dT$, $m = 1, ... N_{maps}$. On a pixel-by-pixel basis, the phase maps are unwrapped

(Matlab function *unwrap*), and a linear regression fit is used to calculate the slope $2\pi f(x, y)$ of the function $\Delta\varphi(x, y, \Delta t) = 2\pi f(x, y) \cdot \Delta t$. For our acquisition ($N_\delta = 74$), we chose $N_{maps} = 7$. The result is the field map in Figure 3-42, left. The map in the skin area presents too much jerkiness, while smooth in all other regions. This is due to the water signal being weaker in the problematic area, which produces an inaccurate result. We repeat the B_0 map derivation procedure described above, but this time data is modulated to the lipid resonance. The result is the field map in Figure 3-42, center. Because there is only one field map, but the two maps look very different, we need to conciliate the two results. The explanation to the different appearance of the two maps is that they reflect the regions for which there was enough signal intensity to calculate the local frequency map. A combined B_0 map, that assigns for each position the value calculated in the water B_0 map if the water signal intensity is stronger than the lipid signal at that position, and the lipid B_0 map value if the lipid signal is stronger than the water, is calculated. The result is shown in Figure 3-42, right. Alternatively, this could be done by using a weighted (proportional to the signal intensity) contribution and the method is applicable when multiple resonances are present.

Figure 3-42 Leg B_0 Map: Color bar scales indicates amount of off-resonance in Hz.
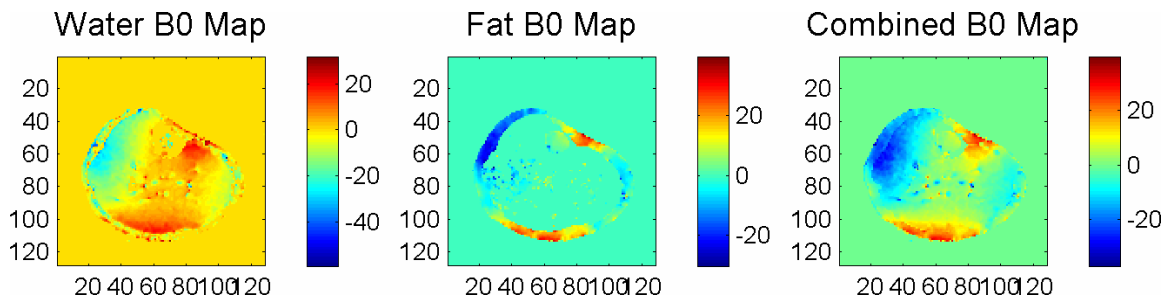
3.9   DISCUSSIONS AND CONCLUSIONS

In the spectrally selective imaging technique, using a multishot rosette trajectory acquisition developed by Noll [37], the random or irregular sampling in time of the k-space positions leads to off-resonance contributions canceling to noise distributed over the whole image. This background noise is in addition to other types of noise present in an MR image (thermal, systematic, physiological noise). In the 2D spectroscopic imaging technique we developed - RSI, we also employ the rosette trajectories but, by fully encoding the spatial-spectral information, this background noise can be eliminated and the greatest SNR sensitivity for these trajectories can be achieved. The off-resonance behavior of these trajectories (determined in our encoding approach by the regular sampling and phase accumulation at each K-space position) is investigated and we derive an analytical expression for the spectral response function. Using this expression, the position of the maxima and minima is derived and the width of the spectral passband in which there is very little degradation of the signal is shown to be equal to the inverse of the trajectory readout. In addition, it can be shown that the off-resonance behavior for a given frequency location improves when the trajectory readout increases. The spectral response behavior described by the function we derived is typical for all 2D spectroscopic imaging techniques using self-rewinding trajectories that periodically sample the center and edges of K-space thus, techniques like Out-and-In spiral spectroscopic imaging, PREP or spectroscopic TWIRL (Chapter 4.0) will have the same kind of off-resonance behavior as RSI.

Based on scanner hardware constraints (maximum gradient/slew rate/sampling rate), we derive the conditions for optimal rosette trajectories that provide the fastest K-t space coverage for a given spatial resolution and spectral bandwidth. There are three ways the trajectories can be designed. The most common way is to design the trajectory such a whole petal per each

trajectory will be contained in a temporal slice (within a spectral dwell time). For lower spectral bandwidth and/or lower spatial resolutions, it is possible to increase further the speed of the acquisition by allowing more than one petal per trajectory in each temporal slice (second way to design the trajectories). This case, usually results in an increase in sampling non-uniformity. However, by appropriately tweaking the trajectory parameters and the number of excitations used, this drawback (increased non-uniformity) can be partially eliminated while the gain in acquisition speed is preserved. The third way to design the trajectories, addresses the case where the spectral bandwidth targeted for the acquisition is larger than the one achievable with one set of trajectories and a number of temporally interleaved trajectory sets are used.

The problem of the number of excitations to be used in an RSI experiment is addressed in two ways. For fastest K-t space coverage, we wrote a simulation program that measures the distance between data samples and finds the minimum number of excitations such Nyquist sampling criterion is observed. More convenient would be to be able to use an analytical expression for the number of excitations to be used (second way). We derive such an expression. While the estimated number of excitations is an overestimate, we show that for this number the highest sampling uniformity for the RSI acquisition is achieved. In addition, an analytical expression correctly estimates the precompensation weights required when reconstructing the data.

We investigate the performance of the RSI acquisition technique. While RSI can achieve a speedup in data acquisition of one or two orders of magnitude compared to CSI, the SNR efficiency gain is approximately 15%. We first show that the quality factor of a fast CSI technique compared to classical CSI is proportional to the square root of the ratio between the readout (acquisition time) of the fast technique to the CSI readout. We derive the quality factors

for a few techniques that were calculated in a different way by Pohmann *et al.*. Based on this result, we demonstrate SPLASH cannot achieve a greater sensitivity than CSI at low spectral resolution, and offer an alternative explanation why methods like the Dixon method (spectral resolution $N_\delta = 2$), besides speedup in data acquisition, may be more suitable than CSI for lower spectral resolutions. Secondly, we measure the SNR advantage of an acquisition technique with K-space disk support versus one with square support. This advantage was noted by Bernstein *et al.* [4], and we found a CSI acquisition with K-space disk support can achieve a SNR sensitivity gain of up to 27% over a CSI with square support. Because of the rosette trajectories non-uniform sampling, RSI incurs a SNR penalty of approximately 10%. These predictions are verified with extensive simulations for a wide range of spectral bandwidths and spatial resolutions. We also conclude the sampling density postcompensation indispensable when precompensation weights are not properly calculated or known, and widely used in gridding reconstruction of non-Cartesian data, should be regarded as an additional filter (in addition to explicitly applied smoothing filters). This conclusion is supported by the increase in SNR (observed by us) and detail loss [31] for reconstructions using postcompensation versus the ones that only use precompensation.

The RSI technique is demonstrated experimentally on phantoms and *in vivo*. A full resolution field map is derived from the acquired data using linear regression and the spatial information found for each spectral resonance. The B_0 inhomogeneities are corrected for in the reconstructed data using an algorithm developed by Irarrazabal *et al.* [19].

4.0   SPECTROSCOPIC IMAGING WITH TWISTED RADIAL LINES

TRAJECTORIES (STWIRL)

4.1   TRAJECTORY DESIGN

We have shown in the previous chapter that the periodic sampling of the center and edges of K-space of the rosette trajectories previously used in an imaging fashion (spectrally selective imaging is modulation plus 2D reconstruction), allowed us to use them for spectroscopic imaging, simultaneously resolving the spatial and spectral information. We also showed that the non-uniform sampling associated with the rosette trajectories reduces by ~10% the SNR efficiency of the RSI technique. Further gains in SNR efficiency can be obtained if we adapt for spectroscopic imaging a fast data acquisition imaging technique that maintains uniform sampling.

A two dimensional imaging technique that achieves uniform sampling over most of K-space is TWIRL [22]. The Twisted Radial Lines (TWIRL) method has been introduced for magnetic resonance angiograms that are susceptible to flow-induced dephasing associated with irregular flow in vessels. While the flow-induced dephasing is minimized by using radial lines to cover K-space, radial lines provide a non-uniform, hence inefficient coverage. The K-space trajectories (Figure 4-1) start at the center of K-space ($K = 0$) as radial lines that begin twisting

at a position $K_0 = p \cdot K_{max}$ where $p < 1$ represents the fraction of imaging trajectories required compared to using radial lines ($\pi \cdot N_x$). Thus, the number of excitations:

$$N_{sh} = p \cdot \pi \cdot N_x \tag{4.1}$$

The speed along the trajectory is constant G and the constant sampling density requirement is equivalent mathematically to:
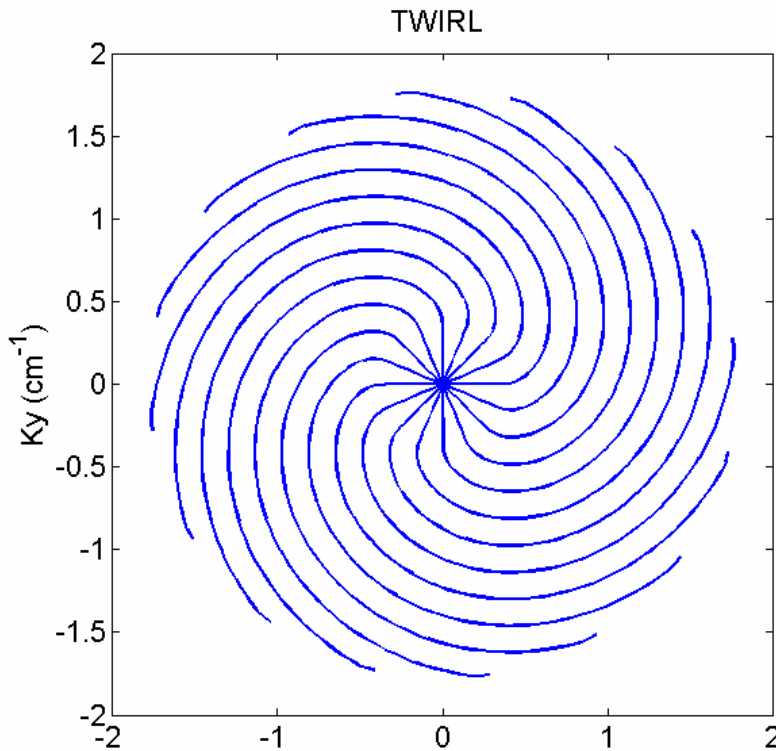
$$\dot{r}(t) \sim \frac{1}{r(t)} \tag{4.2}$$

The solution to equation(4.2) is:

$$K(t) = \sqrt{2 \cdot \gamma \cdot G \cdot K_0 \cdot t + K_0^2} \tag{4.3}$$

$$\vartheta(t) = \sqrt{\frac{2 \cdot \gamma \cdot G \cdot t}{K_0}} + \vartheta_0 - \arctan \sqrt{\frac{2 \cdot \gamma \cdot G \cdot t}{K_0}} \tag{4.4}$$

Figure 4-1 Twisted Radial Lines (TWIRL) imaging trajectories

116

Due to slew rate limitations ($S \leq S_{max}^{HW}$), when implemented, there are four different regions. In the first region from $K = 0$ to K_1, the gradient is ramped up (along a straight line). An optional second region, from K_1 to K_2, consists of a straight-line constant gradient. Over a third transitional region the trajectory starts twisting on a circle of radius K_s, between radial positions K_2 and K_3. Fourth region, from a radius K_3 to K_{max}, is the constant sampling density region where equations(4.3) and (4.4) are observed.

$$K_1 = \frac{\gamma \cdot G^2}{2S}; \ K_s = \frac{\gamma \cdot G^2}{S}; \ K_2 = \sqrt{K_0^2 - K_s^2}; \ K_3 = \sqrt{K_0^2 + K_s^2} \qquad (4.5)$$

The durations the trajectory spends in each region are:

$$t_1 = \frac{2 \cdot K_1}{\gamma \cdot G}; \ t_2 = \frac{K_2 - K_1}{\gamma \cdot G}; \ t_3 = \frac{K_s \cdot \arcsin(K_s / K_0)}{\gamma \cdot G}; \ t_4 = \frac{K_{max}^2 - K_3^2}{2 \cdot \gamma \cdot G \cdot K_0} \qquad (4.6)$$

The requirement to have a second region nonnegative duration ($t_2 \geq 0$) yields:

$$p \cdot K_{max} \geq \frac{\sqrt{5} \cdot \gamma \cdot G^2}{2 \cdot S} \qquad (4.7)$$

Satisfying equation (4.7) also insures the existence of the $\arcsin(K_s / K_0)$ in the t_3 expression.

It can be shown that in the fourth region the radial component of the trajectory gradient as a function of the distance K to the center of K-space is:

$$G_r(K) = G \cdot \frac{K_0}{K} \qquad (4.8)$$

This means that at the edge of K-space ($K = K_{max}$), the gradient has a nonzero radial component:

$$G_r(K = K_{max}) = G \cdot \frac{K_0}{K_{max}} = G \cdot p \qquad (4.9)$$

For spectroscopic imaging, to rewind smoothly the trajectory back to the center of K-space is equivalent to making sure the radial component of the gradient becomes null as is the case with the rosette trajectories (equation(3.11) at a time equal to a quarter of the radial oscillation period $t = \pi/2/\omega_1$). This could be accomplished in two ways. After reaching $K = K_{max}$, we could decrease the radial component to zero, allowing for uniform sampling over the entire fourth region of K-space, but the extra time spent outside of the useable K-space ($K > K_{max}$) would be wasted resulting in a lower useable readout time. This would translate into a lower SNR efficiency, similar to the effect observed for the PREP acquisition (equation(3.123)), as discussed in section 3.6.1. The second way to bring the gradient radial component to zero is to start decreasing it before it reaches $K = K_{max}$ and alter the uniform sampling over the region where this is done. We note that the loss in SNR efficiency associated with rewinding the gradients in the PREP acquisition calculated by Pohmann *et al.* is ~17%. The time to rewind the TWIRL gradients relative to their readout time will be shorter than for PREP where the full strength gradients ($G_r = G$) have to be rewound. However, we still expect the SNR efficiency loss to be greater when gradients are rewinded at $K > K_{max}$ (first way) compared to the loss induced by the sampling non-uniformity when rewinding starts before the edge of K-space ($K < K_{max}$). We choose the second modality and introduce a fifth region starting at $K_4 < K_{max}$ (the forth region extends now from a radius K_3 to K_4 instead of K_3 to K_{max}). If a slew rate S_d is used to bring the radial component of the gradient equal to $G_r(K_4) = G \cdot p \cdot K_{max} / K_4$ at K_4, to zero at $K = K_{max}$, K_4 can be determined by solving the equation:

$$K_{max} - K_4 = \frac{\gamma \cdot G^2 \cdot p^2 \cdot K_{max}^2}{2 \cdot K_4^2 \cdot S_d} \tag{4.10}$$

118

This is a cubic equation, which has analytical solutions. If a real positive solution, smaller than K_{max} and greater than K_3 is not found, the slew rate S_d chosen to bring the radial component of the gradient to zero may be too small. Because, during the process of rewinding the gradient in region five, we choose to maintain the speed along the trajectory as close as possible to the original speed G, through accordingly increasing the tangential component of the gradient, the slew rate S_d has to be smaller than the maximum hardware slew rate S_{max}^{HW}. We found values in between $S_d = .5 \cdot S_{max}^{HW}$ to $S_d = .7 \cdot S_{max}^{HW}$ to be good choices.

The gradient value G is chosen to obey the signal bandwidth/sampling requirement (equation(2.41)). To minimize the number of excitations required (equation(4.1)), the value for p is chosen to be the minimum value allowed by the inequality(4.7):

$$p = p_{min} = \frac{\sqrt{5} \cdot \not\gamma \cdot G^2}{2 \cdot S \cdot K_{max}} \tag{4.11}$$

Because the ramp up, region one, is necessary only to bring the gradient to the desired value, in addition to the trajectory designed as above, we design a trajectory that has a constant gradient G from $K = 0$ to $K = K_2$. Thus, for this second trajectory, region one is eliminated and the original region two extends now from $K = 0$ to $K = K_2$. The corresponding times spent in each region by the second trajectory are:

$$t_2' = \frac{K_2}{\not\gamma \cdot G}; \; t_3 = \frac{K_s \cdot \arcsin(K_s / K_0)}{\not\gamma \cdot G}; \; t_4' = \frac{K_4^2 - K_3^2}{2 \cdot \not\gamma \cdot G \cdot K_0}; \; t_5 = \frac{G \cdot p \cdot K_{max}}{S_d \cdot K_4} \tag{4.12}$$

The readout for this second trajectory is:

$$T_{read} = t_2' + t_3 + t_4' + t_5 \tag{4.13}$$

The two designed trajectories are used to obtain the spectroscopic imaging trajectory through concatenation. The second trajectory with no ramp-up is mirrored with respect to the

line that connects $K = 0$ and the point at the end of the first trajectory at $K = K_{max}$. The mirrored trajectory with no ramp up region is added at the end of the first trajectory. Thus, the $K = K_{max}$ point on the trajectory with no ramp up region marks the beginning of the second segment in the spectroscopic trajectory. Because this point is identical to the last point on the first segment (the trajectory with ramp up), it is discarded. At the end of the second segment, another trajectory with no ramp up region is added and the last point on the second segment, identical to the first point on the third segment, is removed and so on. One can choose to form figure-eight spectroscopic trajectories or keep rotating the trajectories in a counter-clockwise direction. We chose the later. To bring the gradients to zero, and end the trajectory at the center of K-space ($K = 0$), the last segment used in the spectroscopic trajectory is a trajectory with ramp up region, which now becomes a ramp down region. The trajectories have a pear-like appearance. In Figure 4-2, three different spectroscopic trajectories (shots), two segments (a petal) from each trajectory are shown.

Figure 4-2 Modified TWIRL (three different shots shown; two concatenated segments in each shot)
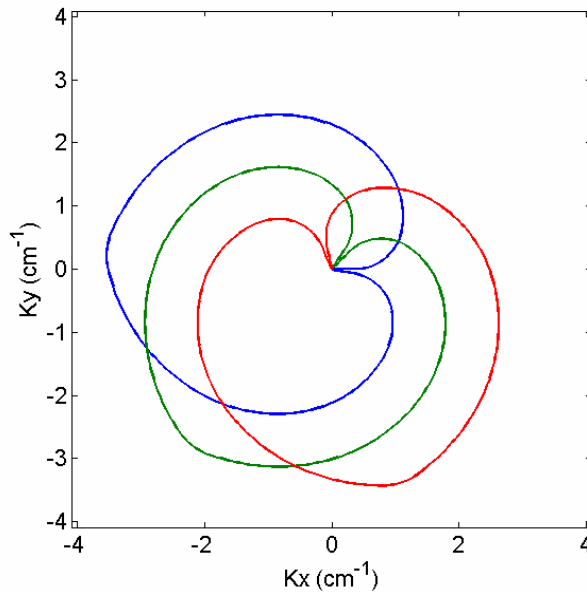
The time separation between two successive $K = 0$ crossings for a spectroscopic trajectory is $dT = 2 \cdot T_{read}$ where T_{read} is given by equations(4.12), (4.13). Therefore, the spectral bandwidth is:

$$\Delta \delta = \frac{1}{2 \cdot T_{read}} \qquad (4.14)$$

The K-t space sampling for three temporal slices is shown in Figure 4-3.

Figure 4-3 Spectroscopic TWIRL trajectories depicted in K-t space look similar to RSI trajectories
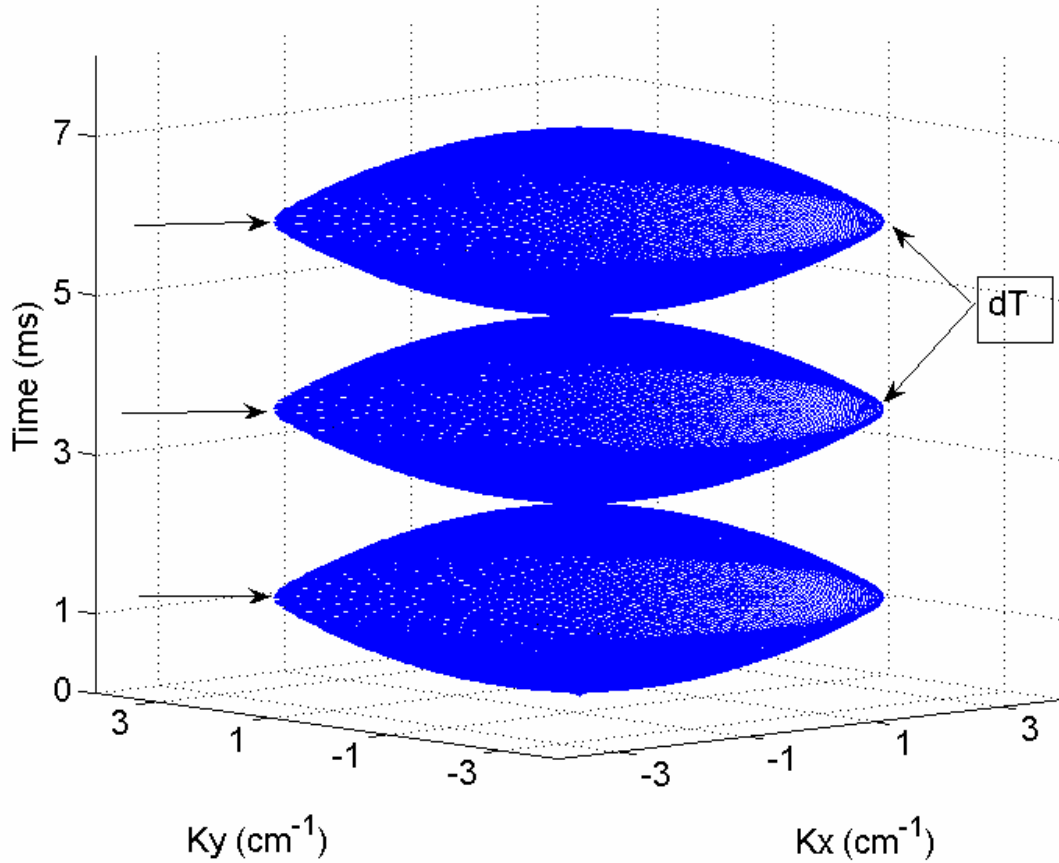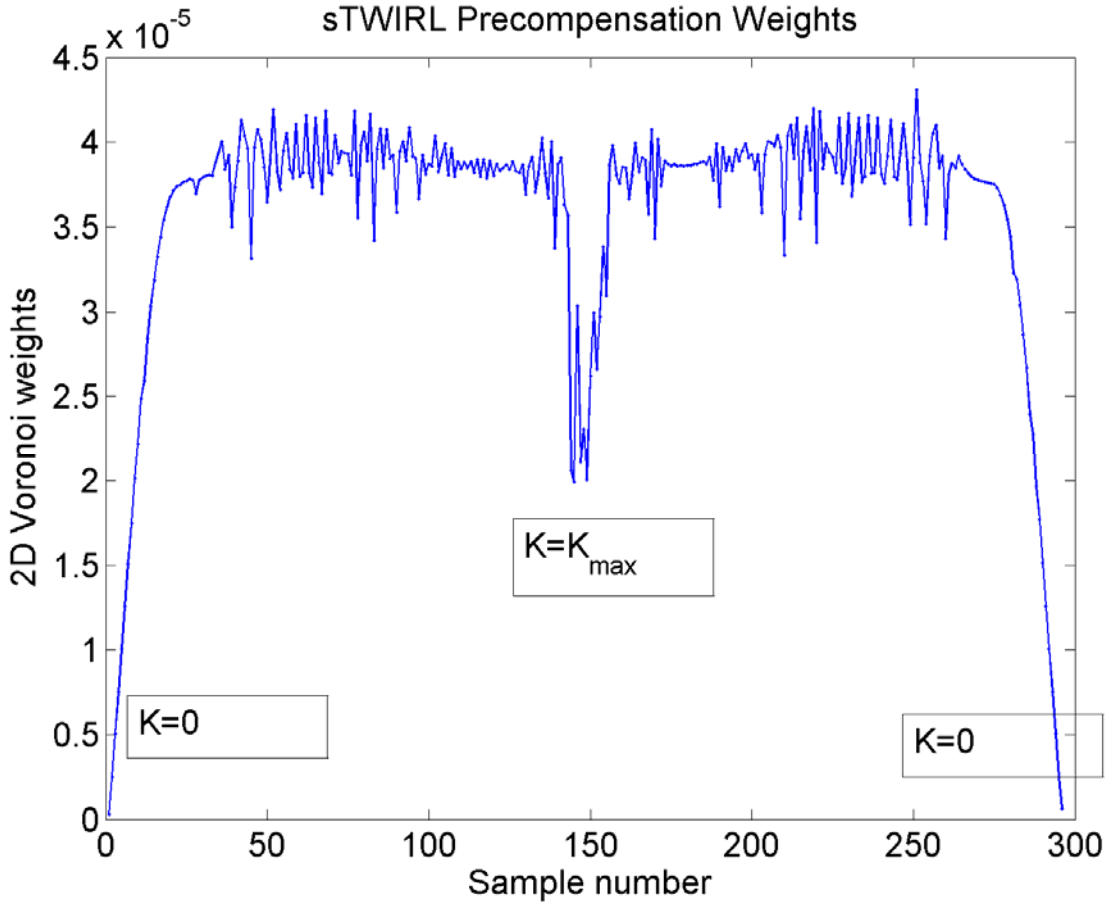
4.2 RESULTS

4.2.1 Simulation Results

Generating synthetic data (ellipses, disks (equations(3.140),(3.142)) at different spatial positions and resonances), we verified the reconstruction program properly resolves the spatial and spectral information.

To measure the SNR efficiency of the sTWIRL acquisition technique and to verify the theoretical predictions made in section 3.6, we used the same simulated object as for RSI (section3.7). The trajectories were designed for a spatial resolution $N_x = 128$, $fov = 18cm$. A spectral bandwidth $\Delta\delta = 850Hz$ is achieved by using two temporarily interleaved sets of trajectories $n_{TI} = 2$. The acquisition for the second set starts T_{read} later than the first set, corresponding to a time when the first set of trajectories set reaches $K = K_{max}$ (see the RSI example for two temporarily interleaved sets Figure 3-13). The maximum gradient is $G = 1.61G/cm$, $p = .23$ and the number of excitations for each trajectory set is $N_{sh} = 94$, thus the total number of excitations $N_{sh}^{sTWIRL}(n_{TI} = 2) = 2 \cdot N_{sh} = 188$. Spectral resolution is $N_\delta = 53$. The precompensation weights (Figure 4-4) are calculated as 2D Voronoi areas in each temporal slice (see section 3.5.1 step 1D on data reconstruction). The two interleaved trajectory sets result in slight variations in sampling density in region four supposed to have constant sampling density. The areas of non-uniform sampling near $K = 0$ and $K = K_{max}$ can easily be identified. We measured a sampling efficiency factor (see Appendix for definition) for these trajectories equal to $\eta_{sTWIRL} = .97$. As for the RSI measurements, no post compensation was used in

reconstructing the data. Running 10^3 simulations with different noise seeds, we measured a SNR efficiency relative to CSI of $\Omega_{sTWIRL} = 1.2157 \pm .0154$.

Figure 4-4 sTWIRL precompensation weights for two temporarily interleaved sets

4.2.2 Experimental Results

To demonstrate experimentally the sTWIRL technique, we used the same vegetable oil phantom used to demonstrate RSI (Section 3.8.1). We chose to use a longer readout time $T_{AQ} = 125ms$, for a spectral resolution of $1/T_{AQ} = 8Hz$. The sampling rate was $dt = 16us$, field of view $fov = 18cm$,

repetition time $T_R = 160ms$ and a gradient value along the constant sampling density region $G = G_{max} = .8 \cdot G/cm$. Trajectories were designed for a spatial resolution $N_x = 64$. With $S = S_{max}^{HW} = 15G/cm/ms$, p was chosen to be twice the minimum value allowed by (4.11), $p = 2 \cdot p_{min} = .2318$. Two temporally interleaved sets of trajectories $(n_{TI} = 2)$ with $N_{sh} = ceil(p \cdot N_x) = 47$ (for a total of 94 excitations), were used to achieve a spectral bandwidth $\Delta\delta = 856Hz$. In Figure 4-5, $N = 100$ out of $N_\delta = 107$ spectral (frequency) reconstructed slices are displayed, (800Hz out of 856Hz), after a B_0 field map (Figure 4-6) correction was applied.

Figure 4-5 sTWIRL acquisition; two temporally interleaved sets, $N_x = 64$, $\Delta\delta = 856Hz$
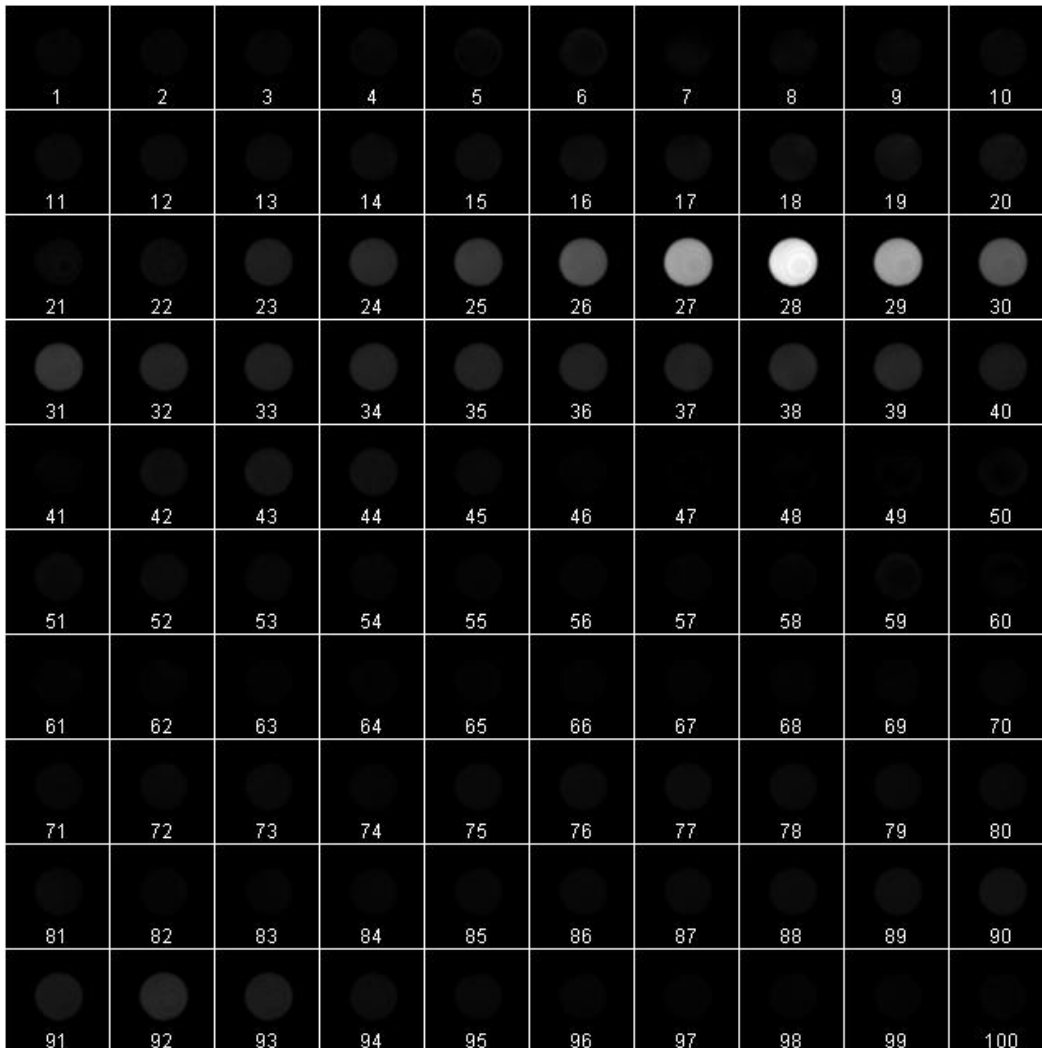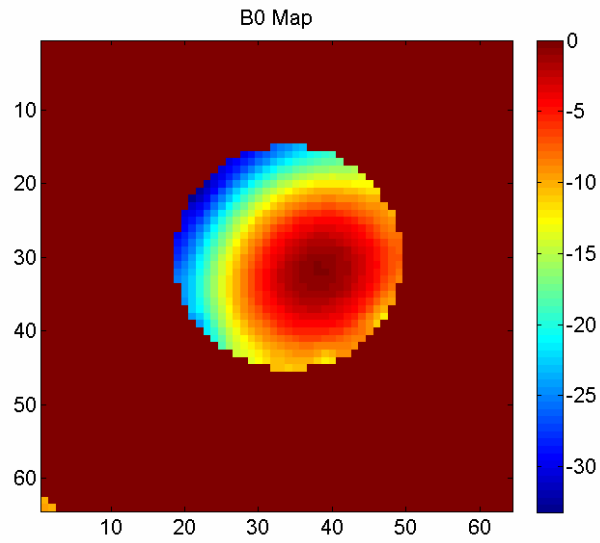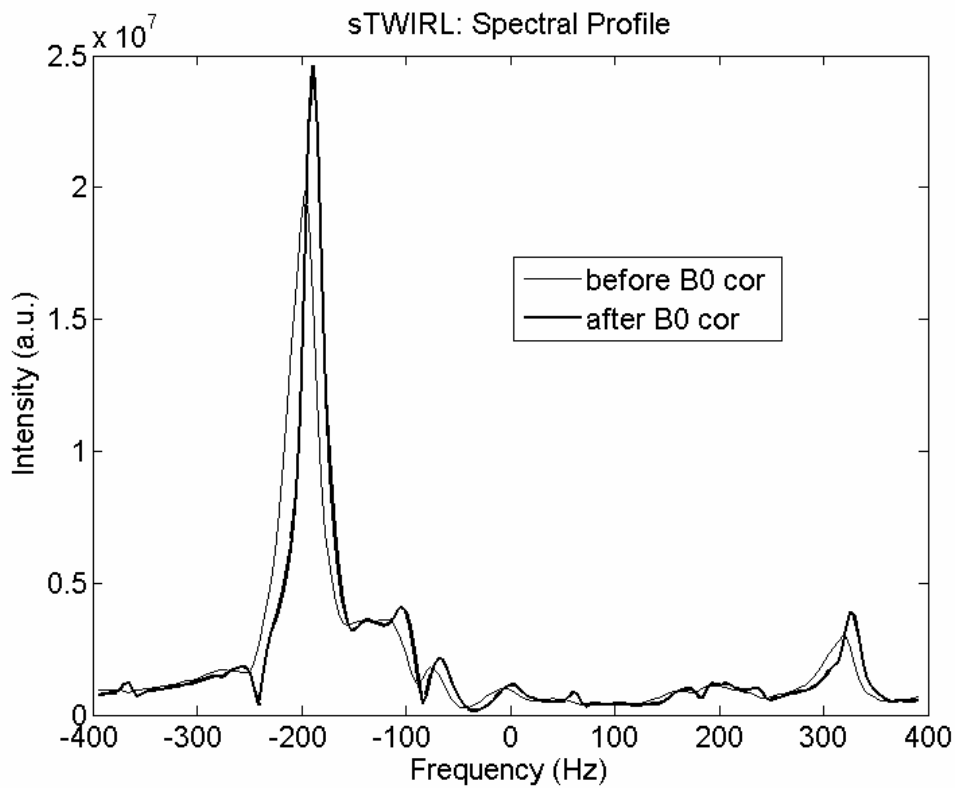
Figure 4-6 sTWIRL acquisition B_0 map

The spectral profile of the phantom, before (thin line) and after (bold line) B_0 correction, is shown in Figure 4-7.

Figure 4-7 sTWIRL oil bottle spectral profile before and after B_0 correction

125

5.0   CONCLUDING REMARKS

We introduce an MRSI imaging technique using the rosette trajectories - RSI, which can provide a speed up in data acquisition of up to two orders of magnitude compared to classical CSI. While the SNR performance of the technique is affected by the non-uniform sampling, because the trajectories do not spend time collecting data in the corners of K-space, RSI can offer an overall SNR advantage compared to classical CSI, providing great flexibility in choosing the total duration scan (based on the level of SNR desired). We investigate theoretically (and confirm through numerical simulations) how the regular patterns of phase accumulation in a rosette acquisition generate the spectral response function for which we derive an analytical expression. The same kind of spectral response is to be expected from all spectroscopic imaging techniques using trajectories that periodically sample the center and edges of K-space. The width of the spectral passband, the positions of the minima and maxima, and the fact the spectral response improves with the increase in trajectory duration, can be derived from this function. We derive an analytical expression for the number of excitations (shots) to be used in an RSI experiment that will provide the highest SNR performance when using these trajectories. An added benefit to using this number of shots is the analytical precompensation weights used in data reconstruction process are correctly estimated. This saves time in the reconstruction process and is important because non-uniformly sampled data weighted incorrectly can result in significant spectral leakage. Extensive simulations are employed to demonstrate the SNR efficiency of the RSI

acquisition over the classical CSI. The technique is demonstrated experimentally on phantoms and *in vivo*.

A second spectroscopic imaging technique (sTWIRL) that addresses the SNR performance penalty incurred by RSI due to non-uniform sampling is introduced and implemented experimentally. The uniform sampling density TWIRL trajectory introduced for imaging is modified and adapted for this method. A phantom is used for experimental demonstration.

An algorithm to generate a more accurate self-derived B0 map for objects with multiple resonances corresponding to different spatial distributions is offered.

From a more general perspective, our work complements and updates some of the results of an extensive theoretical study of the SNR performance of different fast CSI techniques. Namely, we analyze the performance of spectroscopic imaging techniques using non-Cartesian trajectories. While previously noted in an imaging context, that methods with K-space disk support could have an intrinsic SNR advantage over square supported methods, we demonstrate for 2D spectroscopic imaging this advantage can be of up to 27%. This result also suggests 3D spectroscopic imaging techniques with spherical support have a sensitivity of up to 91% greater than the ones with cubic K-space support. Therefore, for a spectroscopic imaging experiment, a disk or sphere supported CSI is more appropriate to be considered as reference when comparing the SNR efficiency of a technique. Moreover, disk/sphere supported CSI unlike their square/cubic counterparts provide for isotropic image resolution, a feature desirable in medical applications. As in imaging, the less uniform the sampling of K-t space, the higher the penalty in SNR for that technique. However, trajectories with uniform sampling density used in imaging like Twisted Radial Lines (TWIRL) for 2D or Twisted Projection Imaging (TPI) for 3D may be

adapted for spectroscopic imaging, closing the gap in SNR efficiency *vs.* rectilinear CSI. In addition, because of the time spent on phase encoding in CSI, there is potential SNR to be gained in RSI by starting the acquisition earlier, immediately following the excitation. As the total acquisition time of an experiment increases, the likelihood of patient moving increases and image artifacts could occur. By oversampling the low-frequency high-energy information at the center of K-space, self-rewinding trajectories are less sensitive to motion.

Finally, the longer reconstruction times involved with non-Cartesian trajectories could be soon reduced to insignificant. The most computationally demanding operations are calculating the sampling densities if an analytical formula does not estimate them correctly and the gridding process. For a given set of imaging parameters, the sampling densities can be pre-calculated and stored. The gridding algorithm is a prime candidate for parallelization. In computing, Moore's Law has been fulfilled over the past four decades, the computing power of a processor approximately doubled every 18-24 months, and the trend is expected to continue for at least another ten years through an increase in the number of CPU cores and execution units combined with smaller size transistors. An alternative also explored by scientists and programmers, is taking advantage of the extremely powerful parallel architecture of the graphical processing units (GPU) which, presently, could execute five to ten times more floating-point instructions per second than the CPUs. In the very near future, with appropriate optimizations, a small workstation should be able to achieve almost real time data reconstruction for 2D (and possible 3D) spectroscopic imaging techniques using non-Cartesian trajectories.

APPENDIX

THEORETICAL SAMPLING EFFICENCY OF ROSETTE TRAJECTORIES

Pipe *et al.* [48], showed that the relative SNR for a non-uniform sampling technique is reduced by a factor that is inverse proportional to the square root of the variance of that acquisition, variance that can be expressed as:

$$\text{var} = \frac{\sigma^2 \cdot M \sum_{n=1}^{N} \sum_{m=1}^{M} (w(m,n))^2}{T \cdot (\sum_{n=1}^{N} \sum_{m=1}^{M} w(m,n))^2} \qquad (A.1)$$

M is the number of samples per readout and N is the number of "read" periods (shots) of duration T. σ is the standard deviation of the white, uncorrelated noise. $w(m,n)$ is the weighting function, which is the same as the relative area/volume for the corresponding data point. The double summation in the denominator is equal to the entire area/volume of the K-space covered. Since this is fixed, the summation in the numerator is minimized when $w(m,n)$ is constant, for a variance $\text{var} = \sigma^2 / T$.

Therefore, for non-uniform sampling, the quantity that measures by how much the SNR is reduced with respect to a uniform acquisition ($\text{var} = \sigma^2 / T$), is:

$$\eta = \sqrt{\frac{(\sum_{n=1}^{N}\sum_{m=1}^{M}w(m,n))^2}{M\cdot(\sum_{n=1}^{N}\sum_{m=1}^{M}(w(m,n))^2)}} \tag{A.2}$$

In section 3.5.1, it was argued that 2D K-space weights could be used instead of 3D K-t volumes. Further, because of the periodicity of the rosette trajectory and because the shots are angularly uniform distributed, the expression in (A.2), can be calculated over one trajectory arm, from $K = 0$ to $K = K_{max}$, over a quarter period of the radial oscillation $T_1/4 = \pi/(2\omega_1)$. Thus, the sampling uniformity/efficiency factor η_{RSI} can be written as:

$$\eta_{RSI} = \sqrt{\frac{(\sum_{i=1}^{M}w_i)^2}{M\cdot\sum_{i=1}^{M}w_i^2}} \tag{A.3}$$

M is the number of samples between $K = 0$ and $K = K_{max}$, w_i is given by (3.93):

$$w_i = K_r^{(i)}\cdot\sqrt{K_{max}^2 - (K_r^{(i)})^2} = K_{max}^2\cdot\sin(2\cdot\omega_1\cdot t^{(i)}) \tag{A.4}$$

For sampling rates sufficiently high (small dt), the sums in (A.3) can be converted to integrals (with $M = (T_1/4)/dt$):

$$\eta_{RSI} = \frac{\int_0^{T_1/4} w(t)\cdot dt}{\sqrt{\frac{T_1}{4}\cdot\int_0^{T_1/4} w^2(t)\cdot dt}} = \frac{\int_0^{T_1/4} \sin(2\cdot\omega_1\cdot t)\cdot dt}{\sqrt{\frac{T_1}{4}\cdot\int_0^{T_1/4} \sin^2(2\cdot\omega_1\cdot t)\cdot dt}} = \frac{1}{\sqrt{\pi^2/8}} \approx .90 \tag{A.5}$$

BIBLIOGRAPHY

1. Adalsteinsson E, Irarrazabal P, Spielman DM, Macovski A. Three-dimensional spectroscopic imaging with time-varying gradients. Magn Reson Med 1995;33(4):461-466.

2. Barker PB, Hearshen DO, Boska MD. Single-voxel proton MRS of the human brain at 1.5T and 3.0T. Magn Reson Med 2001;45(5):765-769.

3. Beatty PJ, Nishimura DG, Pauly JM. Rapid gridding reconstruction with a minimal oversampling ratio. IEEE Trans Med Imaging 2005;24(6):799-808.

4. Bernstein MA, Fain SB, Riederer SJ. Effect of windowing and zero-filled reconstruction of MRI data on spatial resolution and acquisition strategy. J Magn Reson Imaging 2001;14(3):270-280.

5. Boada FE, Christensen JD, Gillen JS, Thulborn KR. Three-dimensional projection imaging with half the number of projections. Magn Reson Med 1997;37(3):470-477.

6. Boada FE, Gillen JS, Shen GX, Chang SY, Thulborn KR. Fast three dimensional sodium imaging. Magn Reson Med 1997;37(5):706-715.

7. Boada FE, Shen GX, Chang SY, Thulborn KR. Spectrally weighted twisted projection imaging: reducing T2 signal attenuation effects in fast three-dimensional sodium imaging. Magn Reson Med 1997;38(6):1022-1028.

8. Brown TR, Kincaid BM, Ugurbil K. NMR chemical shift imaging in three dimensions. Proc Natl Acad Sci U S A 1982;79(11):3523-3526.

9. Conolly S, Glover G, Nishimura D, Macovski A. A reduced power selective adiabatic spin-echo pulse sequence. Magn Reson Med 1991;18(1):28-38.

10. Conolly S, Nishimura D, Macovski A. Optimal Control Solutions to the Magnetic Resonance Selective Excitation Problem. IEEE Trans Med Imaging 1986;MI-5(2):106-115.

11. Conolly S, Pauly J, Nishimura D, Macovski A. Two-dimensional selective adiabatic pulses. Magn Reson Med 1992;24(2):302-313.

12. Dale BM, Lewin JS, Duerk JL. Optimal design of k-space trajectories using a multi-objective genetic algorithm. Magn Reson Med 2004;52(4):831-841.

13. de Graaf RA, Luo Y, Terpstra M, Garwood M. Spectral editing with adiabatic pulses. J Magn Reson B 1995;109(2):184-193.

14. Dixon WT. Simple proton spectroscopic imaging. Radiology 1984;153(1):189-194.

15. Doyle M, Mansfield P. Chemical-shift imaging: a hybrid approach. Magn Reson Med 1987;5(3):255-261.

16. Feng H, Gu H, Silbersweig D, Stern E, Yang Y. Single-shot MR imaging using trapezoidal-gradient-based Lissajous trajectories. IEEE Trans Med Imaging 2003;22(8):925-932.

17. Glover GH. Simple analytic spiral K-space algorithm. Magn Reson Med 1999;42(2):412-415.

18. Hiba B, Faure B, Lamalle L, Decorps M, Ziegler A. Out-and-in spiral spectroscopic imaging in rat brain at 7 T. Magn Reson Med 2003;50(6):1127-1133.

19. Irarrazabal P, Meyer CH, Nishimura DG, Macovski A. Inhomogeneity correction using an estimated linear field map. Magn Reson Med 1996;35(2):278-282.

20. Irarrazabal P, Nishimura DG. Fast three dimensional magnetic resonance imaging. Magn Reson Med 1995;33(5):656-662.

21. Jackson JI, Meyer CH, Nishimura DG, Macovski A. Selection of a convolution function for Fourier inversion using gridding [computerised tomography application]. Medical Imaging, IEEE Transactions on 1991;10(3):473-478.

22. Jackson JI, Nishimura DG, Macovski A. Twisting radial lines with application to robust magnetic resonance imaging of irregular flow. Magn Reson Med 1992;25(1):128-139.

23. Kim DH, Adalsteinsson E, Spielman DM. Spiral readout gradients for the reduction of motion artifacts in chemical shift imaging. Magn Reson Med 2004;51(3):458-463.

24. Kruger G, Kastrup A, Glover GH. Neuroimaging at 1.5 T and 3.0 T: comparison of oxygenation-sensitive magnetic resonance imaging. Magn Reson Med 2001;45(4):595-604.

25. Likes RS. Moving gradient zeugmatography. US patent 4 307 343 1981.

26. Lim KO, Pauly J, Webb P, Hurd R, Macovski A. Short TE phosphorus spectroscopy using a spin-echo pulse. Magn Reson Med 1994;32(1):98-103.

27. Man LC, Pauly JM, Macovski A. Improved automatic off-resonance correction without a field map in spiral imaging. Magn Reson Med 1997;37(6):906-913.

28. Man LC, Pauly JM, Macovski A. Multifrequency interpolation for fast off-resonance correction. Magn Reson Med 1997;37(5):785-792.

29. Mansfield P. Spatial mapping of the chemical shift in NMR. Magn Reson Med 1984;1(3):370-386.

30. Maudsley AA, Matson GB, Hugg JW, Weiner MW. Reduced phase encoding in spectroscopic imaging. Magn Reson Med 1994;31(6):645-651.

31. Meyer CH. Fast-scan imaging. 2004. p 1196-1199 Vol. 1192.

32. Meyer CH, Hu BS, Nishimura DG, Macovski A. Fast spiral coronary artery imaging. Magn Reson Med 1992;28(2):202-213.

33. Meyer CH, Pauly JM, Macovski A, Nishimura DG. Simultaneous spatial and spectral selective excitation. Magn Reson Med 1990;15(2):287-304.

34. Moriguchi H, Duerk JL. Iterative Next-Neighbor Regridding (INNG): improved reconstruction from nonuniformly sampled k-space data using rescaled matrices. Magn Reson Med 2004;51(2):343-352.

35. Moriguchi H, Wendt M, Duerk JL. Applying the uniform resampling (URS) algorithm to a lissajous trajectory: fast image reconstruction with optimal gridding. Magn Reson Med 2000;44(5):766-781.

36. Mosquera C, Irarrazabal P, Nishimura DG. Noise behavior in gridding reconstruction. 1995. p 2281-2284 vol.2284.

37. Noll DC. Multishot rosette trajectories for spectrally selective MR imaging. IEEE Trans Med Imaging 1997;16(4):372-377.

38. Noll DC, Meyer CH, Pauly JM, Nishimura DG, Macovski A. A homogeneity correction method for magnetic resonance imaging with time-varying gradients. Medical Imaging, IEEE Transactions on 1991;10(4):629-637.

39. Noll DC, Peltier SJ, Boada FE. Simultaneous multislice acquisition using rosette trajectories (SMART): a new imaging method for functional MRI. Magn Reson Med 1998;39(5):709-716.

40. Oesterle C, Markl M, Strecker R, Kraemer FM, Hennig J. Spiral reconstruction by regridding to a large rectilinear matrix: a practical solution for routine systems. J Magn Reson Imaging 1999;10(1):84-92.

41. O'Sullivan JD. A Fast Sinc Function Gridding Algorithm for Fourier Inversion in Computer Tomography. Medical Imaging, IEEE Transactions on 1985;MI-4(4):200-207.

42. Parker DL, Gullberg GT. Signal-to-noise efficiency in magnetic resonance imaging. Med Phys 1990;17(2):250-257.

43. Pauly J, Le Roux P, Nishimura D, Macovski A. Parameter Relations for the Shinnar-Le Roux Selective Excitation Pulse Design Algorithm. IEEE Trans Med Imaging 1991;10(1):53-65.

44. Pauly J, Nishimura D, Macovski A. A k-Space Analysis of Small-Tip-Angle Excitation. J Magn Reson 1989;81:43-56.

45. Pauly J, Spielman D, Macovski A. Echo-planar spin-echo and inversion pulses. Magn Reson Med 1993;29(6):776-782.

46. Pauly JM, Hu BS, Wang SJ, Nishimura DG, Macovski A. A three-dimensional spin-echo or inversion pulse. Magn Reson Med 1993;29(1):2-6.

47. Pickup S, Ding X. Pulses with fixed magnitude and variable phase response profiles. Magn Reson Med 1995;33(5):648-655.

48. Pipe JG, Duerk JL. Analytical resolution and noise characteristics of linearly reconstructed magnetic resonance data with arbitrary k-space sampling. Magn Reson Med 1995;34(2):170-178.

49. Pipe JG, Menon P. Sampling density compensation in MRI: rationale and an iterative numerical solution. Magn Reson Med 1999;41(1):179-186.

50. Pohmann R, von Kienlin M, Haase A. Theoretical evaluation and comparison of fast chemical shift imaging methods. J Magn Reson 1997;129(2):145-160.

51. Rasche V, Proksa R, Sinkus R, Bornert P, Eggers H. Resampling of data between arbitrary grids using convolution interpolation. IEEE Trans Med Imaging 1999;18(5):385-392.

52. Rourke DE, Bush SD. Inversion of the Bloch equations with T_{2} relaxation: An application of the dressing method. Physical Review E 1998;57(6):7216.

53. Sarty GE. Single TrAjectory Radial (STAR) imaging. Magn Reson Med 2004;51(3):445-451.

54. Sarty GE, Bennett R, Cox RW. Direct reconstruction of non-Cartesian k-space data using a nonuniform fast Fourier transform. Magn Reson Med 2001;45(5):908-915.

55. Scheffler K, Hennig J. Frequency resolved single-shot MR imaging using stochastic k-space trajectories. Magn Reson Med 1996;35(4):569-576.

56. Schomberg H, Timmer J. The gridding method for image reconstruction by Fourier transformation. Medical Imaging, IEEE Transactions on 1995;14(3):596-607.

57. Sedarat H, Nishimura DG. On the optimality of the gridding reconstruction algorithm. Medical Imaging, IEEE Transactions on 2000;19(4):306-317.

58.   Silva AC, Barbier EL, Lowe IJ, Koretsky AP. Radial echo-planar imaging. J Magn Reson 1998;135(1):242-247.

59.   Star-Lack JM. Optimal gradient waveform design for projection imaging and projection reconstruction echoplanar spectroscopic imaging. Magn Reson Med 1999;41(4):664-675.

60.   Stenger VA, Boada FE, Noll DC. Three-dimensional tailored RF pulses for the reduction of susceptibility artifacts in T_2^*-weighted functional MRI. Magnetic Resonance in Medicine 2000;44(4):525-531.

61.   Sutton BP, Noll DC, Fessler JA. Fast, iterative image reconstruction for MRI in the presence of field inhomogeneities. Medical Imaging, IEEE Transactions on 2003;22(2):178-188.

62.   Tsai CM, Nishimura DG. Reduced aliasing artifacts using variable-density k-space sampling trajectories. Magn Reson Med 2000;43(3):452-458.

63.   Tyszka JM, Mamelak AN. Volumetric multishot echo-planar spectroscopic imaging. Magn Reson Med 2001;46(2):219-227.